12-2013

Near-Infrared Surface-Enhanced Fluorescence Using Silver Nanoparticles in Solution

Michael D. Furtaw
University of Nebraska-Lincoln, mfurtaw@gmail.com

Furtaw, Michael D., "Near-Infrared Surface-Enhanced Fluorescence Using Silver Nanoparticles in Solution" (2013). *Mechanical (and Materials) Engineering -- Dissertations, Theses, and Student Research*. 63.
https://digitalcommons.unl.edu/mechengdiss/63

NEAR-INFRARED SURFACE-ENHANCED FLUORESCENCE USING SILVER NANOPARTICLES IN SOLUTION

by

Michael D. Furtaw

A DISSERTATION

Presented to the Faculty of

The Graduate College at the University of Nebraska

In Partial Fulfillment of Requirements

For the Degree of Doctor of Philosophy

Major: Mechanical Engineering and Applied Mechanics

Under the Supervision of Professor Gregory R. Bashford

Lincoln, Nebraska

December, 2013

NEAR-INFRARED SURFACE-ENHANCED FLUORESCENCE USING SILVER NANOPARTICLES IN SOLUTION

Michael D. Furtaw, Ph.D.

University of Nebraska, 2013

Advisor: Gregory R. Bashford

Fluorescence spectroscopy is a widely used detection technology in many research and clinical assays. Further improvement to assay sensitivity may enable earlier diagnosis of disease, novel biomarker discovery, and ultimately, improved outcomes of clinical care along with reduction in costs. Near-infrared, surface-enhanced fluorescence (NIR-SEF) is a promising approach to improve assay sensitivity via simultaneous increase in signal with a reduction in background. This dissertation describes research conducted with the overall goal to determine the extent to which fluorescence in solution may be enhanced by altering specific variables involved in the formation of plasmon-active nanostructures of dye-labeled protein and silver nanoparticles in solution, with the intent of providing a simple solution that may be readily adopted by current fluorescence users in the life science research community. First, it is shown that inner-filtering, re-absorption of the emitted photons, can red-shift the optimal fluorophore spectrum away from the resonant frequency of the plasmon-active nanostructure. It is also shown that, under certain conditions, the quality factor may be a better indicator of SEF than the commonly accepted overlap of the fluorophore spectrum with the plasmon resonance of the nanostructure. Next, it is determined that streptavidin is the best choice for carrier protein, among the most commonly used dye-labeled detection antibodies, to enable the largest fluorescence enhancement when labeled with IRDye 800CW and used in combination with silver nanoparticles in solution. It is shown that the relatively small and symmetric geometry of streptavidin enables substantial electromagnetic-field confinement when bound to silver nanoparticles, leading to strong and reproducible enhancement. The role of silver nanoparticle aggregation is demonstrated in a droplet-based microfluidic chip and further optimized in a standard microtiter-plate format. A NIR-SEF technology based on aggregation with optimized salt concentration demonstrates a fluorescence signal enhancement up to 2530-fold while improving the limit-of-detection over 1000-fold. Finally, the NIR-SEF technology is applied to demonstrate 42-fold improvement in sensitivity of the clinically-relevant biomarker, alpha-fetoprotein, along with a 16-fold improvement in limit-of-detection.

COPYRIGHT

ACKNOWLEDGMENTS

There are many people who enabled the completion of this work and I will be forever in debt to all of them. I would like to thank my advisor, Dr. Greg Bashford, for giving me guidance and encouragement along the way. He took me on as a PhD student in unusual and unfortunate circumstances that ended up being a blessing to me. I would like to thank my committee members, Dr. Angela Pannier, Dr. Shadi Othman, Dr. David Hage, Dr. John Barton, and Dr. Jon Anderson, for their time, commitment, and invaluable advice. I would like to further thank Dr. Jon Anderson for being my mentor on this research topic.

I owe special thanks to LI-COR Inc. for encouraging me to continue my education and being flexible enough to enable the process, while keeping me as a full-time employee. Lyle Middendorf, in particular, has been so supportive of the entire process that I could never thank him enough.

Lastly, I must acknowledge my wonderful family. My parents, Paula Wicks and Tom Furtaw, have always offered unconditional love and encouragement to pursue my dreams. My sister, Katie Keuneke, has always been a step ahead of me in life and shows me the way to the next chapter. My wife, Nicole Furtaw, has offered endless love and support along the way. The greatest comfort comes with knowing that regardless of any academic or professional attempt, success or failure, my family will always be…

TABLE OF CONTENTS

List of Symbols and Abbreviations

Symbols

α	polarizability (nm^3)
γ	decay rate (eV)
ε	relative permittivity (relative to ε_0)
ε_0	permittivity of free space ($8.854 \text{x} 10^{-12}$ F·m^{-1})
λ	wavelength (nm)
ω	angular frequency (eV)
ω_p	plasma frequency (rad·s^{-1})
a	radius (nm)
A	absorbance (AU)
C	cross-section (nm^2)
e	elementary charge ($1.602 \text{x} 10^{-19}$ C)
f_n	natural frequency (rad·s^{-1})
I	intensity (W·nm^{-2})
k	wave number (rad·nm^{-1})

k_s	spring constant ($N \cdot m^{-1}$)
L	depth (nm)
m	mass (kg)
m_e	electron mass (9.11×10^{-31} kg)
m^*	effective mass (relative to m_e)
N	number density ($mol \cdot nm^{-3}$)
n_e	number density of electrons ($mol \cdot cm^{-3}$)
q	quantum yield
Q	quality factor

Abbreviation

AFP	alpha fetoprotein
AgNP	silver nanoparticle(s)
AuNP	gold nanoparticle(s)
Av	avidin
b-BSA	biotinylated bovine serum albumin
BEM	boundary element method

BSA	bovine serum albumin
CCD	charge-coupled device
dH_2O	deionized water
DLS	dynamic light scattering
ELISA	enzyme-linked immunosorbent assay
Fab	fragment, antibody-binding
F(ab')$_2$	fragment, double antibody-binding
FLISA	fluorophore-linked immunosorbent assay
FWHM	full-width half-maximum
ICG	indocyanine green
IgG	immunoglobulin G
LOD	limit of detection
LOQ	limit of quantitation
LSP	localized surface plasmon(s)
MEF	metal enhanced fluorescence
mNP	metal nanoparticle(s)
NaCl	sodium chloride

NAv	neutravidin
NIR	near infrared
PBS	phosphate buffered saline
PBST	phosphate buffered saline with Tween
PMMA	poly(methyl methacrylate)
PSP	propagating surface plasmon(s)
RDE	radiative decay engineering
SAv	streptavidin
SDS-PAGE	sodium dodecyl sulfate polyacrylamide gel electrophoresis
SEF	surface enhanced fluorescence
SEFLISA	surface enhanced fluorophore-linked immunosorbent assay
SEM	scanning electron microscopy
SERS	surface enhanced Raman scattering
SIF	silver island films
SP	surface plasmon(s)
TEM	transmission electron microscopy
UV	ultra-violet

List of Figures and Tables

CHAPTER 1. INTRODUCTION

1.1. FLUORESCENCE SPECTROSCOPY

Fluorescence spectroscopy, the optical detection of light emitted by a fluorophore upon relaxation from light-induced excitation, has been widely used for imaging and detection in the biological and chemical sciences for many years[1]. Due to its unique combination of sensitivity and quantitation, fluorescence spectroscopy has replaced other imaging and detection modalities in various applications, including many life science and chemical research assays. As an example, the western blot traditionally made use of radioactivity[2] or, more recently, chemiluminescence[3] via radiolabeled and enzyme-labeled antibodies, respectively. Radioactivity is a very sensitive detection technique involving the measurement of ionizing radiation emitted due to isotopic decay; however, it requires special safety precautions and limits the ability to multiplex (detect multiple antigens or multiple epitopes of a single antigen). Chemiluminescence involves the use of enzyme-linked antibodies that create a luminescent signal when combined with an appropriate substrate. Enzyme-based detection strategies, such as chemiluminescence, are often sensitive but limiting in terms of quantitation, due to a relatively small linear range, and the inability to multiplex. Fluorescence has since been adapted to the western blot technique in order to simultaneously detect multiple antigens of interest[4] and to enable more accurate protein quantitation[5]. Another example is the enzyme-linked immunosorbent assay (ELISA), one of the most widely used among all assay techniques in clinical and research settings[6]. While ELISA is sufficient for many clinical and research diagnoses, the method may be inadequate for some biomarker implementations and development. ELISA typically involves the enzyme-based production of a colorimetric product for detection, which can limit its linear range and inherently limits the ability to simultaneously measure multiple antigens of interest. The fluorophore-linked immunosorbent assay (FLISA) is a closely related technique, which employs fluorophore-labeled antibodies for a fluorescence-based detection strategy, that offers some advantages including an extended linear range, a reduced number of assay steps, and multiplexed detection[7]. In summary, fluorescence spectroscopy has been shown to compare advantageously to other detection modalities when considering the important assay parameters of sensitivity, dynamic range, cost, quantitation, and ability to multiplex.

Fluorescence spectroscopy is also used in many applications beyond the detection technique in bioassays. Due to the ability to detect many fluorophores of differing wavelengths simultaneously, fluorescence is often used for detailed imaging applications such as cells[8], tissue sections[9], and small animals[10]. The future appears promising for fluorescence spectroscopy as new applications continue to evolve. Recently, fluorescence has translated into clinical research enabling innovation in, e.g., image-guided surgery[11] and detection of biomarkers associated with cancer[12-14] and other diseases[15-17].

1.2. NEED FOR ENHANCED SENSITIVITY

Despite being a well-established, broadly-used technique, there remains a demand for improved sensitivity for many applications that rely on the use of fluorescence. Further improvement to assay sensitivity, in general, remains desirable for early detection of cancer and other diseases, as well as novel biomarker discovery. Clinical assays that detect cancer early can prevent progression[18] which may lead to improved prognosis and reduced costs of care[19]. Highly-sensitive clinical assays may also lead to routine cancer screening as opposed to investigation of suspected tumors[20], which is often too late for a favorable prognosis. Improved limit of detection (LOD) may also enable researchers to identify novel biomarkers that lack the *in vivo* quantity required for detection with currently available diagnostic technology[21-23]. Along with reducing assay LOD, it is also desirable to be able to measure small changes in biomarker concentration. For example, prostate specific antigen (PSA) is an important biomarker to measure over time after radical prostatectomy. Removal of the main source of PSA[24], however, makes the serum levels difficult to detect due to extremely low abundance. Enhanced sensitivity may also enable novel biomarkers that can be taken from non-local samples, such as blood, breath, urine, or sweat, where the concentration is significantly lower than near the diseased organ. An example is Alzheimer's disease which can often be confirmed by biomarkers obtained via brain biopsy, however, measurement in blood or cerebrospinal fluid may enable detection without major surgery or autopsy[25].

The potential of improved prognoses and reduction in costs of care has led to a surge in research aimed at increasing the sensitivity, and thus the LOD, of biomarker assays in an attempt to diagnose disease as early as possible. LOD can be improved through increased signal intensity and/or reduced background noise. In fluorescence-based bioassays, the antigen of interest (biomarker) is indirectly detected using a fluorophore-labeled antibody that binds to it. Ideally, every antigen is bound by one or more labeled antibodies and the antibodies do not bind to other molecules or surfaces and thus a signal is generated that is directly proportional to the amount of antigen present in the sample. Therefore, the main contributors to the signal in fluorescence-based assays are the efficiencies of the fluorescence and antibody binding processes. Likewise, the main contributors to the background noise are the autofluorescence or scatter from the assay materials and non-specific binding of the antibodies. This work focuses on improvements to the fluorescence process, including signal and background. One approach to reduction in background noise is to use near-infrared (NIR) fluorescence. NIR fluorescence typically has lower background than visible fluorescence due to reduced scatter[26] and lower autofluorescence[27] of common assay substrates. Unfortunately, NIR probes often suffer from lower signal intensity, relative to visible probes, due to low intrinsic quantum yield[28]. An approach to overcome low intrinsic quantum yield, and thus, improve fluorescence signal is by locating the fluorophore near a plasmon-active nanostructure (typically gold or silver), which leads to modified excitation and decay rates, a process known as surface-enhanced fluorescence (SEF). SEF is a technology that can significantly improve quantum yield, increase the excitation rate of fluorophores, as well as improve photostability. The combination of NIR probes and SEF has the potential to synergistically improve the LOD of fluorescence-based assays by simultaneously increasing the numerator (signal), while decreasing the denominator (background noise) in the signal-to-noise ratio.

1.3. LONG-TERM GOAL OF RESEARCH

Ultimately, it is desirable to have a full understanding and complete control of the SEF process in order to maximize the detectability of individual fluorophores. This knowledge would enable the design of optimized plasmon-active substrates that could then be fabricated with high efficiency and subsequently applied to improve the use of fluorescence spectroscopy. An example outcome of achieving this goal could be orders of magnitude reduction in LOD leading to novel diagnostic biomarkers. SEF may also benefit assays where the necessary LOD is already achievable by reducing the power and sensitivity requirements of the optical components. A reduction in required excitation intensity and detector sensitivity may enable low-cost, early diagnosis of disease in third-world countries using fluorescence detection with a cell phone in ambient light. Fluorophore design and synthesis may also benefit from SEF if the intrinsic quantum yield is no longer a major technical hurdle. These opportunities may be achievable after several research goals are met, including: identification of optimal plasmon-active nanostructure geometries for various fluorophores, enabling the accurate prediction of the enhancement potential of various nanostructure geometries combined with various fluorophores via mathematical models, development of efficient fabrication processes to create the nanostructures, assembly of the various nanostructures with their respective emitters in a reproducible and efficient process, and assay design to implement the technology in ways beneficial to society.

1.4. CONTRIBUTION OF RESEARCH IN THIS DISSERTATION

This dissertation describes research conducted with the overall goal to determine the extent to which NIR fluorescence signal in solution may be enhanced using citrate-stabilized silver nanoparticles (AgNP) by altering specific variables involved in the process, with the intent of providing a simple solution that may be readily adopted by current fluorescence users in the life science research community. Specifically, the following contributions to the research community are disclosed:

i. The idea that an emitter must spectrally overlap with the resonance of the plasmon-active substrate is challenged and demonstrated to be true only in particular situations. Further, it is shown that significant enhancement can be achieved with plasmon-active substrates that have minimal ensemble, far-field interaction with the excitation or emission light (Chapter 3).

ii. It is shown that various proteins can enable SEF using non-specific interactions with AgNP in solution. It is also determined that streptavidin (SAv) may be the most effective, commonly used carrier protein for enhanced detection using SEF-based immunoassays (Chapter 4).

iii. A microfluidic device is used to investigate the relationship between mixing of AgNP with dye-labeled SAv and the ability to generate NIR-SEF. This is the first known combination of SEF and microfluidics in the literature (Chapter 5).

iv. Aggregation of AgNP and dye-labeled SAv to enhance fluorescence signal is further investigated in the more common assay environment of a microtiter plate. Greater than 1000-fold improvement in LOD is demonstrated for NIR-dye-labeled SAv using citrate-stabilized AgNP in solution combined with an optimized salt concentration (Chapter 6).

v. A NIR-SEFLISA assay is described with a demonstration of 42-fold improvement in sensitivity, along with a 16-fold reduction in LOD for the clinically-relevant biomarker, alpha fetoprotein (AFP) (Chapter 7).

CHAPTER 2. BACKGROUND INFORMATION AND LITERATURE REVIEW

2.1. FLUORESCENCE SPECTROSCOPY

Fluorescence spectroscopy is the optical detection of molecules that absorb a particular spectrum of electromagnetic radiation (light) and re-emit electromagnetic radiation at another spectrum. Figure 2.1 shows a simplified Jablonski diagram[29] that demonstrates the fluorescence mechanism. The absorption of a single photon with an appropriate frequency, and thus energy, causes an electron to move from the electronic ground state to a high-energy state. Over a very short period of time, (e.g. 10^{-12} s)[1], the electron loses some energy to the environment (in the form of heat) which moves the electron to the lowest singlet excited state. After some time in this state, (e.g. 10^{-8} s)[1], the electron is then able to move back to the electronic ground state by emitting the remaining energy as another single photon at a lower frequency (longer wavelength).

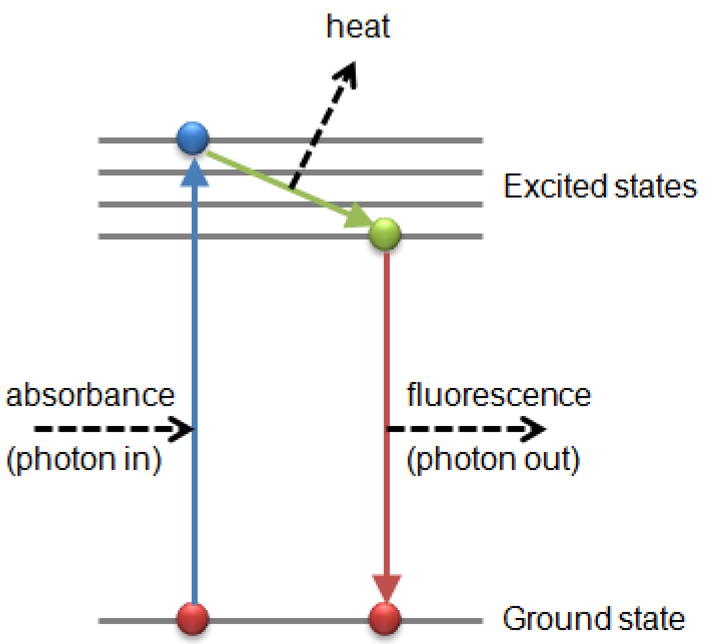

Figure 2.1. Jablonski diagram of the fluorescence mechanism. A photon is absorbed causing the molecule to move to an excited electronic state (blue line). The molecule loses some energy to heat as it moves to the lowest excited state (green). A photon is spontaneously emitted allowing the molecule to return to the ground state (red line).

The optical detection of this process, known as fluorescence spectroscopy, is conducted by exciting the fluorophore with a light source at an appropriate wavelength (one readily absorbed by the fluorophore) and collecting the emission light at a longer wavelength. The excitation source can be a laser, light-emitting diode, or a broadband filament bulb with an appropriate filter in place. The emission is also filtered to prevent the detection of scattered excitation light. The difference between the wavelength of maximum absorption and the wavelength of maximum emission is known as the Stokes' shift. The longer the Stokes' shift, the easier it is to separate the emission energy from the excitation energy. It is common for an organic fluorophore to have a Stokes' shift of approximately 10 - 20 nm. As an example, Figure 2.2 shows the absorbance and emission spectra for IRDye 800CW which is used frequently in this dissertation.

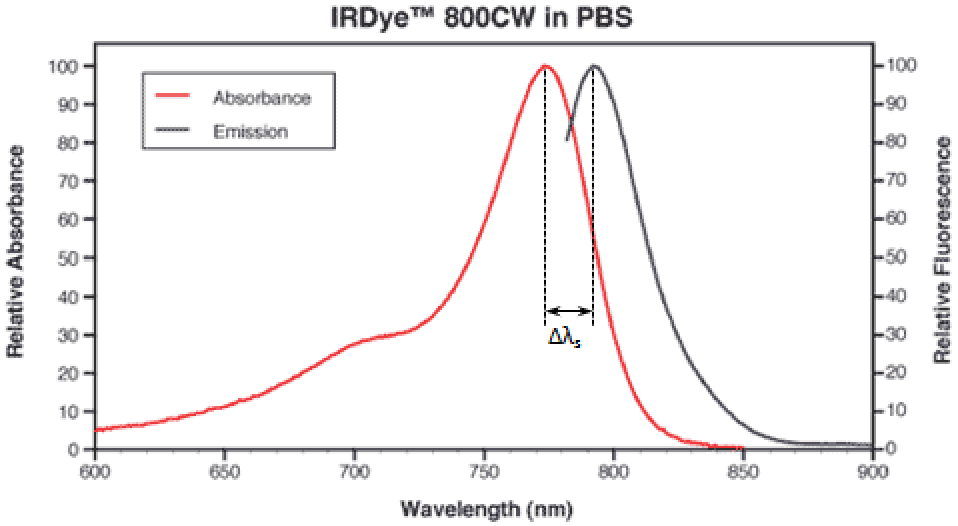

Figure 2.2. Aborbance and emission spectra of IRDye 800CW in PBS. The Stokes shift ($\Delta\lambda_S$) is the difference between the wavelength of maximum absorbance and the wavelength of maximum emission. Copyright LI-COR, Inc. Adapted with permission.

2.2. NEAR-INFRARED FLUORESCENCE

NIR fluorescence involves fluorophores that absorb and emit light in the wavelength range of 700 - 900 nm. NIR fluorescence typically has lower background than visible fluorescence due to reduced scatter[26] and lower autofluorescence[30] of common assay substrates such as nitrocellulose, polyvinylidene difluoride (PVDF), poly(methyl methacrylate) (PMMA), and polydimethylsiloxane (PDMS). NIR fluorescence is also useful for *in-vivo* imaging due to deeper penetration in tissue and reduced autofluorescence, compared to visible light. The deeper penetration is mostly enabled due to the relatively low absorption and scatter of NIR light by hemoglobin (oxygenated and deoxygenated) and water. Figure 2.3 shows the extinction coefficient of hemoglobin, oxygenated hemoglobin, and water in the wavelength range of 400 to 1000 nm. The extinction coefficient of a material is the amount of light attenuation per mole of the material, per unit length of depth. In addition to the increased depth of penetration, the lower absorption and scatter of biological materials in the NIR also reduces the autofluorescence and total background signal, which ultimately leads to improved signal-to-noise. The advantages of NIR fluorescence for *in vivo* imaging of animals and humans has led to applications, including imaging of normal and diseased vasculature, tissue perfusion, protease activity, hydroxyapatite, and cancer[31].

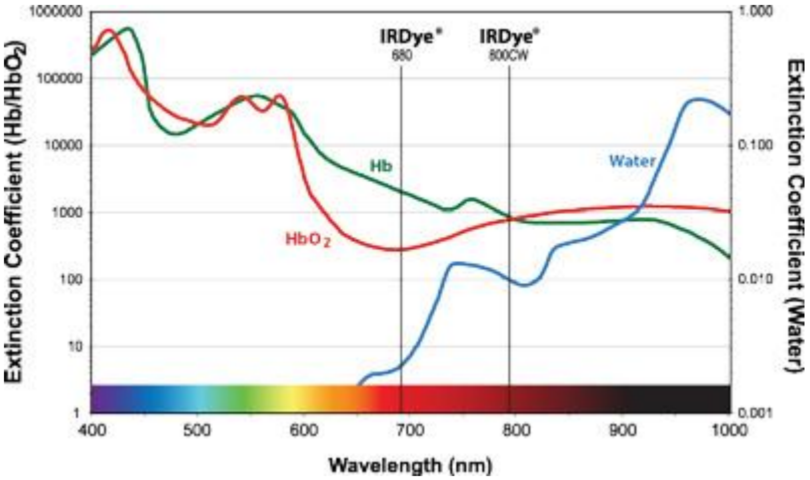

Figure 2.3. Extinction coefficient of hemoglobin, oxygenated hemoglobin, and water across the visible to NIR spectrum. Copyright LI-COR, Inc. Reprinted with permission.

2.3. SURFACE PLASMONS

Plasmonics is another important research topic involving the interaction of light and electrons. When a metal nanoparticle (mNP) is subjected to an electromagnetic field at certain frequencies, its conduction band electrons can be forced to oscillate within the particle volume and slightly into the surrounding medium. The electrons can be thought of as an incompressible fluid, often referred to as an electron cloud. The collective oscillations of these electron clouds are known as localized surface plasmons (LSP). They are termed 'localized' because the net displacement, relative to the mNP, is zero. There are propagating surface plasmons (PSP) that can occur on the surface of larger metal structures in which the net displacement is not zero; however, the research included in this dissertation relies specifically on LSP.

LSP can be modeled as a spring-mass system where the mass is analogous to the electron cloud and the spring is analogous to the electric charge caused by the displacement of the electron cloud (see Figure 2.4). The natural frequency (f_n) of a spring-mass system is given by

$$f_n = \sqrt{\frac{k_s}{m}} \qquad (1)$$

where k_s is the spring constant and m is the mass. Similarly, the plasma frequency $\left(\omega_p\right)$ of LSP is given by

$$\omega_p = \sqrt{\frac{n_e e^2}{m^* \varepsilon_0}} \qquad (2)$$

where n_e is the number of electrons, e is the charge of one electron, m^* is the mass of one electron, and ε_0 is the permittivity of the surrounding medium. Equations 1 and 2 show the similarity of LSP to that of a simple, spring-mass system; however, like nearly all natural systems (as opposed to ideal systems) there are non-linear damping processes and other higher-order effects that must be considered. The collective effects of all processes involved determine the response of the electron cloud to the electromagnetic field, which is represented as the complex permittivity (ε_m) of the material, or,

$$\varepsilon_m = \varepsilon_1 + i\varepsilon_2 \qquad (3)$$

The complex permittivity enables theoretical prediction of light-interaction at the nanoscale[32] and can be obtained via theoretical models[33, 34] or empirical data[35].

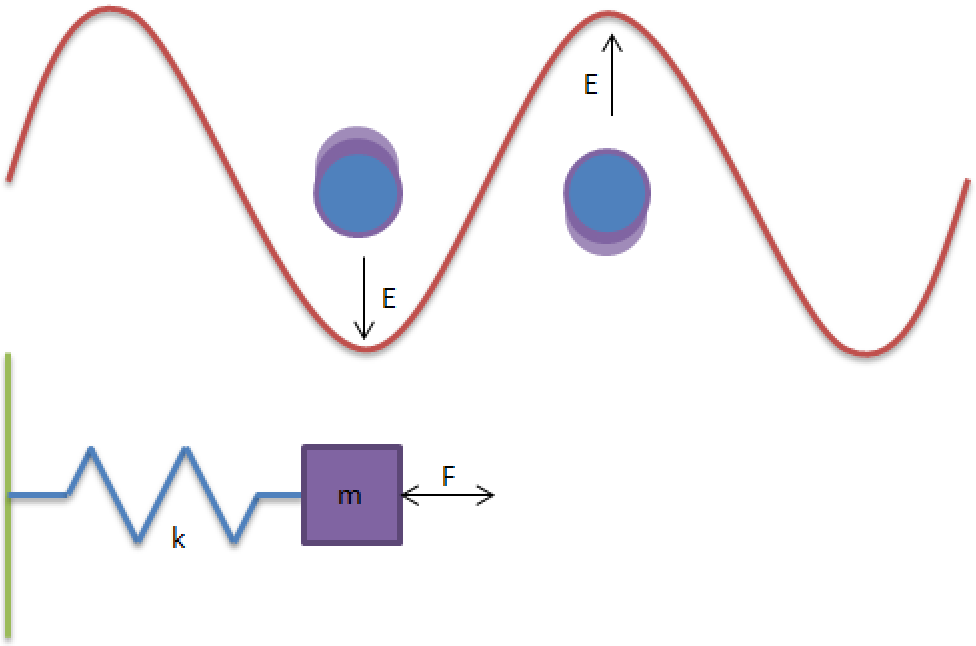

Figure 2.4. Diagram showing the analogous, force-induced oscillations of LSP from a mNP subjected to an electromagnetic field and a simple, spring-mass system subjected to an external driving force.

The ability of mNP to convert energy in the form of light to LSP has caused them to be referred to as nanoantennas[36-41]. Like antennas on the macroscale, nanoantennas can collect energy from a large volume and confine it to a much smaller volume, much smaller than the wavelength. In doing so, the electromagnetic field is highly enhanced in these regions, commonly referred to as 'hot-spots'[42-47]. The high-intensity field in these regions can be coupled to a fluorophore to increase the excitation rate and, through the law of reciprocity, similarly increase the emission rate[48]. The effect of LSP on the fluorescence process is referred to as surface-enhanced fluorescence (SEF).

2.4. SURFACE-ENHANCED FLUORESCENCE

SEF has been studied for decades, though it only recently became widespread in the research community. The formation of the SEF research field seems to have been a gradual progression, as opposed to a research track launched from a seminal manuscript. The interaction of light with nanoparticles dates back to Lord Rayleigh at the end of the 19th century[49, 50] with studies involving the absorption and scattering of sunlight by particles in the atmosphere, much smaller than the wavelength of light (i.e. a few nm or less), which generate the blue sky hue. Mie later solved for an analytical solution of light interaction with spherical nanoparticles similar in size to the wavelength[51], based on Maxwell's equations . This pioneering work is still frequently used in modern-day plasmonics research as many plasmon-active nanostructures are indeed spherical nanoparticles similar in size to the wavelength of light. Perhaps the first SEF-like research can be credited to Purcell who found that the radiative decay of an emitter can be affected by the environment[52]. Specifically, Purcell demonstrated the enhancement of spontaneous emission rates of atoms in small resonant cavities with a dependence on the quality factor and mode volumes. Kleppner later found that the environment could inhibit or enhance the radiative decay depending on if the characteristic dimension of the cavity is small or resonant with the emission wavelength, respectively[53]. Once the related phenomenon of surface-enhanced Raman scattering (SERS)[54, 55] became popular in the research community the interest in the use of nanoparticles to enhance optical detection gained momentum.

SERS is the phenomenon of enhanced Raman scattering due to an increased local electromagnetic field near a plasmon-active nanostructure. When a molecule scatters light, most of the energy is elastically scattered (at the same wavelength); however, a small portion is inelastically scattered at various wavelengths depending on the chemical structure of the molecule. This inelastic scattering is known as Raman scattering and is important because it enables label-free detection of individual molecules due to unique Raman signatures (scattering spectra). Unfortunately, Raman scattering occurs at extremely low intensity and is often undetectable. SERS is an important research field as it enables the benefits of Raman scattering within a detectable level of energy; however, even with enhancement the scattering intensity rarely approaches a level close to the emission of a fluorescent dye[54], which thus inhibits the wide-spread adoption of the SERS technique in bioassays.

SEF combines the electromagnetic field enhancement demonstrated in SERS with enhanced emission rates due to the Purcell effect. Early works included the formation of a Purcell cavity by placing fluorophores near mirrored surfaces[56]. The Lakowicz group at Maryland can be credited for re-energizing the field of SEF in the early 2000s when the term radiative decay engineering (RDE) was coined in a series of manuscripts[57-61]. RDE was introduced with a thorough description of the fluorescence process and how it can be modified by nearby plasmon-active substrates[57]. Importantly, the explanations and language were inviting to researchers in the fluorescence field, as opposed to previous work by physicists, which may have assisted in the acceleration of progress. The effects of silver island films (SIF) on the quantum yield and radiative decay rates of common visible dyes were presented[58]. SIF are random, nanoscale clusters of solid silver formed on glass substrates by deposition of silver nitrate solution. Next, the isotropic emission of fluorophores where found to become directional when placed near thin metal films[59]. This directional emission phenomena was further studied experimentally and found to enable 50% collection efficiency of the emitted light[60]. Research efforts were then directed back towards nanostructure effects when it was proposed that fluorescence quenching could be expected for small nanoparticles dominated by absorption, while fluorescence enhancement could be expected for larger nanoparticles able to scatter light into the far-field[61]. At this point in time, the understanding was that plasmon-active nanostructures and surfaces could enhance or quench the fluorescence process via increased decay rates, though the exact mechanism had not been determined. The decay rates were thought to depend on the intrinsic quantum yields and distance from the metal surface, which was suggested to be optimized at 10-100 nm. Further contributions made it clear that RDE was a misleading description of the process as a change in the radiative decay rate is only part of the process[62], thus the term SEF was born. SEF has also been frequently referred to as metal-enhanced fluorescence[63-72] (MEF). The field of SEF has expanded significantly in the last decade and many review papers have been published[62, 69, 73-75], as well as books[76, 77].

More thorough reviews of the process have been published[62, 74, 78, 79]; however, a brief summary of the current theory is provided. Fluorescence in free space can be described by the relationship between intrinsic rates of emission (γ_{em}^{0}), excitation (γ_{ex}^{0}), radiative decay (γ_{r}^{0}), and non-radiative decay (γ_{nr}^{0})[1]

$$\gamma_{\mathrm{em}}^{0} = \gamma_{\mathrm{ex}}^{0}\frac{\gamma_{\mathrm{r}}^{0}}{\gamma_{\mathrm{r}}^{0} + \gamma_{\mathrm{nr}}^{0}} \qquad (4)$$

When in close proximity to a plasmon-active nanostructure, the excitation (γ_{ex}) and radiative (γ_{r}) decay rates are increased and an additional non-radiative decay path (γ_{nr}) is introduced giving a new emission rate (γ_{em})[80-82]

$$\gamma_{\mathrm{em}} = \gamma_{\mathrm{ex}} \frac{\gamma_{\mathrm{r}}}{\gamma_{\mathrm{r}} + \gamma_{\mathrm{nr}} + \gamma_{\mathrm{nr}}^{0}} \qquad (5)$$

SEF can thus be described by

$$\mathrm{SEF} = \frac{\gamma_{\mathrm{em}}}{\gamma_{\mathrm{em}}^{0}} = \frac{\gamma_{\mathrm{ex}}}{\gamma_{\mathrm{ex}}^{0}} \frac{\gamma_{\mathrm{r}}/\gamma_{\mathrm{r}}^{0}}{(\gamma_{\mathrm{r}} + \gamma_{\mathrm{nr}} + \gamma_{\mathrm{nr}}^{0})/(\gamma_{\mathrm{r}}^{0} + \gamma_{\mathrm{nr}}^{0})} \qquad (6)$$

and more conveniently in terms of the intrinsic (q^{0}) and enhanced (q) quantum yields as

$$\mathrm{SEF} = \frac{\gamma_{\mathrm{ex}}}{\gamma_{\mathrm{ex}}^{0}} \frac{\mathrm{q}}{\mathrm{q}^{0}} \qquad (7)$$

Thus, SEF is simply the combination of enhanced excitation rate and quantum yield; however, the theory is more complicated when breaking down the individual components of these processes. Since quantum yield cannot exceed unity, fluorophores with high intrinsic quantum yields can only be notably enhanced by an increased excitation rate. A local increase in field intensity is responsible for the enhanced excitation rate as well as any improvement in quantum yield, and is dependent on material properties, nanostructure geometry, dipole emitter orientation, and distance between the emitter and the nanostructure[78, 79]. Of these parameters, the most straightforward to control is the material. The quality factor (Q) is a material-dependent property that describes the number of plasmon oscillations prior to field decay and can be calculated by[79]

$$\mathrm{Q} = \frac{\omega}{2\gamma} \approx \frac{\omega \frac{\delta}{\delta\omega} (\mathrm{Re}\{\varepsilon_m(\omega)\})}{2\mathrm{Im}\{\varepsilon_m(\omega)\}} \qquad (8)$$

where ω is the angular frequency (eV), γ is the decay rate (eV), and ε_m is the complex permittivity of the material. The calculated quality factors for Ag and Au from visible to NIR wavelengths are shown in Figure 2.5. Based on Q alone, Ag is predicted to outperform Au at all visible and NIR wavelengths, while both Ag and Au are maximized in the NIR. It is important to note that the relative trend of Q may be useful; however, a quantitative value should be used cautiously. The commonly used optical properties of Ag and Au contain a margin of error approaching the magnitude of the measured values[35] (this is especially true for the imaginary index of refraction for Ag which is near zero at particular frequencies). This error propagates into the calculation of Q but is rarely considered in the literature. Figure 2.5 also shows the resonant plasmon wavelengths for Ag and Au spherical nanoparticles under the quasi-static approximation, where free electrons can be treated as an incompressible fluid that oscillate collectively as a dipole[83]. The plasmon resonance shifts when the nanostructure geometry is larger and no longer negligible in size compared to the wavelength of excitation. Nanostructures experience maximum polarizability at their plasmon wavelengths leading to the strongest, plasmon-induced, increase in field intensity. The increased electromagnetic field intensity may be the reason that various nanostructures have been selected to match the excitation or emission wavelength of the fluorophore in many SEF studies[82, 84-87]. This reasoning can be misleading though, since γ_{nr} is also maximized at the plasmon frequency. Therefore, the optimal wavelength for SEF is not necessarily at the plasmon resonance[83] and may occur at significantly red-shifted wavelengths where Q is maximized. Beyond the relatively low intrinsic quantum yields, the relatively large Q value may explain the magnitude of enhancement found only in the NIR thus far.

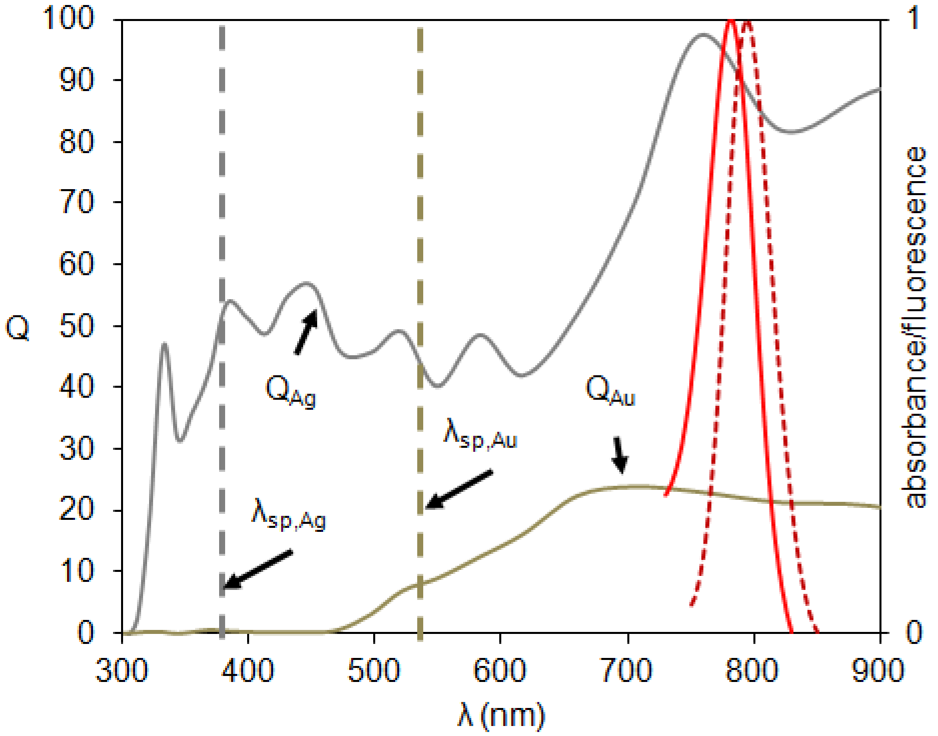

Figure 2.5. Calculated quality factor (Q) for Ag and Au as a function of wavelength. The surface plasmon wavelengths (λsp) of spherical nanoparticles, under the quasi-static approximation, are shown along with the normalized absorbance and emission curves of IRDye 800CW.

As mentioned above, theoretical calculations based on commonly accepted experimental values should be used with caution. Q for Ag is shown in Figure 2.6 with error bars corresponding to those published in a commonly used reference[35]. While many plasmonic calculations do not require Q explicitly, they all depend on the complex permittivity values of which Q is based. To the authors' knowledge, there are no known examples in the literature where this error margin has previously been discussed.

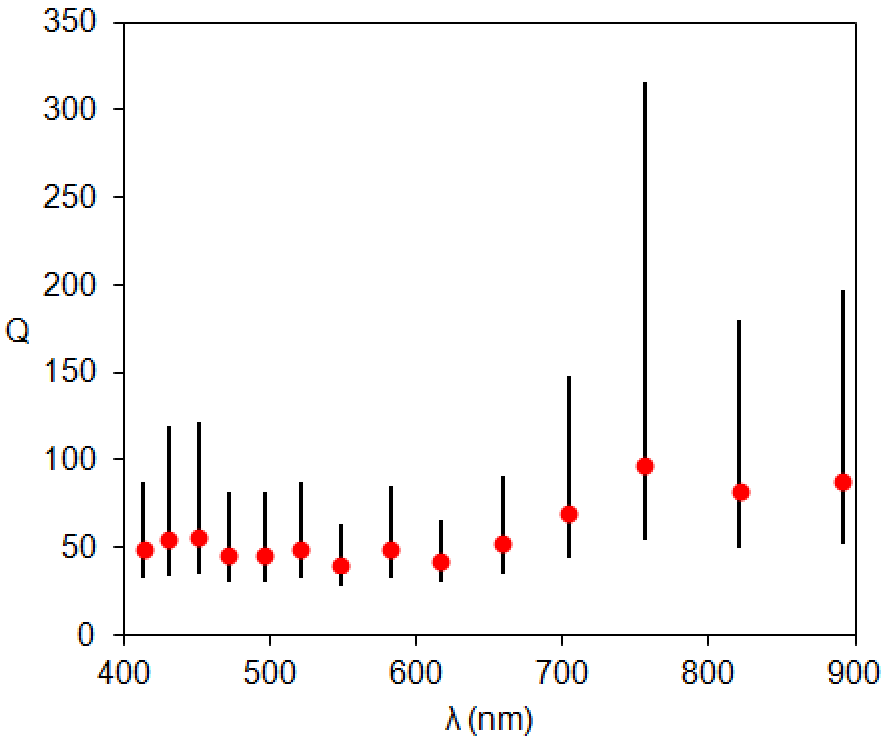

Figure 2.6. Quality factor for Ag with error bars (using experimental margin of error[35]).

2.6. NEAR-INFRARED, SURFACE-ENHANCED FLUORESCENCE

NIR-SEF has received relatively little attention compared to SEF with visible fluorophores in the literature. NIR-SEF has been demonstrated with silver nanostructures on surfaces[88-91], gold nanostructures on surfaces[28, 92, 93], and gold nanoparticles in solution[87, 94-96]. Initially, NIR-SEF was studied for the potential enhancement of *in vivo* imaging[90, 91] by applying SEF to the only FDA cleared fluorophore for use in humans, indocyanine green (ICG). Enhancement to signal intensity with ICG of 20-fold[91] and 30-fold[90] were demonstrated on SIF and AgNP on glass, respectively. This initial enhancement using NIR fluorescence was promising as the enhancement found with visible fluorophores is typically 10-fold or less. Later, Anderson et al. demonstrated that the advantages of NIR fluorescence in general, such as low background and autofluorescence, could be combined with the SEF technology[88, 89, 97]. SIF were used to demonstrate 18-fold enhancement of IRDye 700 and 15-fold enhancement of IRDye 800CW[88]. Colloid-coated surfaces turned out to be less effective with only 5-fold enhancement of IRDye 700 and 11-fold enhancement of IRDye 800CW[89]. A breakthrough occurred when substantially larger enhancement of IRDye 800CW was found using highly-concentrated, citrate-stabilized AgNP (unpublished), fabricated using a proprietary adaption to common methods[98, 99]. Further research determined that nanoparticle interactions, or aggregation, may be responsible for the enhancement. Aggregates of AgNP were formed in solution and deposited on glass slides to enhance the fluorescent signals of Alexa Fluor 680 and IRDye 800CW by over 200-fold and 100-fold, respectively[89]. Citrate-stabilized AgNP are typically stable due to the negatively charged citrate ions on the surfaces, which prevent collisions between individual AgNP. The addition of salt can screen the surface charges and allow interaction between the AgNP, hence forming aggregates. A design of experiments method was conducted to optimize the citrate-stabilized AgNP for enhancement of IRDye 800CW-labeled SAv in solution and applied to a FLISA assay[100]. At this point, significant enhancement of IRDye 800CW could be demonstrated; however, further insight into the physical mechanisms was needed to convey the results to the broader scientific community and enable further optimization. Recently, NIR-SEF on a surface of gold nano-pillars demonstrated enhancements of 2970-fold[101] and 7400-fold[102] (by far the largest ensemble enhancements, at any wavelength, ever published to the author's knowledge). The 7400-fold enhancement using IRDye 800CW[102] was greater than 10X improvement over previous work using the same dye[88, 89, 92, 95]. These recent contributions demonstrate substantial improvement in fluorescence sensitivity using NIR fluorophores; however, they are limited to surface-based assays and are not pertinent to real-world applications.

2.7. LIMITATIONS OF CURRENT TECHNOLOGY

Despite promising progress in NIR-SEF there are no known commercially available assay kits, or researchers from outside the plasmonic community able to implement these techniques to improve assay sensitivity and/or LOD. The lack of technology transfer and adoption may be due to the expense and expertise needed to fabricate these nanostructures and/or the modifications required of traditional assay preparation formats and workflows. The surface-based technology developed in the Chou lab at Princeton[101, 102] may eventually provide improved assay sensitivity; however, it does not address the need for a solution-based platform and would likely be displaced if a simple solution provided the same (or even similar) enhancement. The solution-based strategy investigated by Anderson et al. at LI-COR has the potential to fill this gap; however, it requires further discovery to interpret the mechanisms involved with the goal of maximizing sensitivity and minimizing complexity. In this dissertation, these problems are addressed by advancing the fundamental understanding of NIR-SEF, while demonstrating significant enhancement using simple-to-fabricate AgNP in solution. This contribution may enable life science researchers to incorporate NIR-SEF in their current fluorescence-based assays in order to address the need of enhanced sensitivity and/or improved LOD.

CHAPTER 3. SURFACE-ENHANCED FLUORESCENCE WITH VISIBLE AND NEAR-INFRARED FLUOROPHORES IN SOLUTION

3.1. INTRODUCTION

It is commonly accepted in the literature that fluorophores having absorption and/or emission spectra that overlap with the resonant frequency of a plasmon-active nanostructure demonstrate the greatest SEF. Successful implementations of SEF using this logic have been demonstrated in several publications; however, the studies have often required experiments on a surface and/or measurement at the single nanostructure level[85, 86, 103], as opposed to ensemble measurements including many fluorophores and many plasmon-active nanostructures. Solution-based SEF has been demonstrated using NIR fluorophores[100]; however, it remains unclear if visible fluorophores can provide similar, or better, levels of enhancement as suggested by the commonly accepted spectra overlap theory. It is hypothesized that a correlation between fluorophore spectra and nanostructure resonance may not be ideal when using a concentrated solution of mNP as the plasmon-active substrate. It is expected that a competition between signal enhancement and signal attenuation[104, 105] (or inner-filter effect[106, 107]) may ultimately lead to a negative relationship between nanostructure resonance and SEF with increasing concentration of mNP. Further, it is hypothesized that the quality factor may be an important material property to determine the ability to generate substantial SEF. It has been previously suggested that maximum fluorescence enhancement may not always occur near the resonant frequency of the nanostructure due to absorption[83]; however, it has not been demonstrated in the literature to the author's knowledge. Recently, it was shown that the related phenomenon of surface-enhanced Raman scattering (SERS) may also occur at excitation wavelengths significantly red-shifted from the resonant frequency of the nanostructure[108, 109]. Further, like SERS, SEF is dominated by light interactions in 'hot spots' which may contain active spectra that differ from the ensemble measured absorbance[110]. Here, we use theoretical analysis along with experimental data to test the hypotheses that (1) inner-filtering (or reabsorption of the emitted light by the plasmon-active nanostructure) may red-shift the optimal fluorophore spectra away from the resonant frequency of the plasmon-active nanostructure and (2) that in some cases, the quality factor may be a more important predictor of SEF as opposed to the nanostructure resonance indicated by the absorbance spectra.

3.2. MATERIALS AND METHODS

Materials. Alexa Fluor 488 and Alexa Fluor 594 were purchased pre-conjugated with SAv (Life Technologies, Grand Island, NY). IRDye 680LT and IRDye 800CW were acquired pre-conjugated with SAv (LI-COR, Lincoln, NE). Unlabeled SAv was purchased in solution (Life Technologies, Grand Island, NY). AgNP were acquired at a stock concentration of ~ 20 nM with an average diameter of ~ 20 nm (LI-COR, Lincoln, NE). All dilutions were performed with ultrapure water from a Milli-Q system

(Millipore). All reagents were used as received and handled per the manufacturer's instructions, unless otherwise noted.

Absorbance measurements. Absorbance measurements were made on an Agilent 8453 UV-Visible spectrophotometer (Agilent Technologies Inc., Santa Clara, CA). All SAv-fluorophore conjugates were measured in PBS at a concentration of approximately 1 μg/ml. The actual fluorophore concentration varies for each conjugate solution due to variation in the degree of labeling (dye molecules per SAv molecule). It is assumed that the actual fluorophore concentration is not important since all measurements are relative and conducted as ensemble averages. Absorbance of AgNP was measured after diluting the stock solution 10-fold to be within the linear range of the spectrophotometer.

Fluorescence measurements. Fluorescence emission spectra were acquired using a QuantaMaster spectrofluorometer (Photon Technology International, Birmingham, NJ). Figure 3.1 shows a schematic of the spectrofluorometer system and components. All measurements were conducted with all slits opened 2 full turns on the adjustment knobs, which corresponds to a slit-width of 1 mm. A high-pass filter was placed in front of the detector to reduce undesired scatter from the excitation diffraction grating. The cut-off frequency of the filter was 450 nm for Alexa Fluor 488 and 500 nm for all other fluorophores. Labeled and unlabeled SAv were mixed with various concentrations of AgNP by adding 2 ml of 2 nM SAv-conjugate to 2 ml of AgNP solution in optical-grade poly(methyl methacrylate) cuvettes and incubated for 4 hours in the dark at room temperature. Each sample was carefully inverted three times prior to measurement to suspend any large aggregates that may have settled over time. All fluorescence spectra involving AgNP were corrected with background subtraction using a cuvette with identical contents minus the fluorophore. For example, 2 nM dye labeled SAv with 20 nM AgNP was corrected by subtracting the corresponding spectrum of 2 nM unlabeled SAv with 20 nM AgNP.

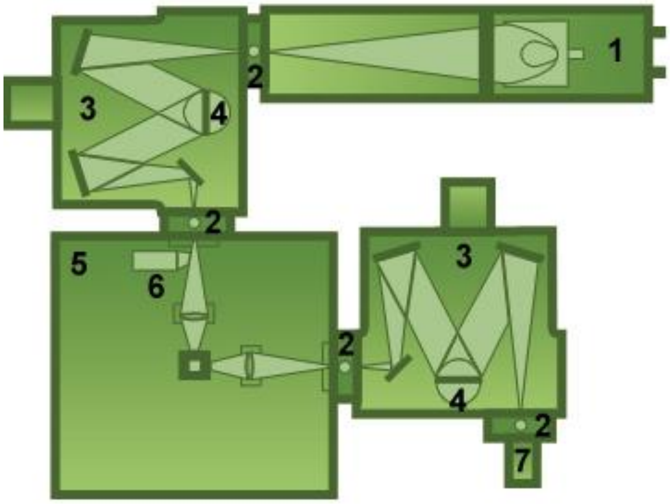

Figure 3.1. Schematic of spectrofluorometer components including: (1) light source, (2) adjustable slits, (3) excitation and emission monochromator, (4) excitation and emission grating, (5) sample compartment, (6) excitation correction, and (7) detector. Copyright Photon Technology International, Inc.

3.3. RESULTS AND DISCUSSION

Fluorophore characterization. The intrinsic absorbance and emission spectra were acquired for each fluorophore (Figure 3.2). In general, the absorbance and emission maxima occurred at, or very close to, the manufacturers' published values (Table 3.1). The four chosen fluorophores provide a sample spanning 300 nm in wavelength (500 to

800 nm) with nearly even spacing of 100 nm between each. The range was chosen to include a fluorophore very close to the resonant frequency of the AgNP solution near 500 nm all the way to 800 nm where there is minimal attenuation of light and a maximized quality factor (see Figure 3.2). The absorbance spectrum of the AgNP solution is broader than expected with Mie theory due to the presence of large particles within the polydisperse sample.

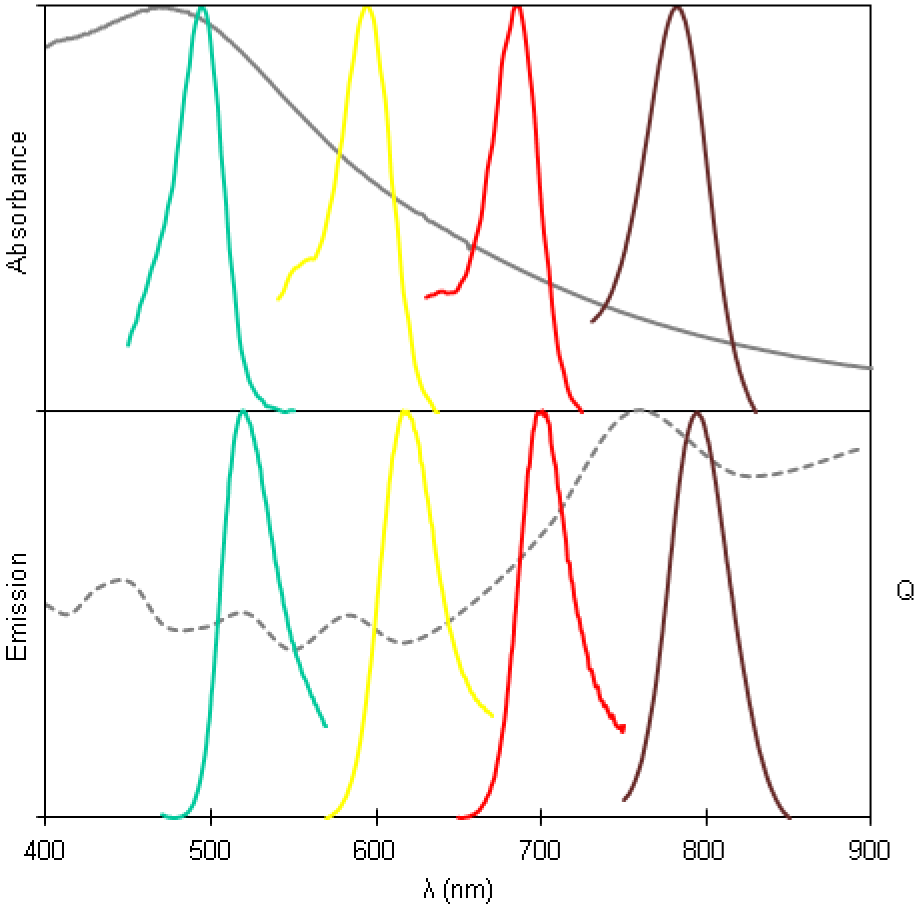

Figure 3.2. Top: Normalized absorbance of AgNP (gray), Alexa Fluor 488 (cyan), Alexa Fluor 594 (yellow), IRDye 680LT (red), and IRDye 800CW (purple). Bottom: Normalized quality factor (gray, dashed) and corresponding emission curves for each fluorophore.

Table 3.1. Properties of fluorophores used in this work (per manufacturers' websites).

Fluorophore	$\lambda_{abs,max}$ (nm)	$\lambda_{em,max}$ (nm)	$\varepsilon_{\lambda abs,max}$ (M^{-1} cm^{-1})	QY
Alexa Fluor 488	496	519	71000	0.92
Alexa Fluor 594	590	617	73000	0.66
IRDye 680LT	680	694	250000	0.19
IRDye 800CW	778	794	240000	0.07

Theoretical calculations. The spectral and distance dependent enhancement of fluorophores near a mNP can be calculated using the multi-multipole (MMP) theory[84]. Assuming the dipole moment of the fluorophore is normal to the mNP (best case for SEF) the modified emission rate, γ_{em}, can be calculated by

$$\frac{\gamma_{em}}{\gamma_{em}^{0}} = \frac{\gamma_{exc}}{\gamma_{exc}^{0}} \frac{q}{q^{0}} \qquad (1)$$

where γ_{em}^{0} is the emission rate far from the mNP, γ_{exc} is the modified excitation rate, and q is the modified quantum yield. The excitation rate far from the mNP and intrinsic quantum yield are denoted with the superscript '0'. The modified excitation rate can be calculated by

$$\frac{\gamma_{exc}}{\gamma_{exc}^{0}} = \left|1 + 2\frac{a^{3}}{(a+z)^{3}} \frac{\varepsilon(\lambda_{exc}) - 1}{\varepsilon(\lambda_{exc}) + 2}\right|^{2} \qquad (2)$$

where a is the diameter of the mNP, z is the distance between the fluorophore and the surface of the mNP, and $\varepsilon(\lambda_{exc})$ is the complex permittivity of the mNP at the excitation wavelength. The modified quantum yield can be calculated based on the enhancement of the radiative decay rate, γ_r/γ_r^0, and the non-radiative decay rate, γ_{nr}, using

$$q = \frac{\gamma_r/\gamma_r^0}{\gamma_r/\gamma_r^0 + \gamma_{nr}/\gamma_r^0 + (1 - q^0)/q^0} \qquad (3)$$

$$\frac{\gamma_r}{\gamma_r^0} = \left|1 + 2\frac{a^3}{(a+z)^3}\frac{\varepsilon(\lambda_{em}) - 1}{\varepsilon(\lambda_{em}) + 2}\right|^2 \qquad (4)$$

$$\frac{\gamma_{nr}}{\gamma_r^0} = \frac{3}{8}\mathrm{Im}\frac{\varepsilon(\lambda_{em}) - 1}{\varepsilon(\lambda_{em}) + 1}\frac{1}{k_{em}^3 z^3} \qquad (5)$$

where k_{em} and $\varepsilon(\lambda_{em})$ are the circular frequency and complex permittivity of the mNP at the emission wavelength. When the Stokes-shift of the fluorophore is small, equations (2) and (4) are essentially equal due to the law of reciprocity. This means that a mNP acting as a nano-antenna performs equally well as a collector of light and emitter of light[48].

The trouble with SEF using mNP in solution is that along with possibly enhancing the fluorescence of a nearby emitter, they may also cause attenuation of the excitation light and/or emitted energy of fluorophores far away. The absorption, scattering, and extinction cross sections of mNP are given by[83]

$$C_{abs} = k\mathrm{Im}[\alpha] = 4\pi k a^3 \mathrm{Im}\left[\frac{\varepsilon - \varepsilon_m}{\varepsilon + 2\varepsilon_m}\right] \qquad (6)$$

$$C_{sca} = \frac{k^4}{6\pi}|\alpha|^2 = \frac{8\pi}{3}k^4 a^6 \left|\frac{\varepsilon - \varepsilon_m}{\varepsilon + 2\varepsilon_m}\right|^2 \qquad (7)$$

$$C_{ext} = C_{abs} + C_{sca} = 9k{\varepsilon_m}^{3/2}V\frac{\varepsilon_2}{[\varepsilon_1 + 2\varepsilon_m]^2 + {\varepsilon_2}^2} \qquad (8)$$

where α is the polarizability of the mNP, k is the wavenumber (in the surrounding medium), ε_m is the permittivity of the medium surrounding the mNP, and the complex permittivity of the mNP is $\varepsilon = \varepsilon_1 + i\varepsilon_2$. Using the extinction cross section from equation (8) and the number of mNP per unit volume one can obtain the average reduction in signal for a homogeneously dispersed mix of fluorophores as

$$A = NLC_{ext} \qquad (9)$$

$$I = I_0 10^{-NLC_{ext}} \qquad (10)$$

$$S = \frac{1}{L}\int_0^L 10^{-NC_{ext}z}dz = \frac{1 - 10^{-NLC_{ext}}}{NLC_{ext}ln10} \qquad (11)$$

where A is the absorbance, N is the number of mNP per unit volume, L is the total depth of the sample, I is the intensity, I_0 is the intensity prior to entering the sample, and S is the integrated average value of the intensity relative to I_0.

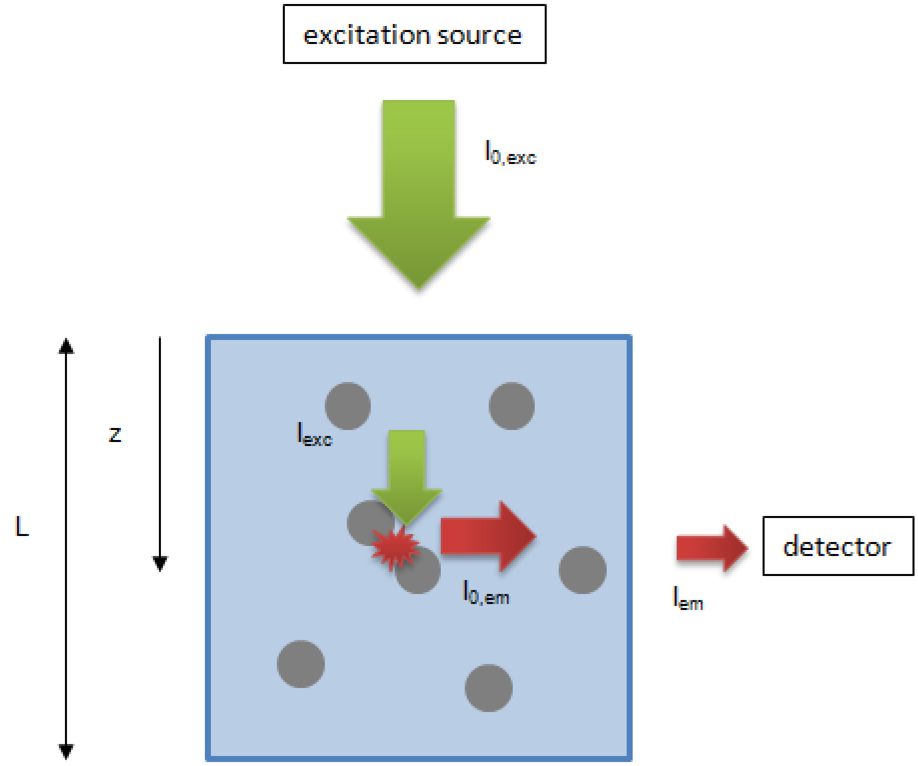

Figure 3.3. Schematic of fluorescence measurement using spectrofluorometer with direction of detection normal to excitation. The green arrows show a decrease in excitation intensity due to attenuation by mNP. The red arrows show a similar decrease in emission intensity also due to attenuation.

Taking the optical properties as equivalent for the excitation and emission wavelength (assuming a small Stokes shift), using equations (1) through (11), the 'observed' fluorescence enhancement for the schematic in Figure 3.3 becomes

$$SEF_{obs} = S^2 \frac{\gamma_{em}}{\gamma_{em}^0} \qquad (12)$$

Combining equations (1) through (12), the wavelength dependent SEF is shown in Figure 3.4. Optical properties of Ag were taken from published data[35], the radius of the mNP (a) was held constant at 10 nm, and the calculations were averaged for distances (z) of 1 to

10 nm in increments of 1 nm. SEF with minimal impact from attenuation is calculated at a mNP concentration (N) of 1 x 10^8 μl^{-1} and a sample depth (L) of 0.1 mm. With negligible attenuation, or inner-filtering, the theoretical enhancement is maximized near the resonant frequency of the mNP (~ 400 nm in water). Increases in the concentration of mNP and/or sample depth dramatically change the curve such that the resonant frequency produces the lowest observed enhancement. In this situation, the observed enhancement increases with wavelength where attenuation is minimal but quality factor is maximized. Also, note that the theoretical enhancement in the NIR is independent of mNP concentration or sample depth due to negligible inner-filtering or attenuation.

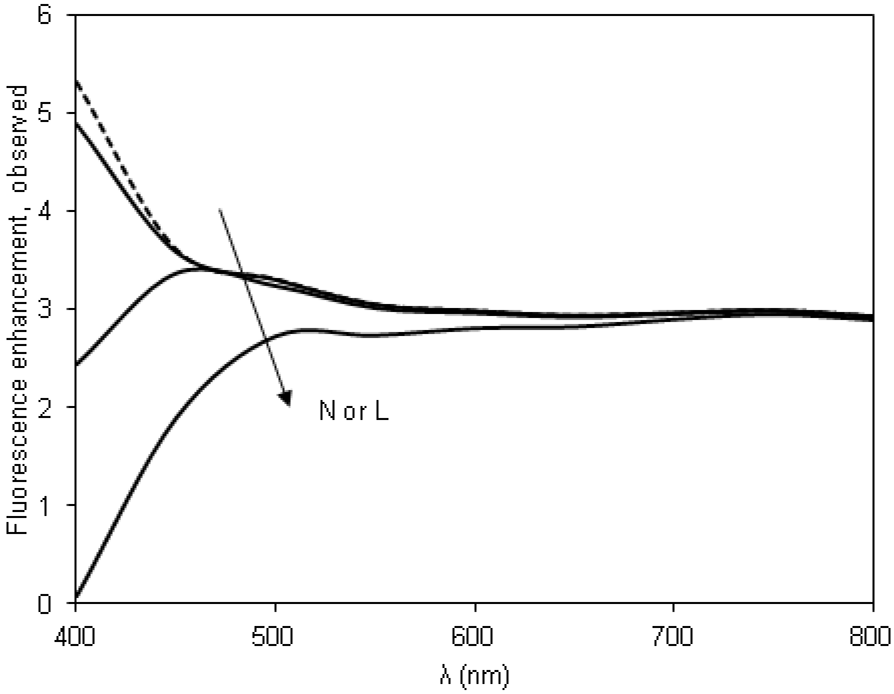

Figure 3.4. Theoretical fluorescence enhancement (observed) as a function of wavelength for negligible light attenuation (dotted line) and order of magnitude increases in mNP concentration (N) or sample depth (L).

Experimental results. Experiments were conducted to test the hypothesis that observed SEF is maximized near the resonant frequency when attenuation is negligible and shifts toward maximized quality factor (Q) when attenuation is significant. Figures 3.5 through 3.9 show fluorescence intensity versus wavelength for the four fluorophores in this study. Each fluorophore was measured without AgNP and with AgNP at concentrations of 0.01X (0.2 nM), 0.1X (2 nM), and 1X (20 nM). The fluorophore concentration was held constant at 2 nM for all experiments except for IRDye 800CW without AgNP. This signal was extremely low due to a lack of sensitivity of the detector at long wavelengths along with the low intrinsic quantum yield of the fluorophore;

therefore, the fluorophore was measured at 20 nM for the IRDye 800CW sample without AgNP (see Figure 3.8).

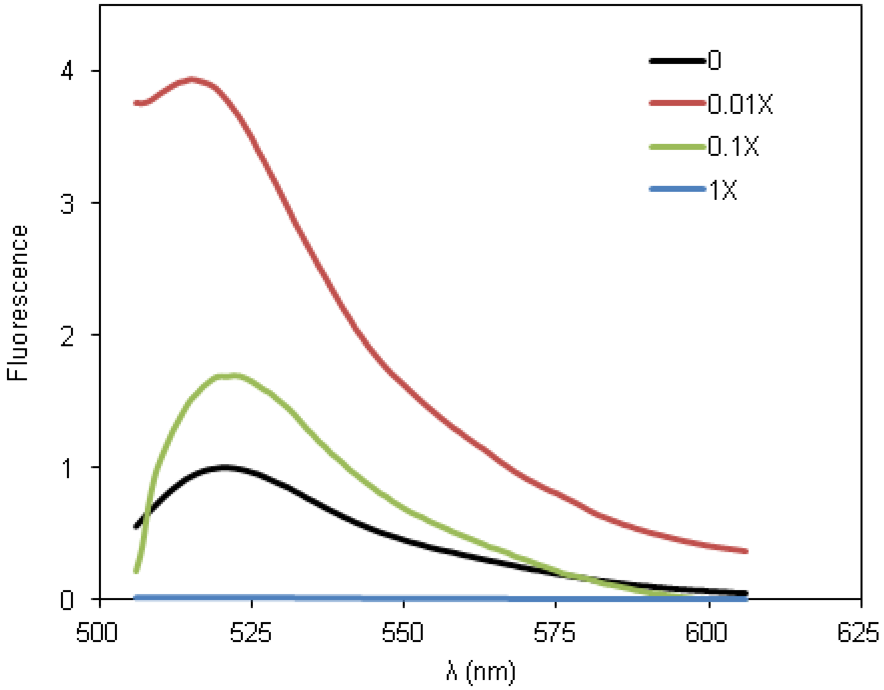

Figure 3.5. Measured fluorescence of Alexa Fluor 488 labeled SAv with various concentrations of AgNP. Each curve represents the average of three measurements with background subtracted.

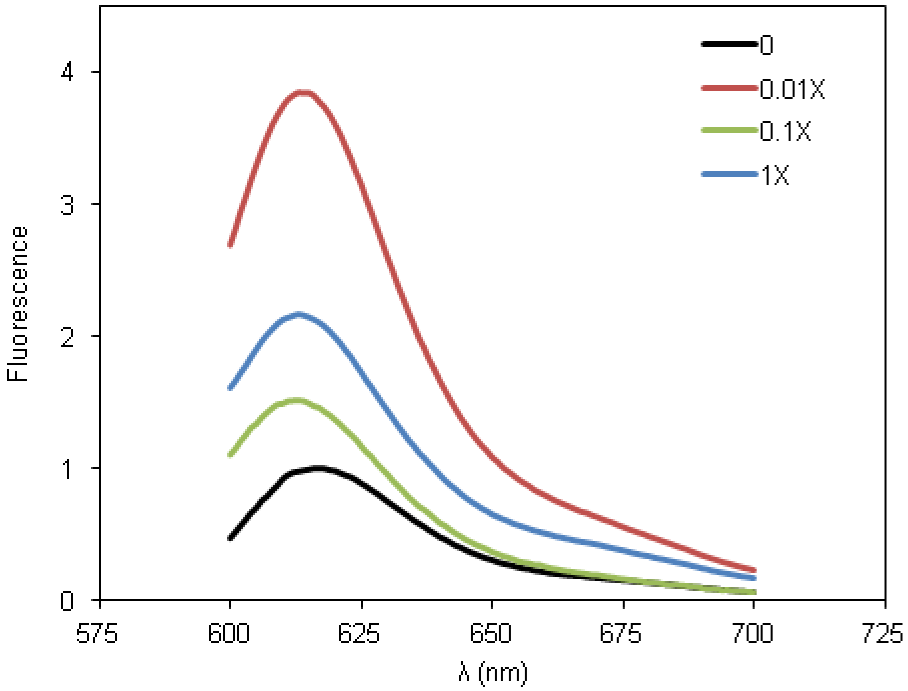

Figure 3.6. Measured fluorescence of Alexa Fluor 594 labeled SAv with various concentrations of AgNP. Each curve represents the average of three measurements with background subtracted.

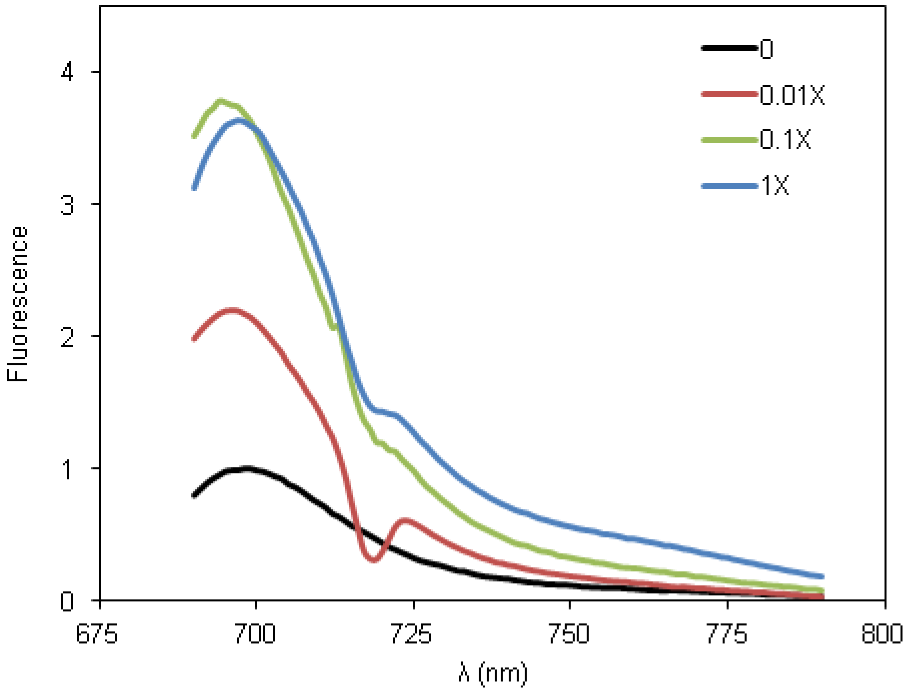

Figure 3.7. Measured fluorescence of IRDye 680LT labeled SAv with various concentrations of AgNP. Each curve represents the average of three measurements with background subtracted.

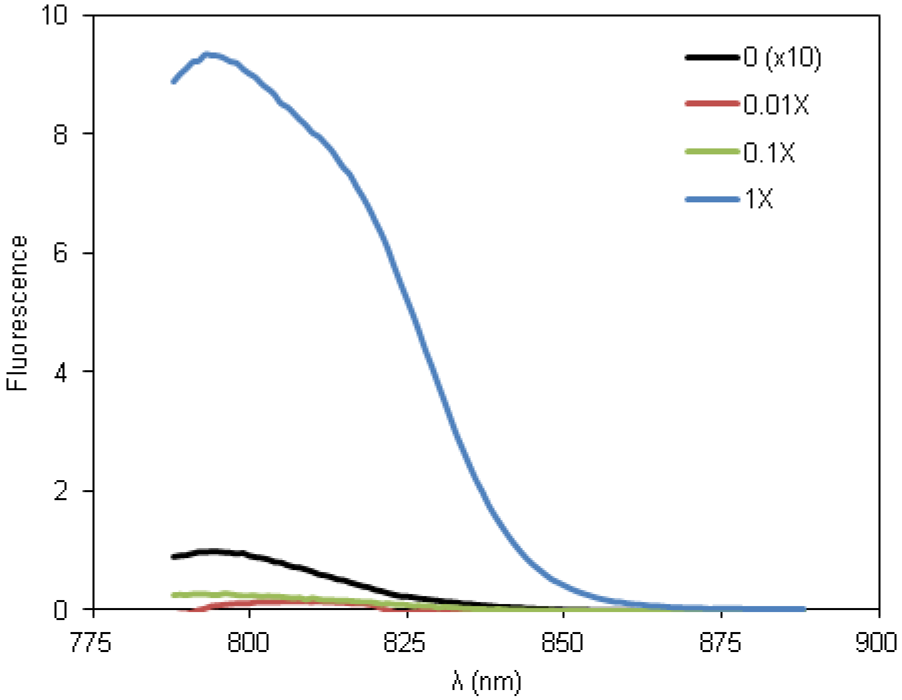

Figure 3.8. Measured fluorescence of IRDye 800CW labeled SAv with various concentrations of AgNP. Each curve represents the average of three measurements with background subtracted.

The results for all fluorophores are summarized in Figure 3.9. Alexa Fluor 488 showed enhancement with 0.1X AgNP that was reduced upon further addition of AgNP. This may be due to the large attenuation of excitation and emission light with high concentrations of AgNP. The fluorescence signal was reduced almost 100-fold at 1X AgNP. Alexa Fluor 594 and IRDye 680LT showed modest enhancement at all concentrations of AgNP, which may indicate a balance between SEF and attenuation. IRDye 800CW showed a slight reduction in fluorescence at the lowest concentration of AgNP and large enhancement upon further addition of AgNP. The slight reduction at 0.01X AgNP is unexpected and may be due to error associated with very low signal.

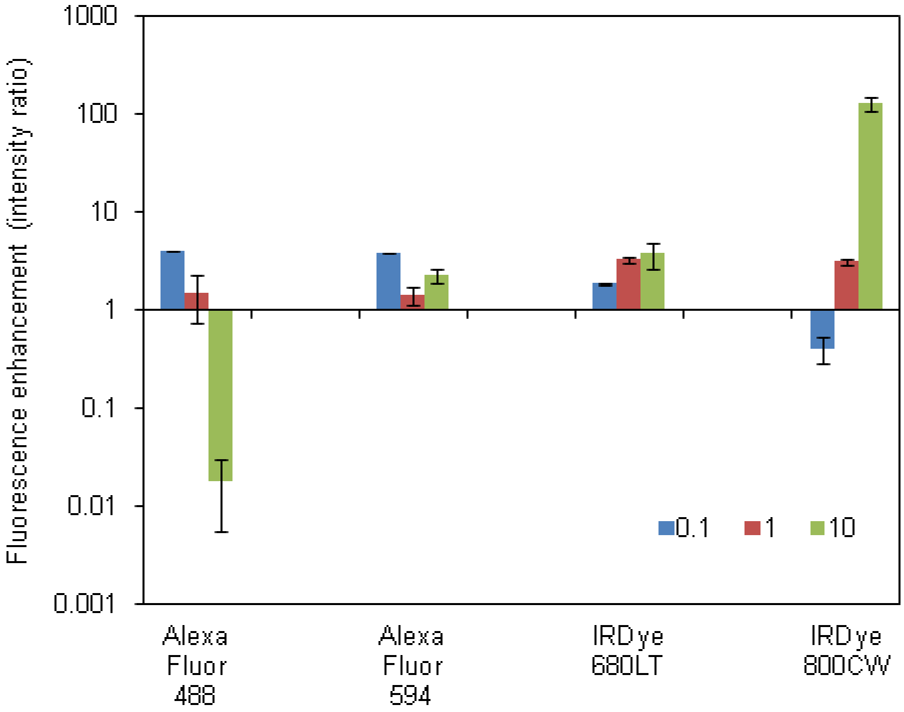

Figure 3.9. Fluorescence enhancement for each fluorophore at various molar ratio of AgNP:SAv-fluorophore. Error bars indicate +/- one standard deviation.

Combining experimental results with theory. The theoretical analysis and experimental data are in reasonable qualitative agreement; however, there is further explanation warranted to synchronize the evidence towards the hypothesis. There are four main causes for prevention of quantitative agreement between the experimental data and the theoretical analyses. First, the AgNPs are not monodisperse as the theory requires. In fact, they are quite polydisperse. Second, the polydisperse AgNP solution contains significant numbers of particles that do not fall within the quasi-static limit (i.e. they are not negligible in size compared to the wavelength of light). The presence of large particles is also the reason that the measured AgNP absorbance is significantly red-shifted from the theoretical peak. Third, each fluorophore has a different quantum yield which is expected to have a significant impact on the potential of fluorescence enhancement, regardless of the wavelength. Finally, the theoretical analysis does not take into account the changes in local field intensity due to multiple AgNP attached to the SAv molecule, which is expected to occur (see Chapter 4). Further, the number of dimers and higher-order aggregates formed by AgNP and the SAv molecules is expected to increase with the concentration of AgNP.

Most of the listed limitations for quantitative comparison are irreconcilable; however, the quantum yield of each fluorophore can be found in the literature. Equation 1 shows that, on a first-order approximation, the intrinsic quantum yield is inversely proportional to the fluorescence enhancement. Therefore, the contribution of the intrinsic quantum yield can be eliminated and the contribution of the local field intensity estimated by correcting for quantum yield. This correction is achieved by simply multiplying the observed SEF by the intrinsic quantum yield. As an example, if an emitter had a quantum yield of 0.5, than the approximation is that the local field intensity must be responsible for at least 50% of the enhancement. Figures 3.10 and 3.11 show the fluorescence enhancement corrected for quantum yield for AgNP:SAv-fluorophore molar ratios of 0.1 and 10, respectively. Figure 3.10 demonstrates that at low AgNP:SAv ratios, the accepted theory holds that SEF is maximized near the resonant frequency of the mNP (demonstrated by absorbance). Figure 3.11 demonstrates that at high AgNP:SAv ratios the accepted theory is no longer correct and SEF becomes maximized in the NIR where the quality factor is also maximized. Further, the enhancements due to local field intensity, as well as the total enhancement, are significantly larger for NIR dyes far from the resonant frequency of an AgNP monomer in comparison to the dyes closer to the resonant frequency (or absorbance maximum). The additional enhancement is likely due to the increase in aggregates formed around the labeled-SAv molecules, which is expected to create 'hot spots' where SEF can be extremely large[46].

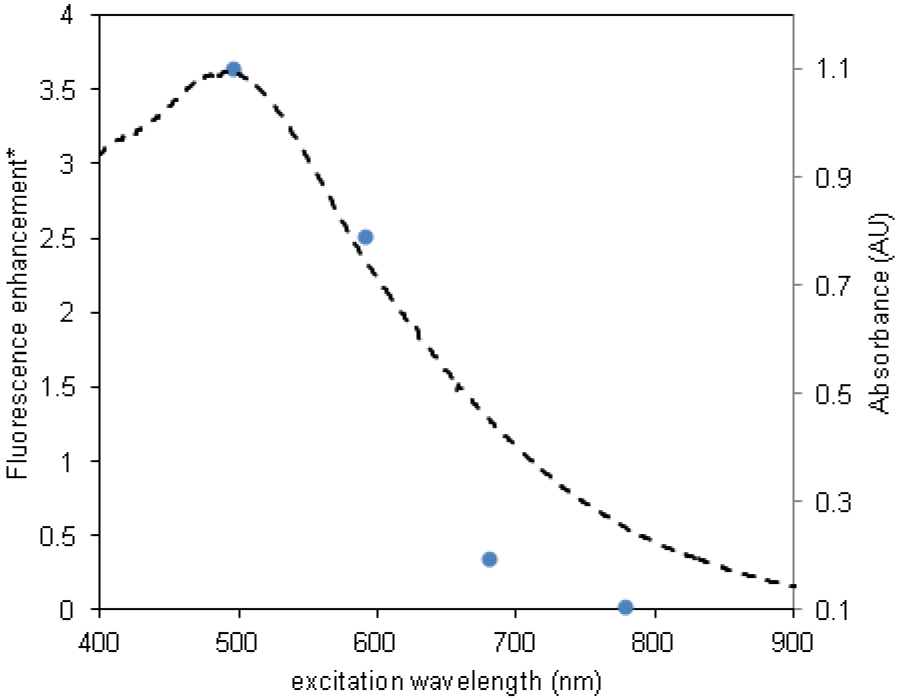

Figure 3.10. Fluorescence enhancement (*corrected for quantum yield) versus excitation wavelength for each fluorophore at a molar ratio of 0.1 AgNP:SAv-fluorophore plotted with the absorbance of AgNP on an arbitrary scale. Error bars (hidden by the markers) indicate +/- one standard deviation at each data point.

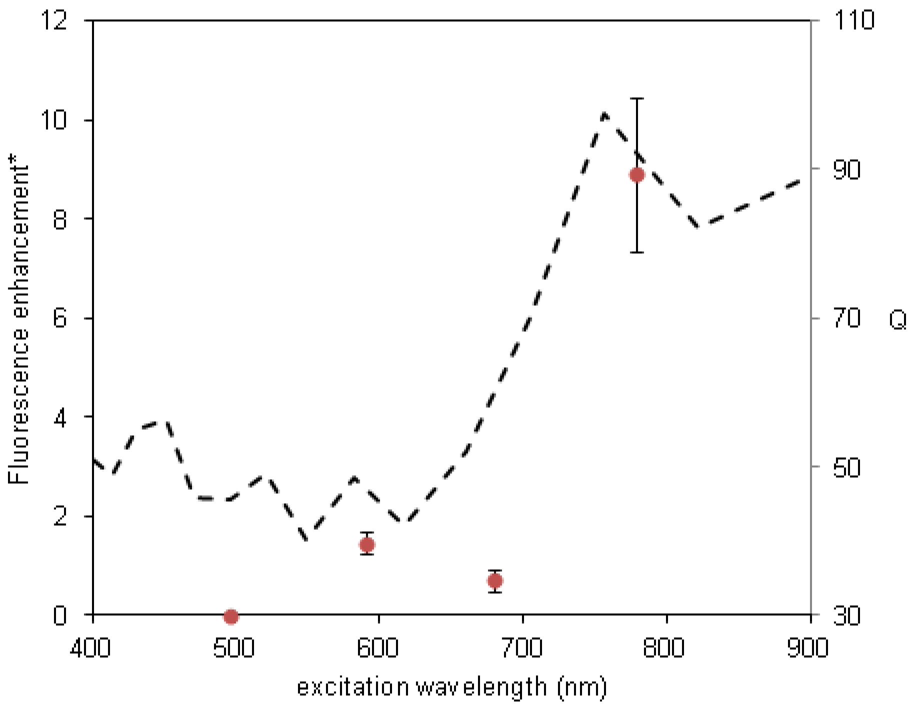

Figure 3.11. Fluorescence enhancement (*corrected for quantum yield) versus excitation wavelength for each fluorophore at a molar ratio of 10 AgNP:SAv-fluorophore plotted with the quality factor of AgNP on an arbitrary scale.. Error bars indicate +/- one standard deviation at each data point.

3.4. CONCLUSIONS

In this chapter, it was demonstrated that the currently accepted theory predicting maximized SEF near the resonant frequency of a plasmon-active nanostructure is dependent on the amount of inner-filtering. Further, it was shown that NIR fluorophores, significantly red-shifted from the resonant frequency of Ag, can experience substantial SEF. The experimental data agreed with the qualitative trends expected from theory; however, the magnitude of enhancement for IRDye 800CW, in particular, was far beyond the predicted value. It is expected (though not tested in this chapter) that the formation of aggregates may be responsible for the increased magnitude of enhancement. The effect of aggregation on the SEF process is studied in Chapters 5 and 6. The findings in this chapter are valuable for multiple reasons. First, it opens the doors for further research involving fluorophores in the NIR range that have not previously been widely expected to demonstrate significant SEF. Second, it suggests that a non-specific interaction between AgNP and labeled-SAv can be easy and powerful without significant inner-filtering if using a NIR dye. Further evidence of interaction between AgNP and SAv is shown in Chapter 4. Third, though not tested directly, the findings suggest that Ag may be a better material choice than Au for NIR-SEF because Ag is expected to have less inner-filtering in combination with a larger quality factor.

CHAPTER 4. A COMPARISON OF CARRIER PROTEINS

4.1. INTRODUCTION

Fluorescence-based assays frequently make use of a fluorophore-conjugated biomolecule as a carrier for detection. These fluorophore-labeled biomolecules enable indirect detection of a target antigen by binding specifically to the target and thus providing a fluorescent signal that is proportional to target concentration. Carrier biomolecules can be in the form of DNA, RNA, oligonucleotides, proteins, or peptides. Proteins are a common carrier of fluorophores in various immunoassays including the prevalent Western blot and fluorophore-linked immunosorbent assay (FLISA). The most commonly used carrier proteins are streptavidin (SAv), immunoglobulin G (IgG), and IgG fragments. SAv is a tetrameric, bacterium protein that can bind up to four biotin molecules. The SAv – biotin interaction forms one of the strongest non-covalent bonds in nature[111]. For this reason, antibodies are often conjugated with biotin and subsequently probed with labeled-SAv as the secondary, or tertiary, detection antibody. IgG is an antibody protein found in the serum of humans and other animals. The whole IgG molecule consists of two identical variable regions and one constant region, all connected by disulfide bonds in the ‘hinge’ regions. The variable regions can differ from molecule to molecule and are responsible for the ability to bind to a specific antigen. The constant region remains identical from molecule to molecule (for a given animal) and is usually used as the target for subsequent antibodies in immunoassays. When used as the final detection antibody it is common for fragments of the IgG molecule to be used without the constant region. The antibody fragments come as either a single fragment antigen-binding (Fab) region or both antigen-binding ($F(ab')_2$) regions connected by disulphide bonds. Figure 4.1 shows the structure of SAv and IgG. The Fab regions are identical and located above the ‘hinge’, while the constant region is below the ‘hinge’. Various enzymes are used to cleave specific portions of the IgG molecule in order to isolate the fragments.

Successful SEF has been demonstrated with labeled SAv and citrate-stabilized AgNP in Chapter 3; however, it remains unclear whether SAv is the best choice for carrier protein. Further, to enable future implementations of SEF in a multiplexing format, SAv cannot be used solely, as a different detection antibody must be used to locate a second antigen. It is hypothesized that the physical size and shape of these carrier proteins may be able to influence the ability to enhance the fluorescent signal from the fluorophores they carry. This hypothesis is tested in three parts. First, it is hypothesized that the size of the carrier protein is important because it determines the average distance of the fluorophores to the nanoparticles. Second, it is hypothesized that the size and shape of the carrier protein determines the number of nanoparticles that can be bound simultaneously per protein, as well as distance between the nanoparticles. Third, it is hypothesized that the shape of the carrier protein determines the number of possible orientations between nanoparticles and the likelihood of the fluorophores to be in the optimal position for plasmon enhancement. To test these hypotheses, SAv, IgG, and $F(ab')_2$ proteins were experimentally and theoretically compared for performance in surface-enhanced fluorescence using IRDye 800CW as the fluorophore and citrate-stabilized AgNP as the plasmon-active substrate.

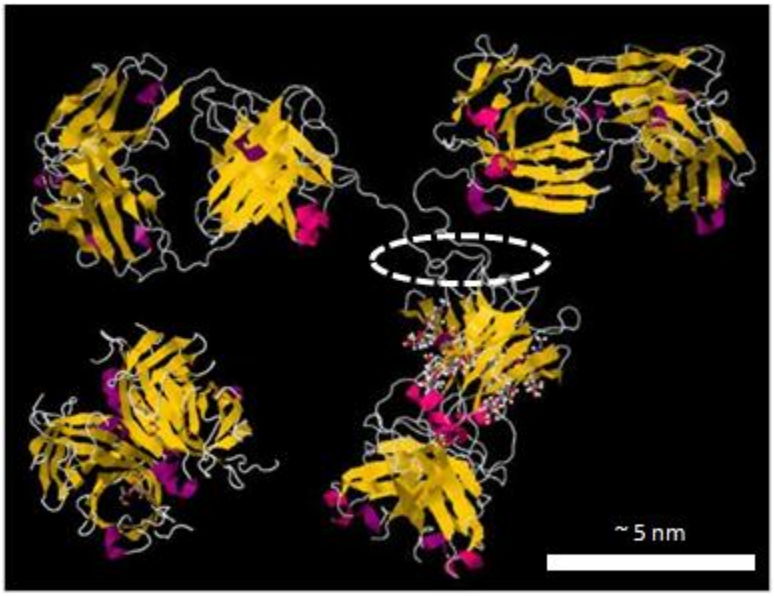

Figure 4.1. 3D models showing the size and structure of SAv (5 x 4.5 x 4.5 nm), lower left[112], and IgG (16 x 15 x 5 nm), right[113]. F(ab')$_2$ is equivalent to IgG without the constant region below the 'hinge' (circled).

4.2. MATERIALS AND METHODS

Materials. SAv and IgG (goat anti-rabbit) were acquired pre-labeled with IRDye 800CW (LI-COR, Lincoln, NE). F(ab')$_2$ (purified non-immunized donkey) was purchased unconjugated (Jackson ImmunoResearch Laboratories, West Grove, PA) and subsequently labeled with IRDye 800CW – NHS ester (LI-COR, Lincoln, NE) using a common labeling technique[114]. AgNP were acquired at a stock concentration of ~ 20 nM with an average diameter of ~ 20 nm (LI-COR, Lincoln, NE). All dilutions were performed with ultrapure water from a Milli-Q system (Millipore). All reagents were used as received and handled per the manufacturer's instructions, unless otherwise noted.

Absorbance measurements. Absorbance measurements were conducted in a 96-well plate using a Synergy 4 Hybrid Microplate Reader (BioTek Instruments Inc., Winooski, VT). SAv, F(ab')$_2$, and IgG at various concentrations were mixed with 0.1X AgNP (~ 2nM) by adding 50 μl of protein diluted in ultrapure water to 50 μl of AgNP and then incubating for 1 hour at room temperature.

Fluorescence measurements. Fluorescence measurements were conducted in 384-well plates using an Odyssey Sa Infrared Imaging System (LI-COR Biosciences, Lincoln, NE).

Boundary element method simulations. Electromagnetic field enhancement was calculated using a freely distributed MATLAB toolbox incorporating the boundary element method (BEM)[115]. A custom program was developed to calculate the electric field modulus between a pair of AgNP under the quasi-static approximation (Appendix A).

4.3. RESULTS AND DISCUSSION

Protein-nanoparticle geometry considerations. As stated before, it is expected that the physical size and geometry of SAv, F(ab')$_2$, and IgG has considerable impact on their ability to create enhanced electromagnetic fields when aggregating with citrate-stabilized

AgNP. Figure 4.2 illustrates this point by presenting examples of possible binding arrangements between the protein and AgNP. The simplest interaction occurs between SAv and AgNP. With an approximately cube-like structure of 5 nm sides (see Figure 4.1), SAv can only bind a maximum of two 20 nm AgNP simultaneously due to geometric limitation (i.e. SAv is too small to contact three 20 nm AgNP simultaneously when they are packed as closely as possible). Figure 4.2(a) shows that a third AgNP cannot make contact with the SAv when two AgNPs are already in contact. When contacting two AgNP simultaneously, the SAv molecule always creates a gap of approximately 5 nm. The antibody fragment, F(ab')$_2$, consists of two identical structures that can be approximated as square prisms with 5 nm sides and a length of 7 nm (see Figure 4.1). The two structures are connected by a disulfide 'hinge region' which creates a gap on the order of 1 nm. Figure 4.2(b) shows that F(ab')$_2$ can contact a total of four AgNP simultaneously. In this case, the distance between any two AgNP can vary between 5 nm and 15 nm. It should be noted that when the distance is minimized (see Figure 4.2(b) dotted lines) there is only a small probability that the attached fluorophore(s) are located directly between the AgNP. On the other hand, the probability that the fluorophore(s) are located directly between the AgNP is maximized when the distance is also maximized. It is expected that this relationship is not ideal for fluorescence enhancement. The whole antibody, IgG, consists of three nearly identical structures that can be approximated again as square prisms with 5 nm sides and a length of 7 nm each. The three structures are held together by 'hinge regions' that consist of disulfide bonds creating gaps of approximately 1 nm. Figure 4.2(c) shows that IgG can bind up to three coplanar AgNP at a time. It is expected that two more AgNP could simultaneously be bound, including one in front of and one behind the structure in the diagram, giving a total of up to 5 AgNP at once. There are two likely orientations for the coplanar capacity, shown as the solid particles and dotted lines respectively. The dotted lines are expected to occur less frequently as the protein would likely make contact with the AgNP prior to allowing it to wedge itself between multiple regions. In this case, the distance between AgNP can vary between 5 nm and 15 nm. In contrast to F(ab')$_2$, the fluorophore(s) on IgG are likely to be directly between two AgNP when the distance is minimized. This orientation would require the AgNP to be positioned as shown by the dotted lines in Figure 4.2(c), which is improbable due to unfavorable entropy. It should be noted that it is possible that IgG could bind more than three coplanar AgNP simultaneously if the hinges are positioned correctly and the AgNP assemble in an appropriate orientation. Nonetheless, these diagrams are intended to compare the binding capacities and probable orientations of the AgNP in relation to the protein and ultimately the location of the fluorophore(s) relative to the AgNP. A comparison of these diagrams suggests that SAv is most probable to position the fluorophore(s) directly between AgNP with a minimal gap.

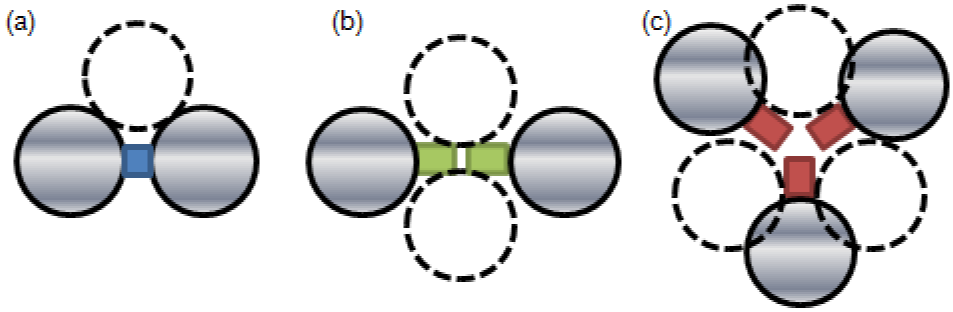

Figure 4.2. Diagram showing possible interaction orientations for 20 nm AgNP with (a) SAv, (b) F(ab')$_2$, and (c) IgG. The colored blocks represent the proteins and are drawn to scale relative to the 20 nm AgNP. The gaps between blocks for (b) F(ab')$_2$ and (c) IgG represent the 'hinge regions'.

Absorbance measurements were made at various ratios of protein to AgNP to experimentally investigate the relative number of AgNPs that each protein can simultaneously bind. Aggregation of the AgNPs induced by protein interaction can be detected as a distinct change in the absorbance spectrum in comparison to AgNPs in the absence of protein. Specifically, the plasmon resonance peak is reduced and the spectrum becomes relatively flat. The absorbance of each protein at the various ratios to AgNPs can be seen in Figure 4.3. The amount of protein required to aggregate the AgNP, and thus change the absorbance spectrum, is indicative of the number of AgNP each protein can bind simultaneously. Specifically, the protein that distorts the plasmon resonance of the AgNP monomers at the lowest concentration likely binds the largest number of AgNP per protein. Likewise, the protein requiring the highest concentration to distort the plasmon resonance of the AgNP monomers likely binds the least number of AgNP per protein. SAv causes sufficient aggregation to significantly impact the spectrum at a ratio of 5 molecules per AgNP and completely flattens it at 10 molecules per AgNP. F(ab')$_2$ completely flattens the spectrum at a ratio of 5 molecules per AgNP, suggesting that the binding capacity of F(ab')$_2$ is larger than that of SAv. IgG almost flattens the curve at just 2 molecules per AgNP, suggesting that its binding capacity is even larger yet. This experiment is not intended to quantitatively compare the binding capacities; however, it does provide qualitative data in agreement with the binding capacity predictions based on the geometry of each biomolecule and AgNP.

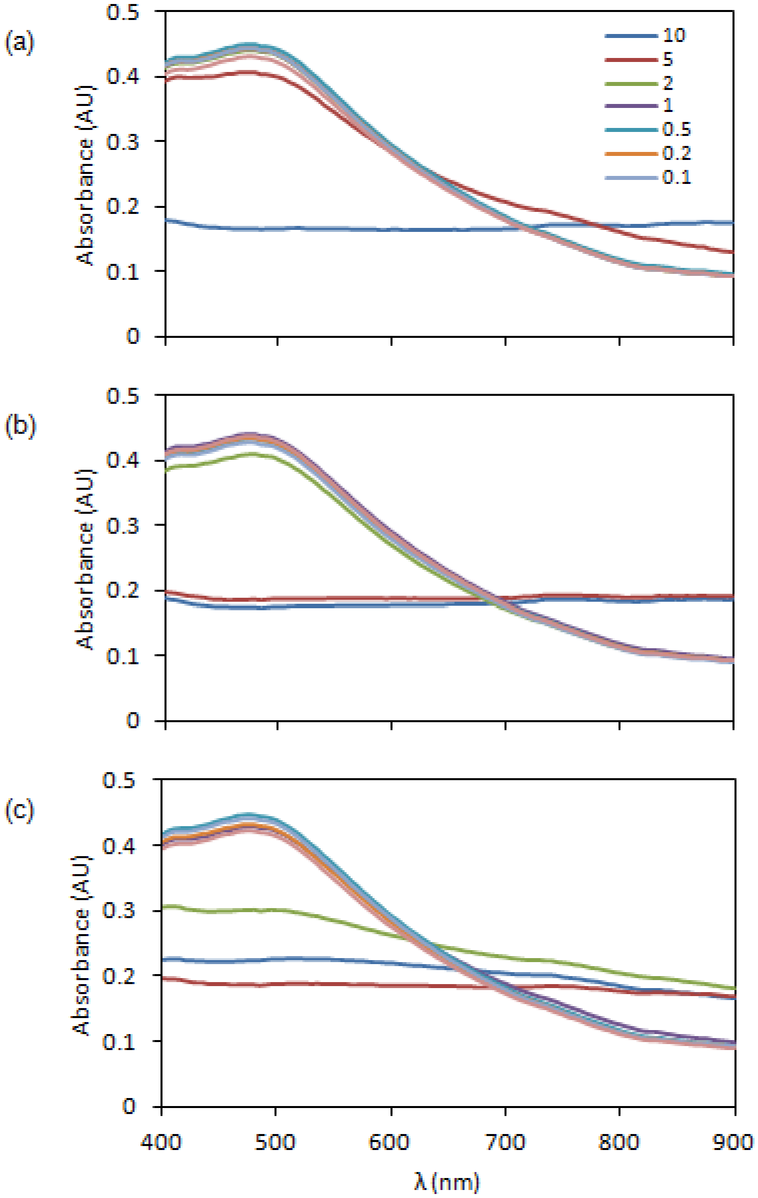

Figure 4.3. Absorbance measurements of (a) SAv, (b) F(ab')$_2$, and (c) IgG mixed with AgNP at various molar ratios (protein:AgNP). The AgNP concentration was held constant at ~ 2 nM, while the protein concentrations varied. Aggregation causes the resonant peak to decrease and the spectra to become flat.

Simulated electromagnetic field intensity. As stated before, it is expected that the fluorescence enhancement using the various biomolecules may also differ due to the physical distance between multiple AgNP bound by the proteins. To study this effect, BEM simulations were conducted on a pair of AgNP at separation distances of 5, 10, and 15 nm (see Figure 4.4). The calculations were made under the quasi-static approximation, which assumes the conduction band electrons move as an incompressible fluid, or cloud, and thus limits the induced oscillations to dipoles. This assumption is known to be valid when the AgNP diameter is significantly smaller than the wavelength of excitation light[116]. The results provide both quantitative and qualitative insight into the distance effect. As the AgNP pair is brought closer together the electromagnetic field is further confined creating larger field intensity. Figure 4.4 shows the simulated electric field modulus ($|E|^2$) on identical logarithmic color map for each distance. At 15 nm, the AgNP dimer have little influence on one another and the field between only reaches 2- or 3-fold enhancement over the far-field intensity. At 10 nm, the particles begin to show a synergistic effect where the individual dipole fields are not only excited by the far-field but also one another. Further, they become able to confine the energy into a smaller volume than individually possible. This enables the intensity to achieve an order of magnitude enhancement. Further enhancement occurs at 5 nm where the energy is confined to an even smaller volume. It is theoretically possible to achieve greater field enhancement by using a smaller carrier protein, and/or, using slightly larger AgNP. This may prove difficult experimentally, however, for two reasons. SAv is the smallest, commonly used carrier protein in bioassays. A smaller protein may not bind multiple AgNP as easily or may be difficult to achieve a useful degree of labeling (fluorophores per protein). Also, larger AgNP diffuse more slowly and do not aggregate as quickly.

Further, the molar concentration decreases as one increases the size of AgNP for a given amount of silver, which further slows the aggregation process.

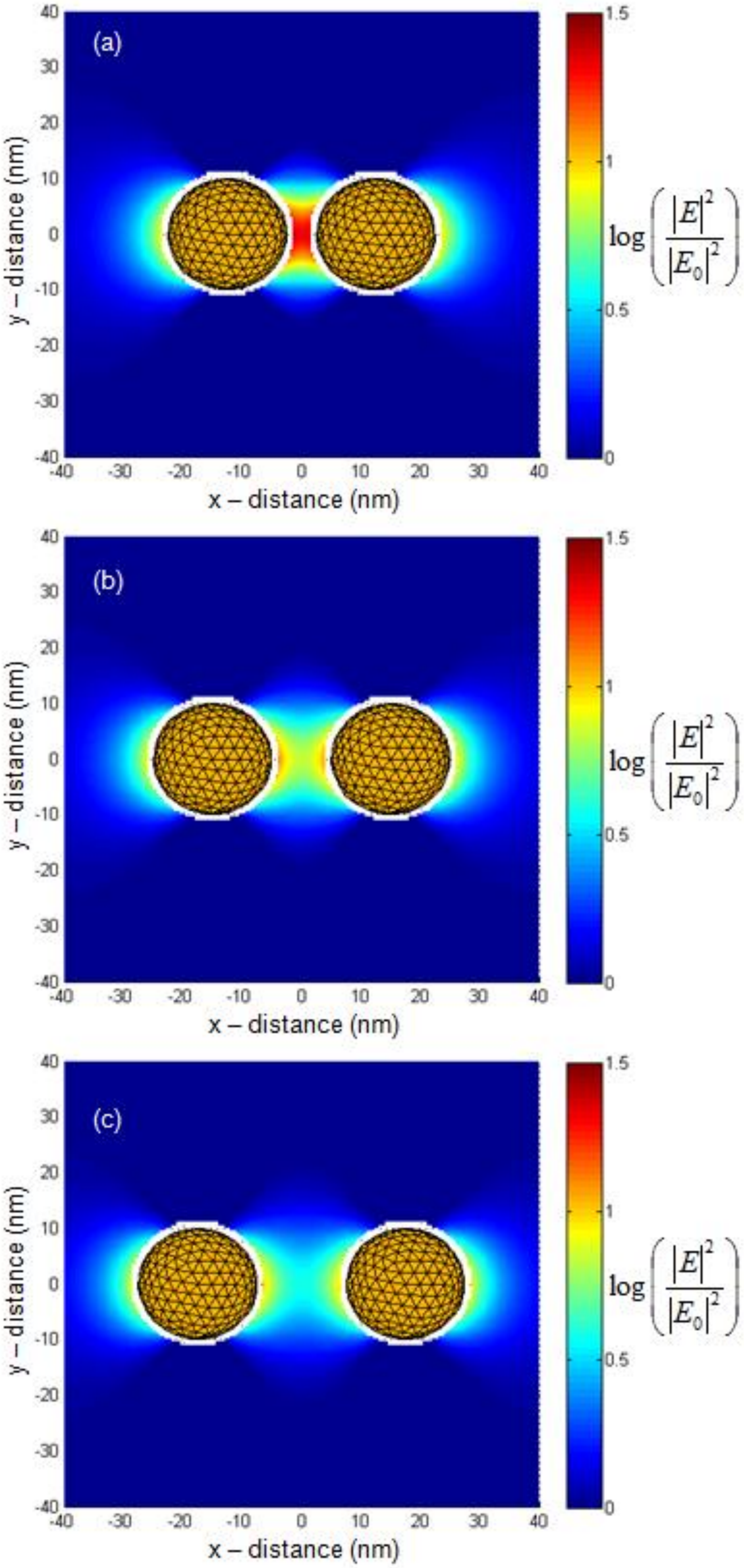
(a)
(b)
(c)
y – distance (nm)
x – distance (nm)
40
30
20
10
0
-10
-20
-30
-40
1.5
1
0.5
0
$\log\left(\frac{|E|^2}{|E_0|^2}\right)$

Figure 4.4. Simulated, relative electromagnetic field intensity around a pair of 20 nm diameter AgNP with separation distances of (a) 5 nm, (b) 10 nm, and (c) 15 nm. The simulations were conducted with light propagation perpendicular to the particle pair axis (y-direction) at a frequency representative of 785 nm wavelength excitation. The polarization is set so that the electric field is parallel with the particle pair axis (x-direction).

Fluorescence enhancement. Experiments were conducted with labeled SAv, $F(ab')_2$, and whole IgG to determine the ability of each biomolecule to enable fluorescence enhancement when combined with the AgNP solution. Figure 4.5 shows the fluorescence enhancement at various molar ratios of protein to AgNP.

$$Fluorescence\ enhancement = \frac{I_{dye+AgNP} - I_{AgNP}}{I_{dye} - I_{blank}}$$

As expected, SAv demonstrates the largest enhancement of 1000-fold at a ratio of 1 molecule to 2 AgNP. At lower protein concentrations, however, it only achieves 100-fold enhancement. This may be due to the more concentrated solutions of protein being able to create higher-order aggregates that further enhance the electromagnetic field intensity, while the lower concentrations are expected to form primarily dimers. Two data points at the highest SAv:AgNP ratios were omitted due to detector saturation. $F(ab')_2$ demonstrates the lowest levels of enhancement, ~20-fold. The enhancement for $F(ab')_2$ appears relatively independent of protein:AgNP ratio which suggests the distance between the AgNPs as the limiting factor, rather than protein-AgNP interaction. IgG achieves an enhancement of ~60-fold at all ratios of protein:AgNP. Again, protein-AgNP interaction is probably not limiting in this case. As expected, all three carrier proteins show a trend of reduced fluorescence enhancement at the highest protein:AgNP ratios.

This is likely due to an increase in monomers coated with protein which are subject to substantially smaller electric field intensities in comparison to dimers and higher-order aggregates. The standard deviations of each data point are relatively small for all three proteins, but clearly smallest for SAv. This may be due to the consistent position of SAv, and thus the fluorophores, in relation to the AgNP as discussed previously.

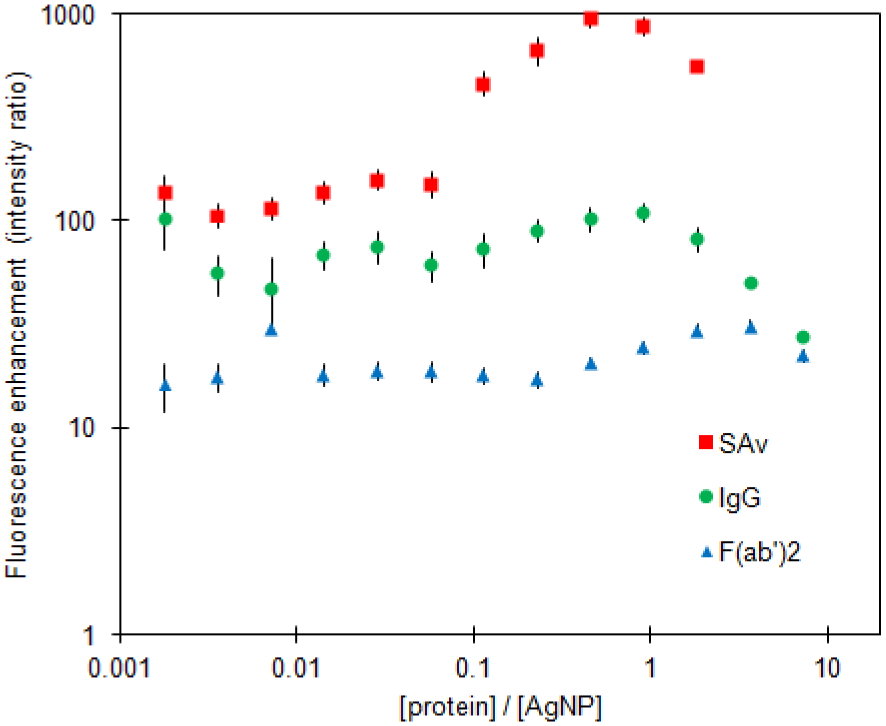

Figure 4.5. Fluorescence enhancement of dye-labeled SAv, F(ab')$_2$, and IgG at various molar ratios of protein to AgNP. Error bars display +/- 1 standard deviation at each data point.

Assay potential. While enhancement of the fluorescent signal is desirable, real-world applications desire a technology that is also linear in respect to signal versus concentration and ultimately achieves greater LOD than available with traditional approaches. To determine the assay potential of each carrier protein, a 2-fold dilution series, 131 nM down to 62.5 fM, was incubated with and without AgNP in a 384-well plate. The data were then plotted to check linearity as well as empirical LOD. SAv-800CW alone is linear from ~64 pM on up to an undetermined limit with an empirical LOD of 16 pM (see Figure 4.6). The addition of AgNP improves the LOD 4-fold to 4 pM. The data remain relatively linear until instrument saturation occurs at concentrations above 8 nM.

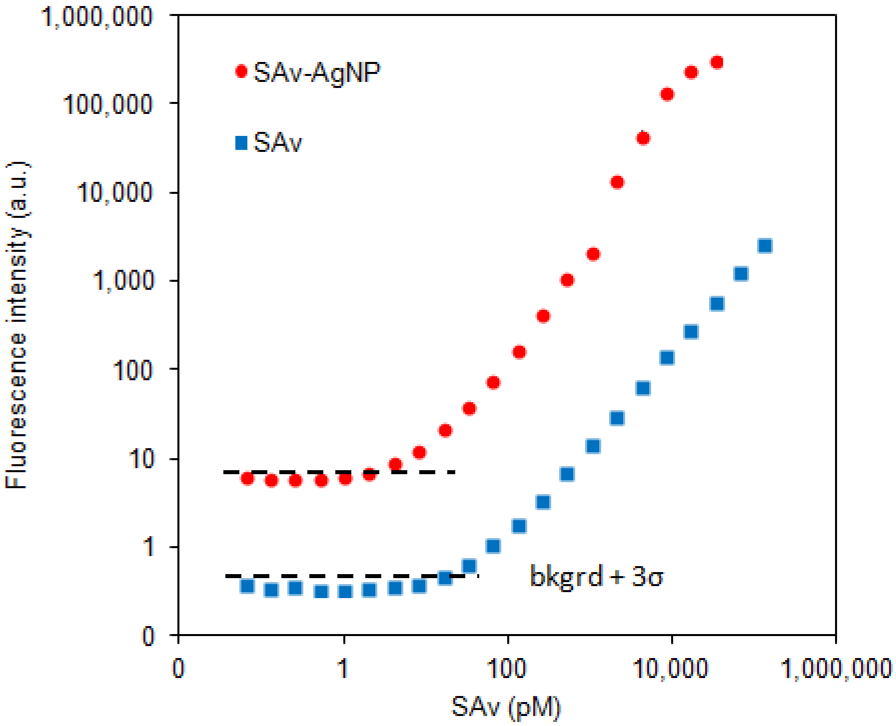

Figure 4.6. Fluorescence intensity versus SAv-800CW concentration with and without AgNP. Error bars at +/- 1 standard deviation at each data point are included, though they are smaller than the data markers and therefore hidden.

F(ab')$_2$-800CW alone is linear from ~64 pM on up with an empirical LOD of 32 pM (see Figure 4.7). The addition of AgNP improves the LOD 2-fold to 16 pM. The data remain linear until instrument saturation occurs at concentrations above 65.5 nM.

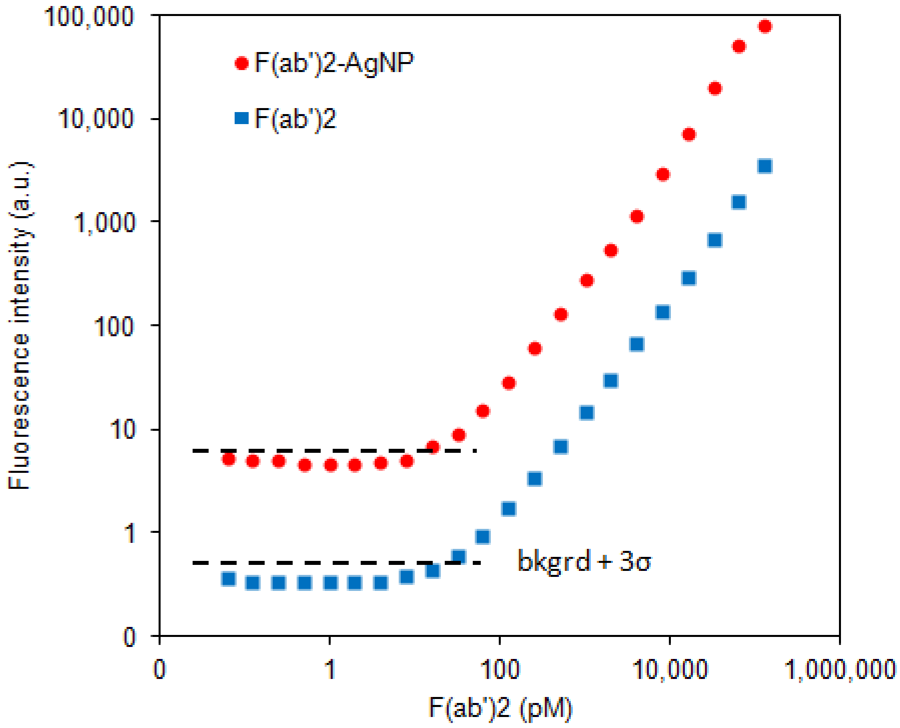

Figure 4.7. Fluorescence intensity versus F(ab')$_2$-800CW concentration with and without AgNP. Error bars at +/- 1 standard deviation at each data point are included, though they are smaller than the data markers and therefore hidden.

IgG-800CW alone is linear from ~64 pM on up with an empirical LOD of 32 pM (see Figure 4.8). The addition of AgNP improves the LOD 4-fold to 8 pM. The data remain linear until instrument saturation occurs at concentrations above 16.4 nM.

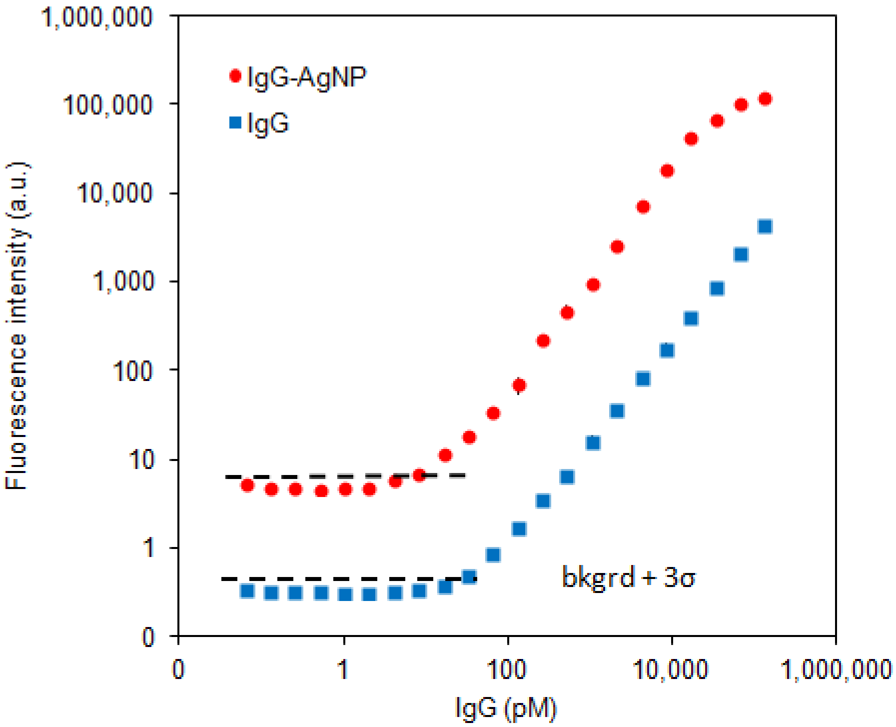

Figure 4.8. Fluorescence intensity versus IgG-800CW concentration with and without AgNP. Error bars at +/- 1 standard deviation at each data point are included, though they are smaller than the data markers and therefore hidden.

4.4. CONCLUSIONS

In this chapter, it was hypothesized that the physical size and shape of carrier proteins play an important role in the ability to enhance the fluorescent signal from the fluorophores they carry when combined with AgNP in solution. The effect of protein size on distance between bound AgNP and thus electromagnetic field intensity was studied using BEM simulations. The effect of protein size on the number of bound AgNP was experimentally studied by measuring aggregation at various protein/AgNP ratios by changes in absorbance. The effect of protein shape on possible AgNP-fluorophore orientations was qualitatively discussed based on geometric limitations. To study these effects in combination, experiments were conducted to measure fluorescence enhancement with dye-labeled SAv, F(ab’)$_2$, and IgG. Each protein demonstrated the ability to enhance fluorescence, maintain a linear relationship with signal versus concentration, and ultimately improve the LOD. SAv was determined to be the best choice for carrier protein due to its unmatched ability to generate 1000-fold enhancement with the smallest standard deviations.

CHAPTER 5. SURFACE-ENHANCED FLUORESCENCE VIA COLLOID AGGREGATION IN A DROPLET-BASED MICROFLUIDIC DEVICE

This chapter is based on previously published work by the author[117]*. Copyright Springer and Plasmonics, 4, 2009, 273-280, Near-infrared metal-enhanced fluorescence using a liquid-liquid droplet micromixer in a disposable poly(methyl methacrylate) microchip, Furtaw, M.D., Lin, D., Wu, L., and Anderson, J.P. Reprinted with kind permission from Springer Science and Business Media.*

5.1. INTRODUCTION

Fluorescence spectroscopy is a sensitive and relatively simple method of detection used in biotechnology research for decades. Recent trends in research however, have demanded the ability to push the limit of detection (LOD) beyond traditional capabilities for increased sensitivity of fluorescence based assays. Improvements in the LOD can be achieved by reduced sample volumes, lower background signals, and increased absorption cross-section, photostability, and quantum efficiency of fluorophores. Microfluidics, near-infrared (NIR) fluorescence, and surface enhanced fluorescence

(SEF) are emerging technologies that can improve the LOD but have not been studied in combination.

Microfluidic systems are becoming increasingly popular in biotechnology research and offer many advantages over the traditional macroscale approaches. Small reagent volumes, shorter reaction times, parallel operation, and the ability to precisely control and study the interaction of biological samples make microfluidic based assays highly appealing[118-120]. While the benefits of microfluidics are astonishing there are inherent difficulties that must be overcome. One such problem arises when detecting dilute sample concentrations in microfluidic channels, especially in continuous flow devices where the exposure time becomes limited, resulting in reduced signal and poor signal-to-noise. Fluorescence detection with NIR fluorophores in combination with SEF may provide a solution for the exposure time limitations of continuous flow microdevices. NIR fluorescence is increasingly being used in biological imaging and molecular applications because it provides significantly lower background signal from scatter than visible wavelength excitation[121, 122]. NIR fluorescence has also been demonstrated to be advantageous in microfluidic applications due to the significant reduction in autofluorescence of common plastics used in microchip fabrication[30, 123-126]. While NIR fluorophores greatly increase signal-to-noise they can be difficult to detect with traditional fluorescence microscopy as the longer wavelengths lead to reduced excitation intensities from common Hg lamps and significantly lower quantum efficiency of most CCD cameras. SEF has emerged as a promising technology that can greatly increase the quantum yield of fluorophores, which can overcome the limited exposure times of continuous flow microfluidic devices and the lower efficiencies of NIR fluorescence microscopy. SEF has been used to provide enhancement of fluorophores in the visible spectrum as well as the NIR. Background signal from silver nanostructures in the visible spectrum, however, may adversely affect the overall signal-to-noise ratio of the system. Surface enhancement in the NIR provides the benefits of enhanced emissions with low background signal[97].

SEF can improve the quantum yield and photostability of a fluorophore when it is located in close proximity to a metal surface. Unlike fluorescence excitation in free space, an excited fluorophore near a metal surface can utilize an additional pathway to return to the ground state by inducing surface plasmons (SPs)[1, 71, 127]. This additional radiative decay mechanism reduces the life-time of the fluorophore and thus improves the photostability[128-130]. The induced SPs propagate along the metal surfaces and either emit photons at the same wavelength as the fluorophore or dissipate as thermal energy, depending on the ability for momentum, or wave vector matching at the metal-dielectric interface[61]. Additionally, local electric fields around the metal surface can act as an antenna to increase the apparent absorption cross-section of the fluorophore[62]. The increased excitation, reduced life-time, and additional emitted photons can lead to substantial improvements in quantum yield and photostability. There are excellent reviews that discuss these mechanisms in greater detail[57, 61, 62, 69].

Research on SEF has focused mainly on flat metallic surfaces or glass slides coated with Al, Au or Ag nanostructures[88, 97, 131-134], the latter known as silver island films (SIFs). Solution-based SEF has received little attention in the literature even though it is highly desirable for solution based assays and medical imaging[69]. The lack of publications involving SEF in solution may be due to the difficulty in controlling aggregation and the position of fluorophores in relation to metal nanoparticles in suspension[135-139]. Microfluidic technologies may overcome these difficulties but have not yet been used to study solution-based SEF, even though it has been used to study the related mechanisms involved in surface enhanced Raman scattering[140-144]. The control of microfluidics in combination with the low background signal of NIR fluorescence provides an ideal system for the study of solution-based SEF.

Here, we report on the use of a liquid-liquid droplet micromixer in a disposable poly(methyl methacrylate) (PMMA) microchip to study the effects of salt concentration, colloid concentration, and mixing efficiency on SEF of NIR fluorophores with aggregated Ag nanoparticles using conventional fluorescence microscopy. Microfluidics provides the advantages of less sample volume, easy manipulation of solution parameters, and controlled mixing and aggregation of the nanoparticles. Furthermore, the use of a water-in-oil droplet micromixer overcomes the “memory” effect of particles sticking to the channel walls and eliminates Taylor dispersion[144, 145], while maintaining discrete packets of known contents without cross contamination. Plastic microchips are desirable for their low-cost, ease of fabrication, and optical clarity, especially in the NIR wavelengths[125]. PMMA has the additional benefit of neutral hydrophobicity (i.e. contact angle of approximately 90°), which minimizes interaction with proteins and other biological samples[124], relative to more hydrophobic polymer materials commonly used as microchip substrates. The NIR dyes not only provide lower background signals, but also demonstrate significant enhancement from SEF when combined with Ag nanostructures[88, 97]. Aggregated silver nanoparticles (AgNP) prove useful in solution-based SEF for their optical properties[61] and compatibility with biological samples[69].

5.2. MATERIALS AND METHODS

The experimental apparatus and microchip geometry are shown in Figure 5.1. Syringe pumps (New Era Pump Systems Inc., Farmingdale, NY) provide flow through each inlet channel. The colloid and dye solutions consistently form droplets bound by oil with volumes that can be manipulated and reproducibly controlled by changing the flow rates of the aqueous and oil solutions in relation to one another, see Figure 5.2. For the purposes of this study the droplet volumes were held constant at an arbitrary volume of approximately 35 nL. Detailed descriptions of water-in-oil droplet formation, mixing in serpentine channels, and AgNP preparation can be found in the literature[100, 145-148]. The AgNP are characterized by dynamic light scattering measurements using a Brookhaven 90Plus particle sizer (Brookhaven Instruments Corporation, Holtsville, NY), which indicate a normal distribution of nanoparticle size with a mean, intensity-weighted diameter of 76 nm and number-weighted mean of 21 nm. The particle density can be calculated using the average diameter and known amount of Ag in the solution. IRDye 800CW-streptavidin dye (LI-COR Biosciences, Lincoln, NE) is diluted to 1 μg mL^{-1} in each required phosphate buffered saline (PBS) solution. PBS is used as the aggregation enabling salt for its commonality and compatibility with biomolecules. Deionized water is used for all dilutions. Typical cooking oil is used to form droplets in the microchannel as it is readily available and immiscible to the aqueous solutions. All solutions are used as received without further filtering.

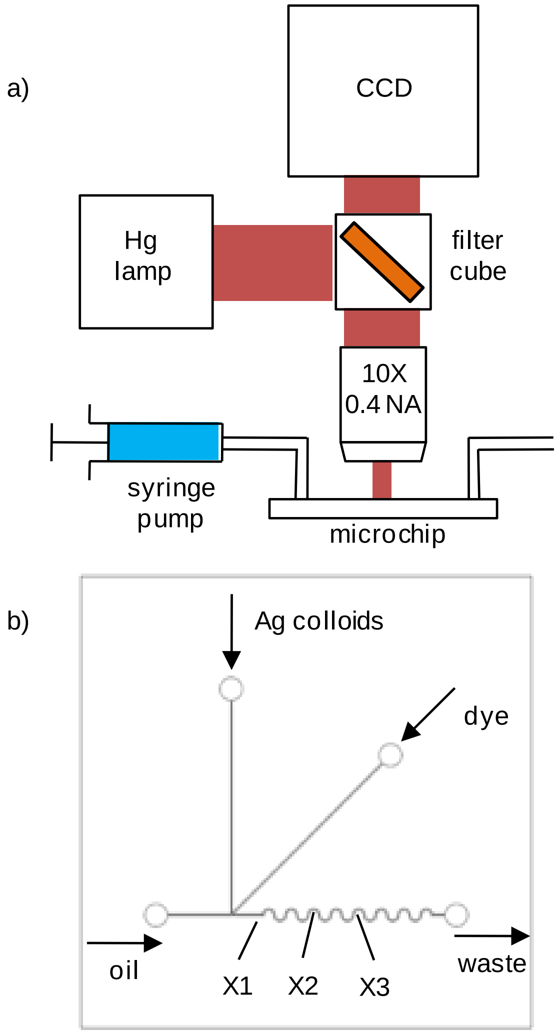

Figure 5.1. Diagrams showing (a) the experimental apparatus and (b) microchip geometry with image acquisition point designated by X1, X2, and X3. A CCD camera acquired images through a fluorescence microscope with a 10X objective lens using Hg arc lamp excitation. A filter cube set appropriate for IRDye 800CW was used with excitation, dichroic, and emission peaks at 740, 770, and 780 nm respectively. The PMMA microchip was fabricated using a hot-embossing technique and bonded with a thin layer of adhesive. Channel dimensions are approximately 200 μm across and 200 μm in depth. Syringe pumps provide flow rates of 1 μL min^{-1} for the colloid and dye solutions and 3 μL min^{-1} for the oil which consistently form droplets of approximately 35 nL that travel through the microchannel at a velocity of 2 mm s^{-1}.

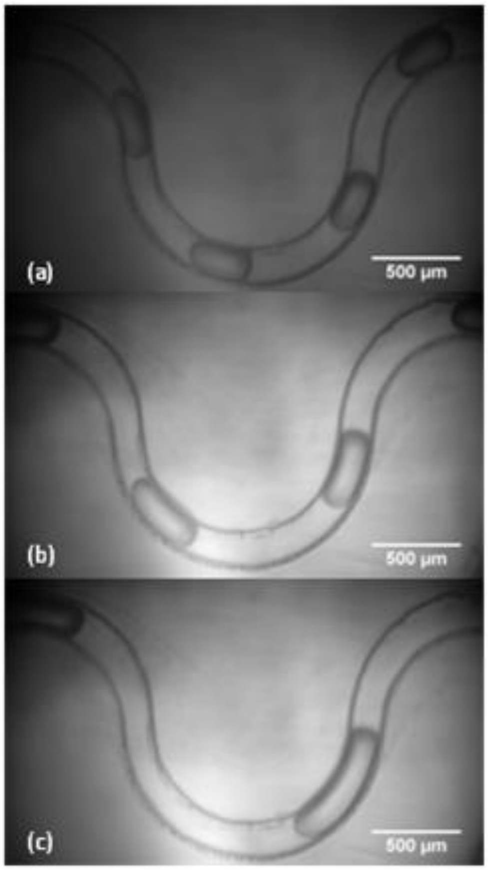

Figure 5.2. The liquid-liquid droplet micromixer allows easy manipulation and control of various parameters including the droplet volume. Droplets of (a) small, (b) medium, and (c) large volume are shown as an example of the capabilities of the device. Other parameters that can be easily manipulated include the relative flow rates of each reagent as well as the mean velocity of the combined solutions and thus the reaction rate. Images were taken with a 10X objective lens under brightfield excitation without post-processing other than simple cropping and adding scale bars.

Chip fabrication. The liquid-liquid droplet micromixers are fabricated using a hot-embossing technique in PMMA. PMMA is purchased as 2 mm thick sheets. A steel dye was milled to leave the necessary geometry for embossing. Mold release agent is sprayed on all surfaces prior to the embossing process to allow easy separation. A heated plate press (Specac Ltd., United Kingdom) is operated at 90°C to heat the PMMA chip near its glass transition temperature. A force load of 3.5 tons is slowly applied to displace the desired material forming the microchannel geometry. The device is slowly brought back to room temperature before removing the embossed microchip so as not to allow internal stresses to form cracks around the delicate features. The microchip is then cleaned with methanol and deionized water before being placed on a hot-plate to rid the surfaces of moisture.

The mating chip is cleaned and then coated with a thin layer of UV-curable adhesive (Summers Optical, Hatfield, PA) using a spin-coater (Laurell Technologies Corp., North Wales, PA). The prepared chips are again stacked in the heated plate press at 80°C and a force load of 1.2 tons for approximately 15 minutes. We find this step to be convenient for the removal of air bubbles between the chip surfaces. Finally, the chip is placed under a UV-lamp for at least an hour to fully cure the adhesive. PMMA does not transmit light in the deep UV (< 300 nm) but allows sufficient light in the 350-400 nm range to enable curing of the adhesive.

Data acquisition. The microchip is placed, with all required tubing attached, under a fluorescence microscope (Olympus America Inc., Center Valley, PA) with a 10X objective lens and mercury arc-lamp excitation. A filter cube (Chroma Technology Corp., Bellows Falls, VT) designed specifically for IRDye 800CW is used with excitation, dichroic, and emission peaks at 740, 770, and 780 nm respectively. Images are acquired in TIFF format with a 16-bit, monochrome CCD camera (Hamamatsu Photonics K. K., Japan) which is controlled by the manufacturer supplied software. Fluorescence microscopy with NIR fluorophores and broadband excitation typically require exposure times on the order of seconds. SEF in our system enabled the exposure time to be reduced to 50 ms providing quality images of the moving droplets with negligible smearing.

Image analysis. All image analysis is completed using Image J software (U. S. National Institutes of Health, Bethesda, MD). Background subtraction for each data set used droplets at various positions along the microchannel that contained colloids with no fluorophore present. Individual droplets are analyzed using the ‘Particle Analysis’ feature included with the software. When used for visual comparison, images are processed with equal adjustments to the brightness, contrast, and applied false color. All fluorescence enhancement data is based on the baseline intensity acquired from the dye solution mixed with deionized water in the absence of AgNP after background subtraction.

5.3. RESULTS AND DISCUSSION

The effect of salt concentration on fluorescence enhancement demonstrates an interesting trend of modest signal increases at both dilute and highly concentrated solutions with a significant but narrow peak in fluorescence intensity (see Figure 5.3). Mixing the IRDye 800CW-SAv diluted in deionized water only with the AgNP gives a modest 2 to 3-fold enhancement. This can be attributed to the lack of aggregation due to the electrostatic repulsion between individual nanoparticles in the absence of salt. The aggregation process, and thus SEF, increase significantly with low concentrations of salt. The increased extinction of aggregated AgNP is known to be dominated by scattering in the

NIR, which allows SPs to radiate into the far-field, rather than dissipate as heat[61]. Our preliminary results suggest an optimal concentration for our system around 0.1X PBS which provides a 35-fold fluorescence enhancement when mixed with the AgNP. Further addition of salt beyond the point of neutralizing the electrostatic charge proves detrimental to the fluorescence signal enhancement. Zhang et al. attribute this to a migration of loosely attached Ag atoms upon bonding with Cl^- ions, which later reattach to form a thin layer of non-crystalline Ag of high light absorptivity and low conductivity[149]. In their work, electron micrographs show geometrical changes in the aggregated AgNP, which cause smoothing in the transitional areas between neighboring nanoparticle surfaces. The presence of a thin layer of non-crystalline Ag is consistent with reduced fluorescence enhancement as the layer of low conductivity would inhibit SP propagation, the smoothing between nanoparticles would reduce the electromagnetic field amplification for enhanced excitation, and the light absorption property would tend to reduce scattering and quench the fluorophores rather than improve their quantum yield.

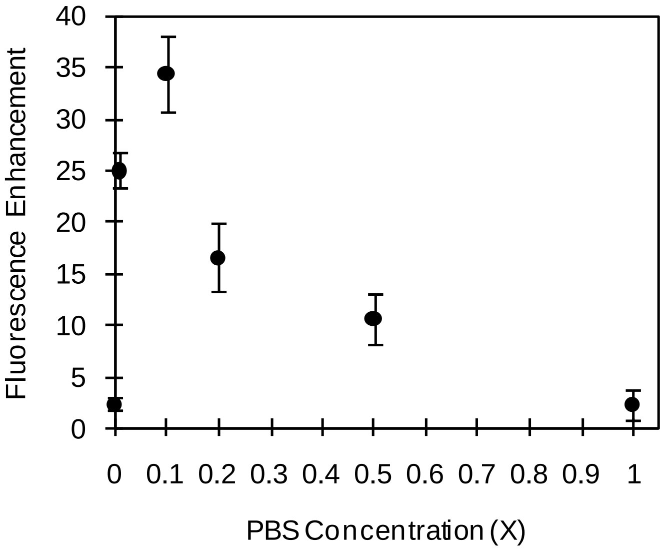

Figure 5.3. Mean fluorescence enhancement of droplets containing IRDye 800CW-SAv (1 µg mL^{-1}) in various concentrations of PBS mixed with AgNP at a density of ~ $1x10^7$ particles nL^{-1}. Data were obtained at position X3 (Figure 1b) using 25 images acquired at a frequency of 1 Hz for each salt concentration. Error bars show the standard deviation of fluorescence enhancement at each salt concentration and demonstrate the consistency of the data. When no salt is added the AgNP remain electrostatically repelled to one another reducing the aggregation process. Low concentrations of salt allow the particles to become neutrally charged enabling the aggregation process to occur at a rapid rate. Higher concentrations of salt react with the AgNP to create a loosely attached, non-conductive layer[149] reducing the development of SPs and thus inhibit SEF.

The effect of colloid concentration on fluorescence enhancement is shown in Figure 5.4. All data points were corrected for background signal at the highest concentrated colloid solution. Lower concentrations demonstrate minimal fluorescence enhancement which can be attributed to the significantly lower probability of AgNP-fluorophore interaction and lack of sufficient colloid aggregation. An increase in colloid concentration enables the formation of larger aggregates which increases the scattering cross-section in the NIR (see Chapter 6). The probability of AgNP-fluorophore interaction beneficial to SEF is also increased with the greater AgNP surface area and density. The linear trend in enhancement of the more concentrated colloid solutions suggests the possibility of further improvement with even denser solutions of colloids. This trend is expected to reach an asymptotic value and perhaps even begin to decrease at higher concentrations of AgNP due to the increase in viscosity and eventual blockage of the excitation light from the fluorophores in the dilute dye solution.

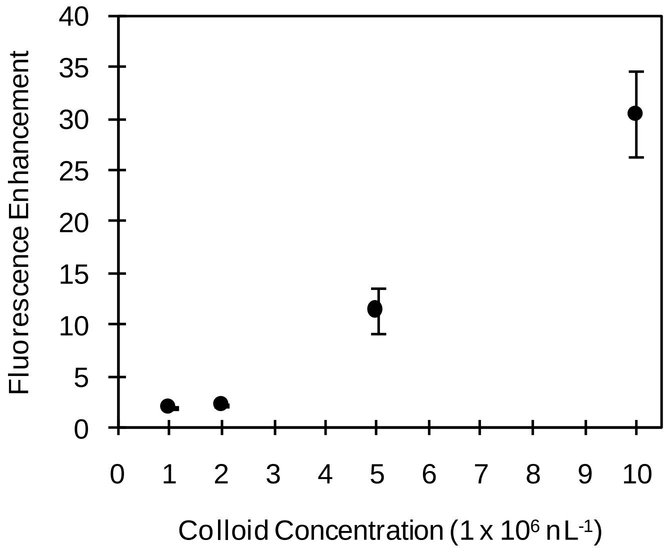

Figure 5.4. Mean fluorescence enhancement of droplets containing IRDye 800CW-SAv (1 µg mL^{-1}) in 0.1X PBS mixed with various dilutions of AgNP. Data were obtained at position X3 (Figure 1(b)) using 25 images acquired at a frequency of 1 Hz for each colloid solution. Error bars show the standard deviation of fluorescence enhancement for each colloid solution and demonstrate the consistency of the data. Low concentrations of AgNP demonstrate only slight fluorescence enhancement due to the lack of aggregation and a reduced probability of interaction between the fluorophores and the AgNP. Higher concentrations of AgNP further the aggregation process and enhance the fluorescence signal in a linear trend increasing with particle density and particle surface area.

The effect of mixing efficiency on fluorescence enhancement is studied by analyzing droplets at different positions within the serpentine microchannel, see Figure 5.5. Flow rates are held constant so that further progression in the micromixer leads to increased mixing time and number of vortex rotations within the droplet, and thus mixing efficiency[147]. Data were acquired at the three positions shown in Figure 5.1(b). The fluorescence enhancement demonstrates a linear increase with distance traveled in the serpentine micromixer. The lack of an asymptotic trend suggests that further enhancement may be possible further down the channel. Physical interference between the outlet port and the microscope objective lens prevented data from being acquired beyond position X3. Vortex rotations within the droplet are caused by the no slip condition at the microchannel wall, much like a rotating wheel on the ground, and thus increase linearly with channel distance. The striation thickness is reduced with each rotation allowing diffusion to increase the mixing efficiency in a logarithmic trend. This is interesting as it suggests that the unexpected linear process of fluorescence enhancement may not have been limited by mixing but rather by some other process, perhaps diffusive in nature, occurring locally around the aggregated structures. The process of aggregation could also be responsible for the unexpected results as the localization of nanoparticles would likely lead to viscosity gradients within the droplet. Future research is required to determine if further, or more intense, mixing changes this trend and to characterize the mixing process involved with aggregation of nanoparticles.

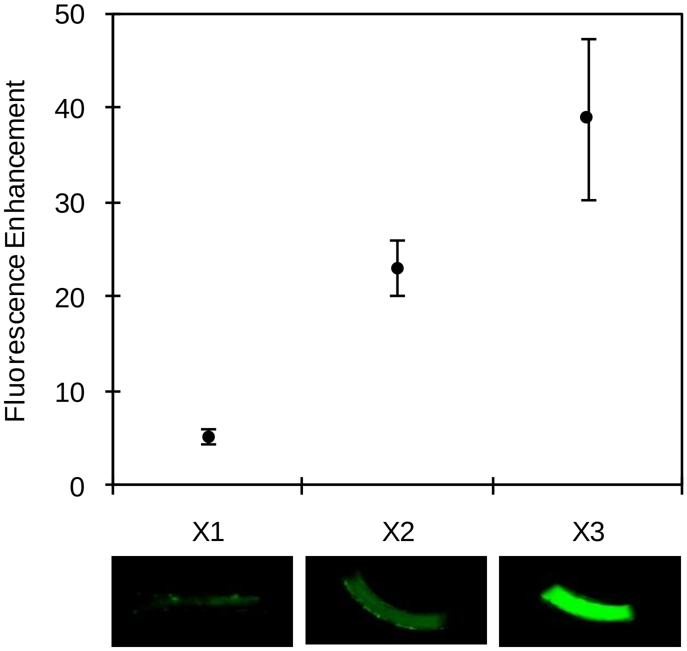

Figure 5.5. Effect of mixing efficiency on fluorescence intensity of droplets containing IRDye 800CW-SAv (1 µg mL^{-1}) in 0.1X PBS solution mixed with AgNP at a density of ~ 1x10^{7} particles nL^{-1}. Fluorescence was measured at three positions along the micromixer, designated as positions X1, X2, and X3, as shown in Figure 1(b). The protein conjugated fluorophores and AgNP form aggregates as the droplets progress through the serpentine micromixer. The aggregation process significantly enhances the fluorescence signal by amplifying the electromagnetic field around the aggregates, improving the excitation rate and increasing the scattering cross-section in the NIR, which enables the induced SPs to radiate into the far-field. The lack of an asymptotic trend in the data indicates that further enhancement may be achievable with increased mixing time or a more intense mixing process.

5.4. CONCLUSIONS

In conclusion, we demonstrate a 35-fold increase in the detected signal of NIR fluorophores with SEF of aggregated AgNP in a PMMA microchip using traditional fluorescence microscopy. Further, the relatively small standard deviations of fluorescence intensity prove this method consistent and reproducible. The use of our microfluidic device enables control of the aggregation process, easy manipulation of important parameters, and requires very small amounts of the dye and colloid solutions. The liquid-liquid droplet micromixer successfully aggregates the nanoparticles while maintaining individual packets of known contents for reproducible quantitative analysis. NIR fluorophores prove useful in researching SEF and should be taken into consideration when using continuous flow microdevices, especially when fabricated from commonly used plastics. Future research will aim to determine the maximum fluorescence enhancement achievable with our system and to further characterize the processes involved in nanoparticle aggregation and SEF for future improvement in quantum yield, photostability, and ultimately the LOD. System modifications, including the use of laser diode sources, will also be implemented to further improve the LOD.

CHAPTER 6. NEAR-INFRARED, SURFACE-ENHANCED FLUORESCENCE IN SOLUTION

This chapter is based on previously published work by the author[150]*. Copyright Springer and Plasmonics, 2013, in press, Near-infrared, surface-enhanced fluorescence using silver nanoparticle aggregates in solution, Furtaw, M.D., Anderson, J.P., Middendorf, L.R., and Bashford, G.R. Reprinted with kind permission from Springer Science and Business Media.*

6.1. INTRODUCTION

Fluorescence spectroscopy is used in many life science and clinical research diagnostic assays. Improvements in the sensitivity and LOD of these assays may have profound implications. In Chapter 5, it was demonstrated that salt concentration, AgNP concentration, and aggregation via mixing are important parameters that affect SEF. While the microfluidic format was useful for the preliminary research, current fluorescence users are not commonly using microfluidic-based assays. To address the use of SEF in a format more compatible with current assays, we now further investigate these parameters in a microtiter plate format to determine the achievable enhancement in signal and LOD. We demonstrate an easy-to-implement, inexpensive, NIR-SEF technique with 1000-fold LOD improvement of IRDye 800CW labeled streptavidin

(SAv-800CW) using ordinary immunoassay consumables and a NIR-fluorescence microtiter plate imager. We introduce the technique which relies on aggregation of SAv-800CW with AgNP at an optimized concentration of salt. We then verify that the technique applies to other NIR fluorophores with similar spectral characteristics. Finally, the technique is analyzed for possible assay implementation by characterizing its linearity, dynamic range, LOD, and repeatability.

6.2. MATERIALS AND METHODS

Materials. IRDye 800CW labeled streptavidin (SAv-800CW) and silver nanoparticles (AgNP) at stock concentration of ~20 nM with an average diameter of ~20 nm were obtained from LI-COR Biosciences (Lincoln, NE). DyLight 800 (Thermo Fisher Scientific, Rockford, IL) was purchased pre-conjugated to SAv, while Alex Fluor 790 (Life Technologies, Grand Island, NY) and CF790 (Biotium, Hayward, CA) were conjugated to SAv using a common NHS-ester labeling technique[114]. SAv powder, molecular biology grade, was purchased from United States Biological (Marblehead, MA). Sodium chloride (NaCl) was purchased from Sigma-Aldrich (St. Louis, MO). All dilutions were completed using ultrapure, Milli-Q water from an EMD Millipore system (Billerica, MA). All reagents were used as received unless otherwise noted.

Absorbance measurements. Absorbance (UV-VIS) measurements were made on an Agilent 8453 UV-visible spectrophotometer (Agilent Technologies Inc., Santa Clara, CA). Unlabeled streptavidin (SAv) was used for all absorbance measurements with AgNP so that the dye would not impact the absorbance curves. All measurements were taken with 10-fold diluted AgNP as the optical density cannot be measured reliably at stock concentration. AgNP absorbance was measured by adding 2 ml of AgNP (~ 2 nM) to 2 ml of dH_2O. The AgNP + SAv absorbance was measured by adding 2 ml of AgNP to 2 ml of 0.2 nM SAv in dH_2O. The AgNP + SAv & salt absorbance was measured by adding 2 ml of AgNP to 2 ml of 0.4 nM SAv in 5 mM NaCl. All absorbance measurements were taken after 1 hour incubation at room temperature in 4 ml plastic cuvettes. The cuvettes were carefully inverted 5 times prior to the measurement to re-suspend any larger aggregates.

Dynamic light scattering. Dynamic light scattering measurements were conducted on a 90Plus Particle Size Analyzer (Brookhaven Instruments Corp., Holtsville, NY) by adding 10 μl of solution from the absorbance cuvettes to 4 ml of dH_2O in new cuvettes. Polymer microspheres in water (Duke Scientific Corp., Palo Alto, CA), NIST traceable mean diameter 92±3.7 nm, were used as standards to ensure accuracy and stability of the instrument.

Electron microscopy. SEM images were acquired using a Hitachi S4700 field-emission scanning electron microscope (Hitachi High Technologies America Inc., Schaumburg, IL) at the University of Nebraska – Lincoln. The samples were immobilized on silicon wafers following a NIST-NCL joint protocol[151]. The immobilized samples were sputter-coated with a thin layer of nickel. TEM images were acquired using a Hitachi H7500 transmission electron microscope (Hitachi High Technologies America Inc., Schaumburg, IL) at the University of Nebraska – Lincoln. The samples were immobilized on silicon monoxide films supported with Formvar on a

200 mesh copper grid (Prod # 01830, Ted Pella Inc., Redding, CA) following a NIST-NCL joint protocol[152].

Fluorescence measurements. NIR-SEF was studied in 384-well optical bottom plates (Nunc, Rochester, NY) commonly used for immunoassays, including fluorescence-linked immunosorbent assays (FLISA) and enzyme-linked immunosorbent assays (ELISA). Figure 6.1(a) shows the steps which include: SAv-800CW dilutions, the addition of AgNP or dH_2O, sample incubation, and detection using an Odyssey Sa Infrared Imaging System (LI-COR Biosciences, Lincoln, Nebraska). Specifically, Step 1 involved the addition of 25 μl of SAv-800CW dilution in dH_2O or 5 mM NaCl, as labeled in Figure 6.1(b-c). Step 2 involved the addition of 25 μl of AgNP, at stock concentration (~ 20 nM), for NIR-SEF or dH_2O for reference fluorescence. The plate was then incubated in the dark at room temperature for 1 hour, allowing only diffusion-limited mixing. Immediately following incubation, images were acquired at several detector gain intensities, Step 3, to make use of the maximum dynamic range of the instrument. Raw images (in pseudocolour) at the lowest and highest gain intensity are shown in Figure 6.1(b-c). All sample data values were corrected for detector gain setting, using the value for each well at the highest gain prior to detector saturation. The Odyssey Sa is a bottom-reading, point-scanning fluorescence imager with a solid-state diode lasers at 685 and 785 nm for excitation and filtered silicon avalanche photodiodes for detection. The 785 nm laser is used throughout this study.

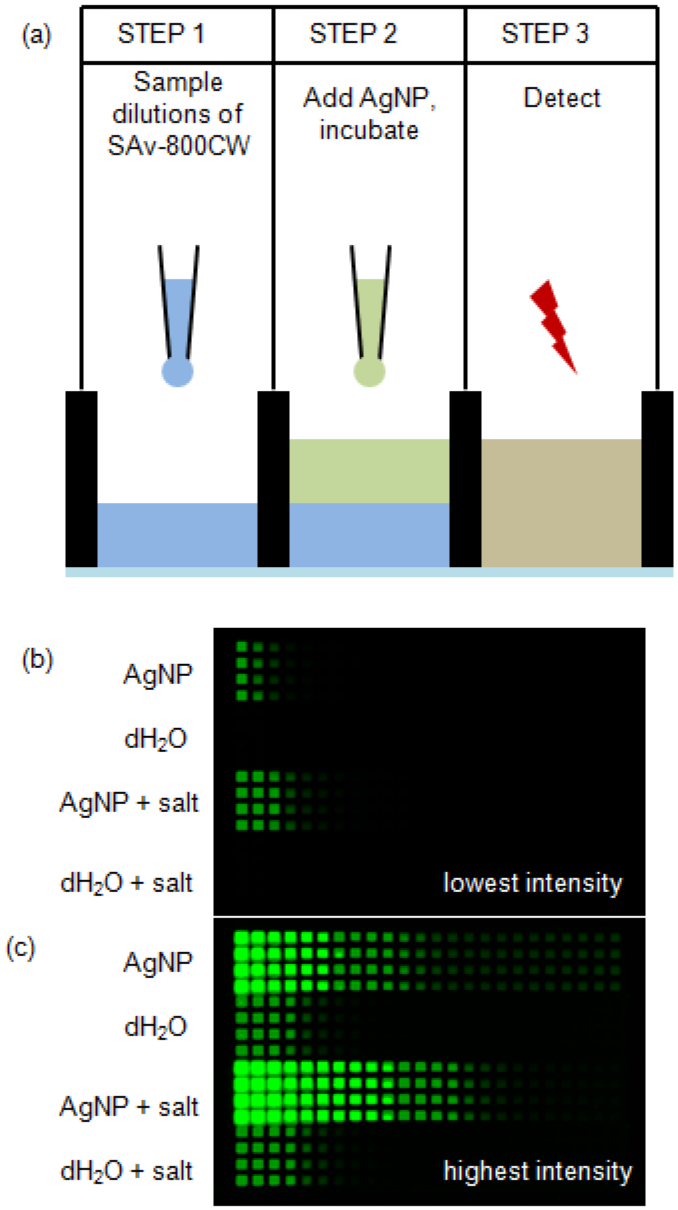

Figure 6.1. Diagram showing the 3 steps (a) required to enhance the fluorescence of SAv-800CW. Sample dilutions of the protein-dye conjugate, two-fold from 16.4 nM to 7.8 fM, along with two columns of background (right most) were imaged with various detector gain intensities to extend the dynamic range of the assay. Raw images at the lowest (b) and highest (c) intensity are shown, which differ by 1024-fold.

Data processing. All fluorescence data were normalized to detector gain intensity of 11 by

$$I = I_n \cdot 2^{11-n} \qquad (1)$$

where n is the detector gain intensity. The values for all sample wells were taken at the highest detector gain intensity prior to detector saturation. In order to verify the linearity of the instrument across all detector gain settings, one sample well for each data set were corrected from multiple images (Figure 6.2). This analysis also shows signal intensity remains constant over the 30 minutes of image acquisition (approximately 5 minutes for each image at differing scan intensity). The constant signal intensity suggests that aggregate sedimentation is not responsible for signal enhancement by bringing more fluorophores into the depth of field of the instrument (FWHM = 1.5 mm). If sedimentation were significant, one would expect an increase in signal with time. The only other possibility is that sedimentation fully completed within the 1 hour incubation period which is not plausible. Even so, if sedimentation did occur it could only be responsible for a modest amount of enhancement as the original sample depth is only about 3 times the depth of field of the instrument.

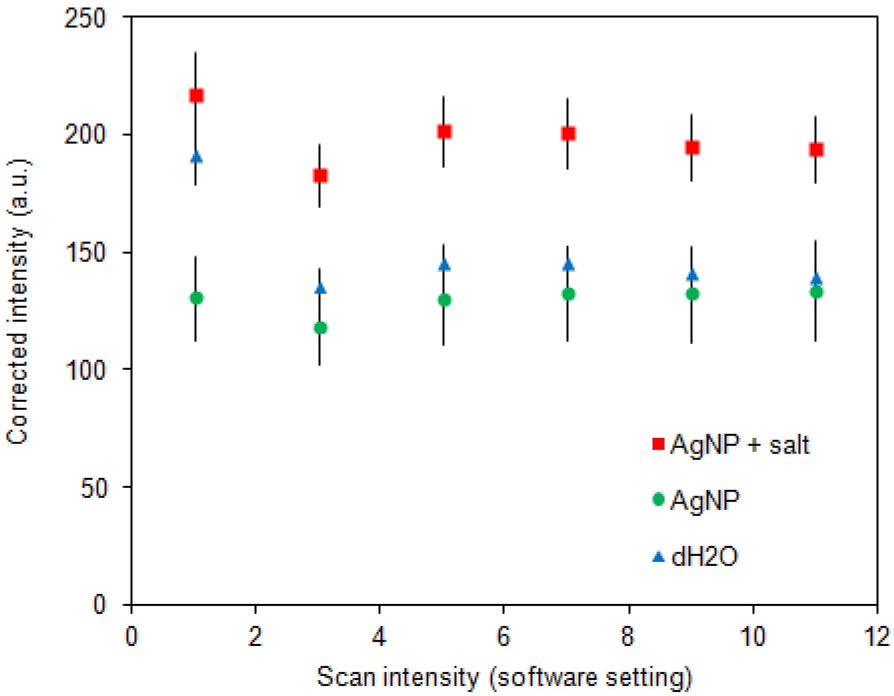

Figure 6.2. Corrected intensity for one set of wells of each treatment at all detector gain settings. Error bars indicate +/- 1 standard deviation at each data point. The first data points (intensity = 1) may be too small to be considered within the linear range. The near-constant value of the rest of the corrected intensities suggests the instrument is linear across all detector gain settings.

Enhancement calculations. Fluorescence enhancement was calculated by

$$SEF = \frac{I_{sample} - I_{background,sample}}{I_{reference} - I_{background,reference}} \qquad (2)$$

Where the sample background was AgNP added to dH_2O or 5 mM NaCl and the reference background was dH_2O.

6.3. RESULTS AND DISCUSSION

SEF by AgNP aggregation. Our technique for NIR-SEF relies on citrate-stabilized, AgNP monomers fabricated by a proprietary process based on conventional methods[98, 99]. It has been demonstrated in previous research that aggregation of plasmon-active nanoparticles can lead to 'hot spots', where the local electric field can increase by several orders of magnitude[153]. It is also known that the process of aggregation can shift, or reduce, plasmon resonance allowing interaction with a broader spectrum of light. The aggregation process is a crucial ingredient in our NIR-SEF technique. The other crucial ingredient is our use of dye-labeled SAv. It is well known that direct contact between a fluorophore and the plasmonic structure will lead to quenching[154]. This problem is solved by using a fluorophore-labeled protein, or DNA strand, to maintain separation between the emitter and the nanostructure surface. We chose SAv as the labeled carrier protein due to its size, symmetry, ability to interact with AgNPs, and its common use in immuno-affinity assays (see Chapter 4). At a certain pH, SAv will interact with negatively charged, citrate-stabilized AgNPs to create dimers, trimers, and other low order aggregates, see Figure 6.3. This is accomplished when SAv, a tetrameric protein, attaches to the surface of two AgNPs, effectively cross-linking them. Importantly, SAv is the size of a cube with 5 nm sides which geometrically prevents it from interacting with more than two 20 nm AgNPs simultaneously. Therefore, the molar ratio between SAv and AgNPs may significantly affect the aggregate size produced through SAv-AgNP interactions alone. When the concentration of AgNPs is significantly larger than that of SAv, as in this study, it is expected that the aggregates are primarily in the form of dimers with some other low order aggregates present along with many non-aggregated monomers. Further aggregation occurs by the addition of salt which screens the negative surface charge on the citrate-stabilized AgNP monomers enabling AgNP-AgNP interactions.

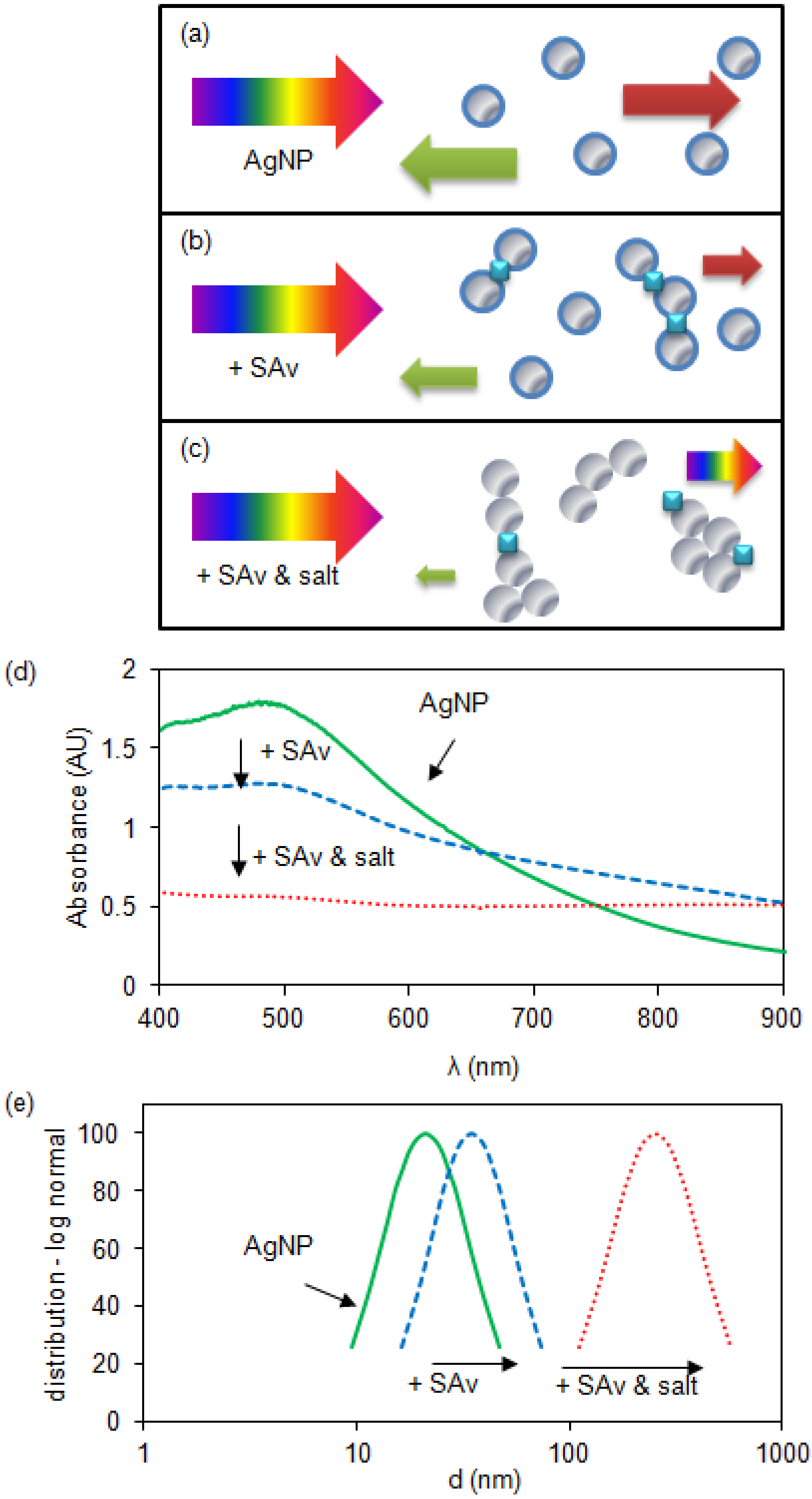

Figure 6.3. Diagram showing the optical response and structural mechanisms of AgNP monomers and the formation of aggregates by SAv, with and without salt. The

monomers (a) reflect green and transmit red light while remaining stable due to a negative surface charge (shown in blue). The addition of SAv (b) enables aggregate formation solely by SAv-AgNP interactions which reduce green reflectance and red transmittance. The addition of SAv with an appropriate amount of salt (c) screens the negative surface charge and enables aggregation from both SAv-AgNP and AgNP-AgNP interactions, causing larger aggregates with a further reduction in green light reflectance while enabling transmittance of the full spectrum. The measured absorbance spectrum (d) and particle/aggregate size distribution (e) are also shown. The mean effective diameters (weighted by number), via dynamic light scattering, for AgNP alone, with SAv, and with SAv and salt are 21, 35, and 252 nm, respectively. The absorbance spectrum of the AgNP monomers is broader than expected with Mie theory due to the presence of larger particles within the polydisperse sample.

Optimal salt concentration. The aggregation process is highly dependent on salt concentration. Some amount of salt is required to reduce the monomer zeta potential sufficiently to enable collisions. Too much salt completely removes the particle charge and allows the AgNPs to precipitate out of solution. The optimal salt concentration (under our conditions) was found by conducting a 2-D dilution experiment in a 384-well plate. The columns contained varied salt concentration from 200 mM down to 0.2 mM NaCl in 2-fold dilutions (2 columns per dilution) with the final 2 columns containing dH_2O. The rows contained varied SAv-800CW concentration from 500 ng/ml down to 500 fg/ml in 10-fold dilutions (2 rows per dilution), with the final 2 rows being background wells. The data (Figures 6.4-6.5) show an optimal salt concentration near 5 mM NaCl. The data also show that the signal is linear over the range used of SAv-800CW, for multiple concentrations of NaCl. This indicates that slight variation in salt concentration should not significantly affect the ability to detect and quantitate the dye with our NIR-SEF protocol. The optimal concentration of 5 mM NaCl was used throughout this study.

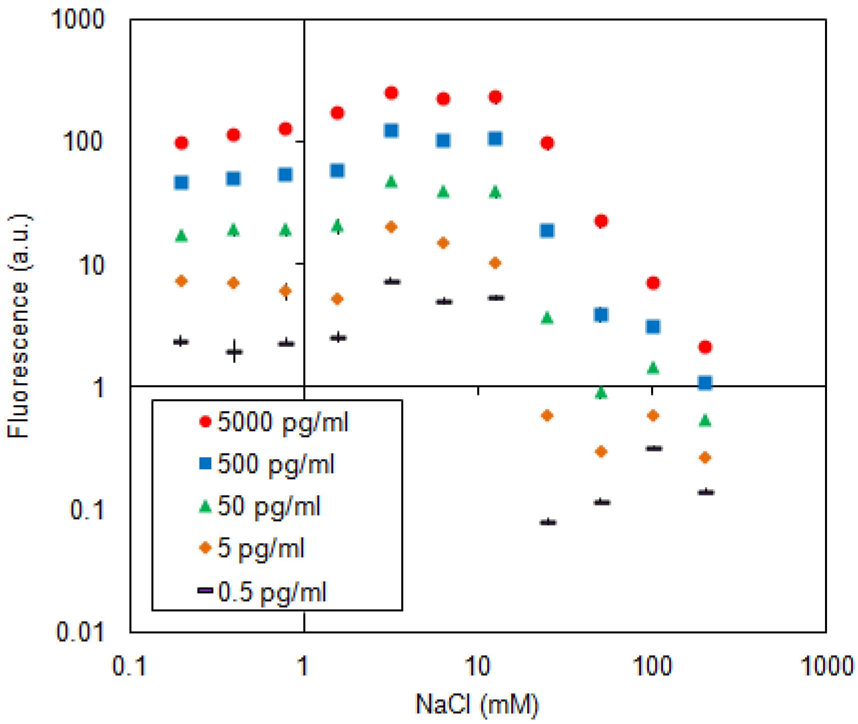

Figure 6.4. Fluorescence intensity versus NaCl at multiple concentrations of SAv-800CW. Error bars indicate +/- 1 standard deviation for each data point.

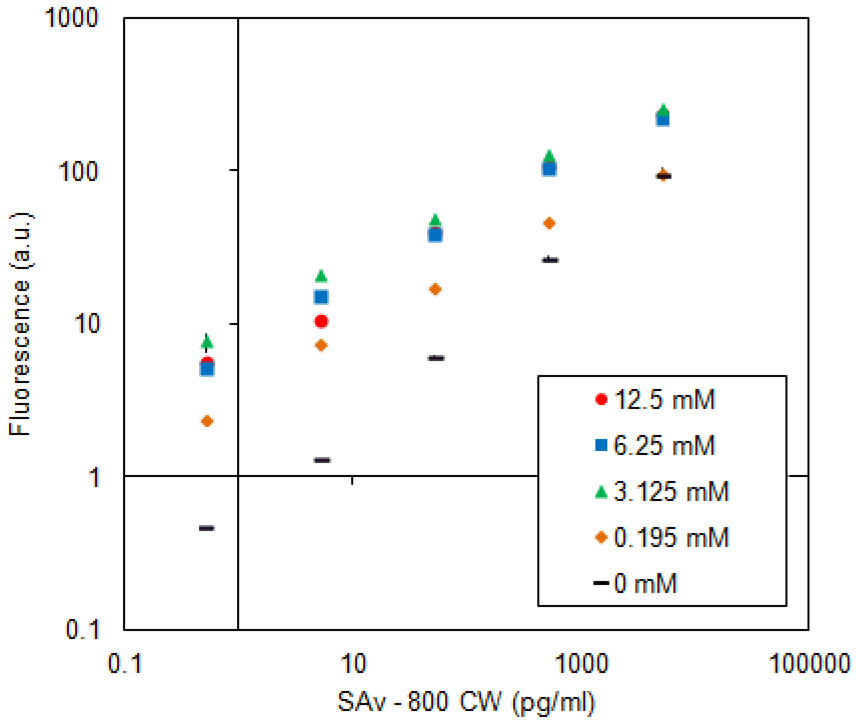

Figure 6.5. Fluorescence intensity versus SAv-800CW at multiple concentrations of NaCl. Error bars indicate +/- 1 standard deviation for each data point.

Electron microscopy images of AgNP monomers and aggregates. Images of the AgNP monomers were acquired using SEM. The images (Figures 6.6-6.7) show diameters in good agreement with the DLS average of 21 nm. Images of AgNP aggregates were acquired using TEM. It is important to point out that it is very difficult to immobilize salt-induced aggregates without affecting the morphology due to the inherent instability in the aggregate solution. The images presented here (Figures 6.8-6.10) should be taken as qualitative representations of the aggregates and visual proof of the aggregation process. The actual aggregates in solution may differ from those immobilized during the TEM imaging process.

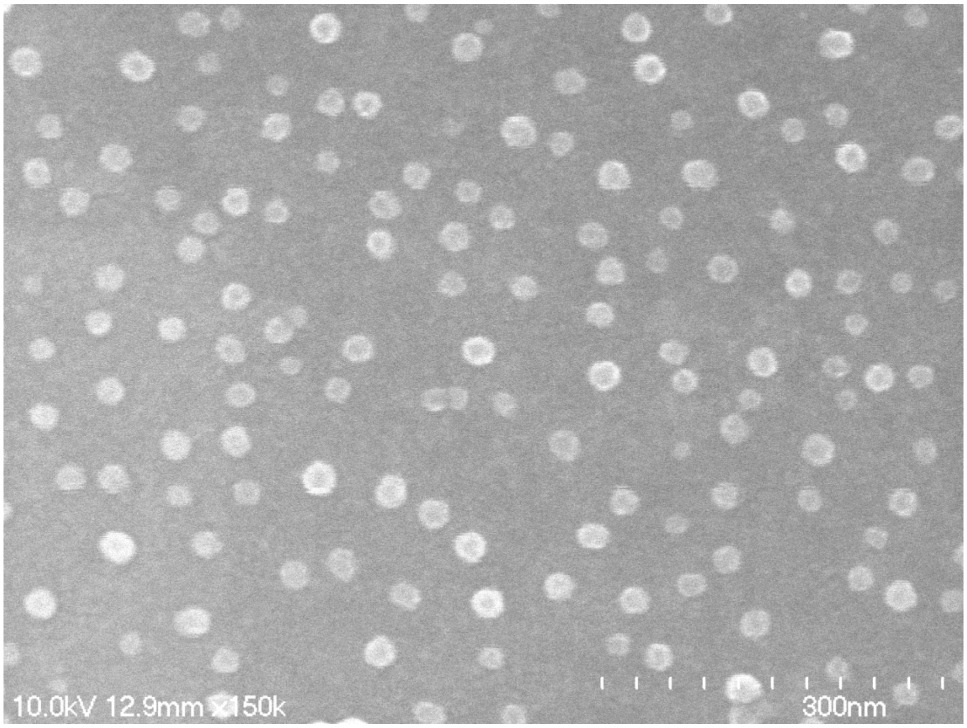

Figure 6.6. SEM image of AgNP monomers. The size of the individual nanoparticles appear to be in good agreement with the DLS average of 21 nm.

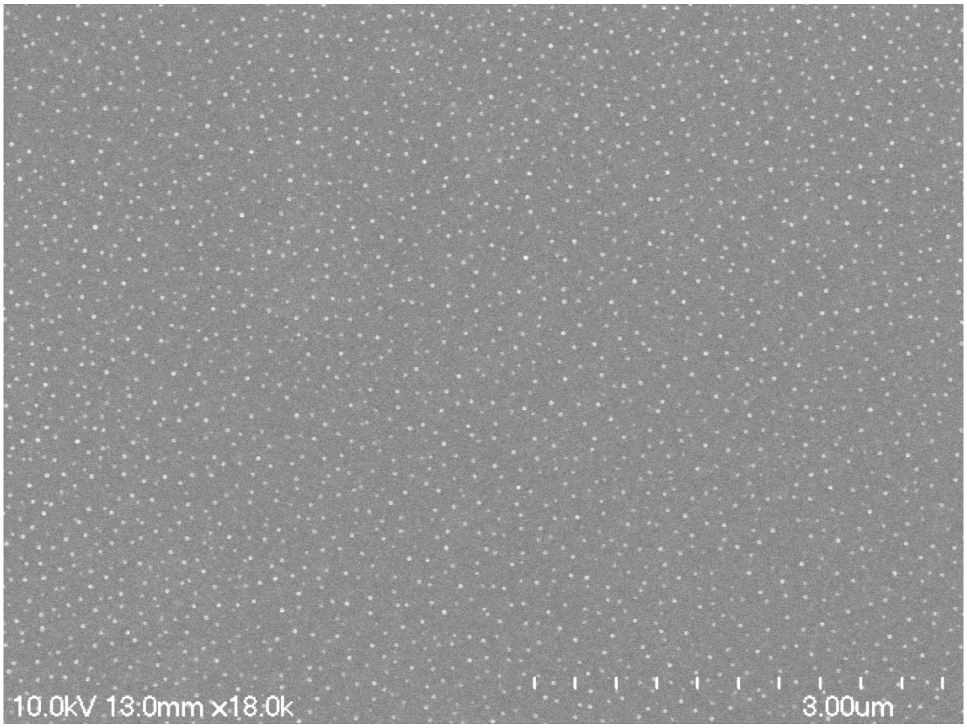

Figure 6.7. SEM images of AgNP monomers in wider field-of-view.

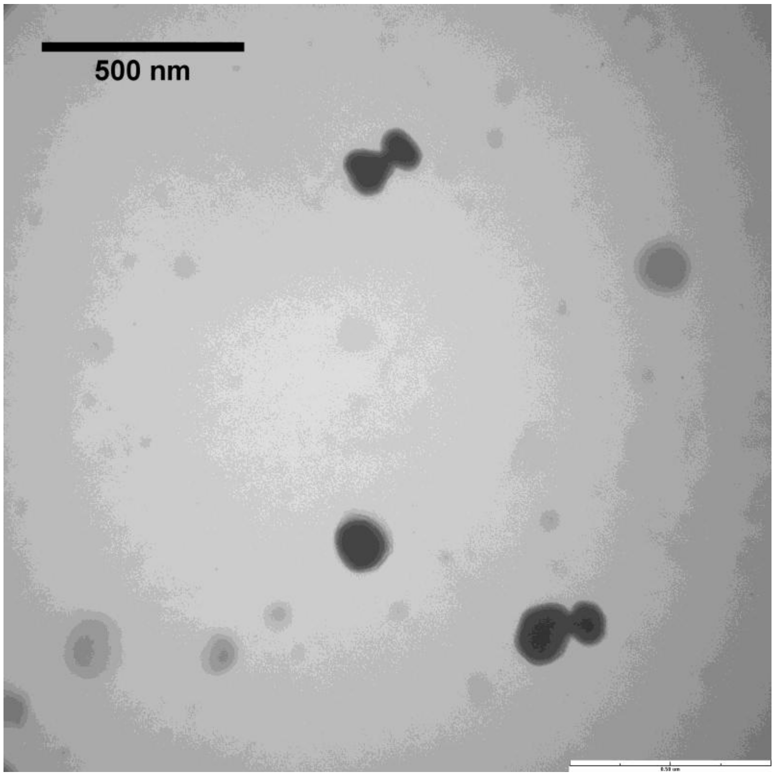

Figure 6.8. TEM image showing a monomer and two dimers formed by adding SAv to the AgNP solution.

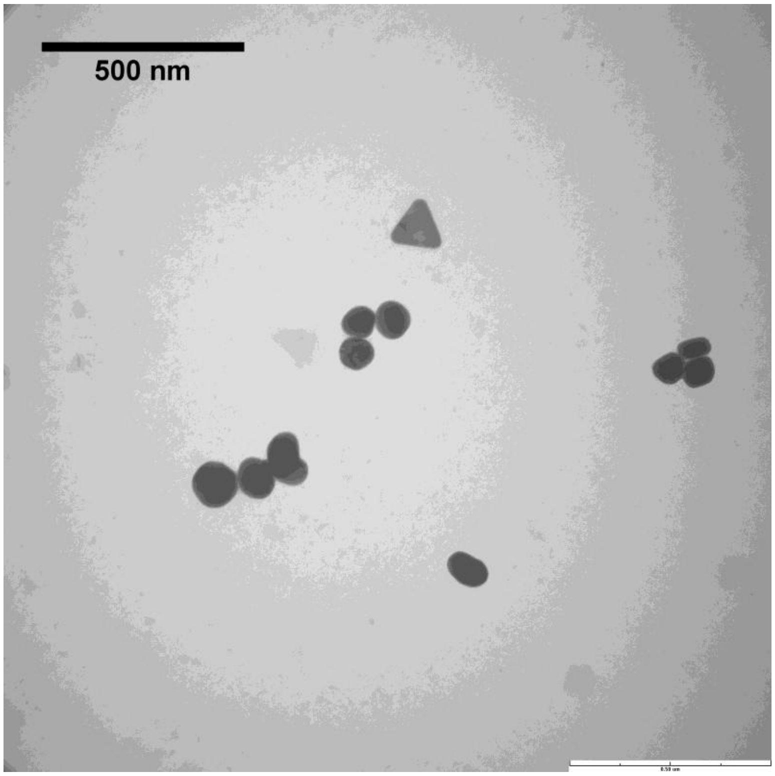

Figure 6.9. TEM image showing trimers formed after adding SAv and salt to the AgNP solution. Notice the presence of a triangular plate, which do not show up often in EM images, so they are expected to contribute very little, if at all, to the SEF process.

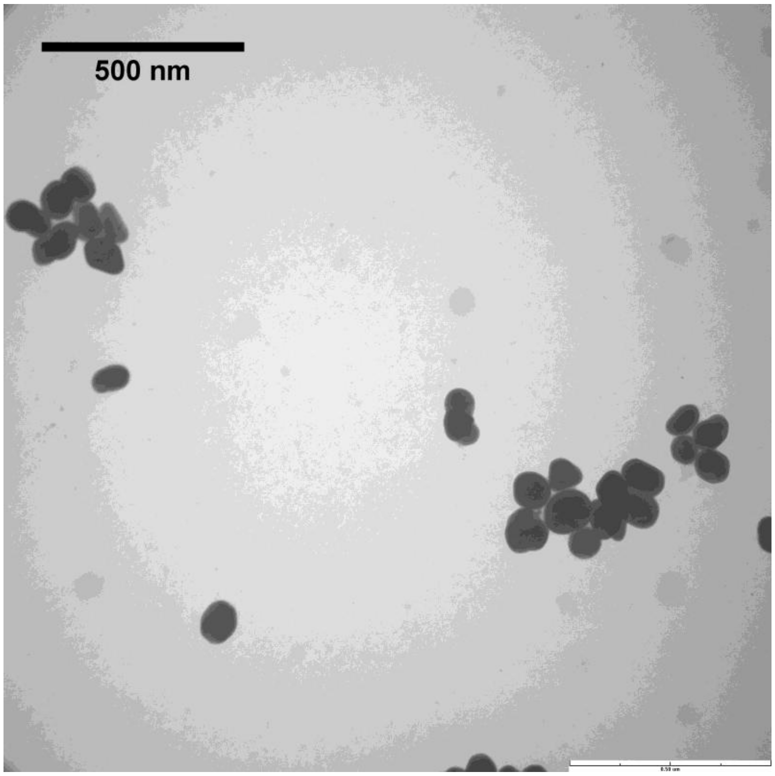

Figure 6.10. TEM image showing higher-order aggregates after adding SAv and salt to the AgNP solution. It appears salt-induced agglomeration may be occurring, which is consistent with previous work[149]. It is unknown at this time what this process contributes to the observed SEF.

SEF of SAv-800CW. Figure 6.11 shows fluorescence enhancement with and without salt for each SAv-800CW dilution where the reference fluorescence was detectable and thus, enhancement could be calculated. Each dilution was replicated in 4 wells and the standard deviations are included in the figure. All values represent ensemble enhancement as opposed to the enhancement of individual fluorophores. The maximum enhancement of 2530-fold for AgNP and salt at the lowest concentration of SAv-800CW is within 3-fold of the largest ensemble enhancement, to the authors' knowledge, previously published[102]. The maximum enhancement may even exceed this value at lower concentrations; however, the reference dilutions could no longer be detected. The enhancement is relatively constant, with and without salt, across the 11 dilutions in which the reference could be detected. Since aggregation without salt is dependent on SAv-linking, the distance between two AgNPs in that situation is approximately 5 nm. The ability of SAv to bind two AgNPs seems to enable it to generate and locate within these ‘hot spots’ which is demonstrated by the 241-fold average enhancement when no salt is added. Aggregation with salt gives around five-fold better results than without salt. This may be due to further enhanced electric fields near and between AgNPs in contact with one another. Previous numerical simulations have shown near-field intensity dependent on the number of particles in an aggregate[155]. In their study, aggregates of AgNP create near-field enhancements up to 640-fold when excited at 780 nm, which may explain the magnitude of enhancement in this study. Increased excitation rate must be responsible for most of the enhancement as less than 10-fold can be expected due to quantum yield (q^0~0.07 for IRDye 800CW[95]). This is further suggested by the fact that other fluorophores with similar spectral properties all show SEF well over 100-fold despite having differing intrinsic quantum yields (see below).

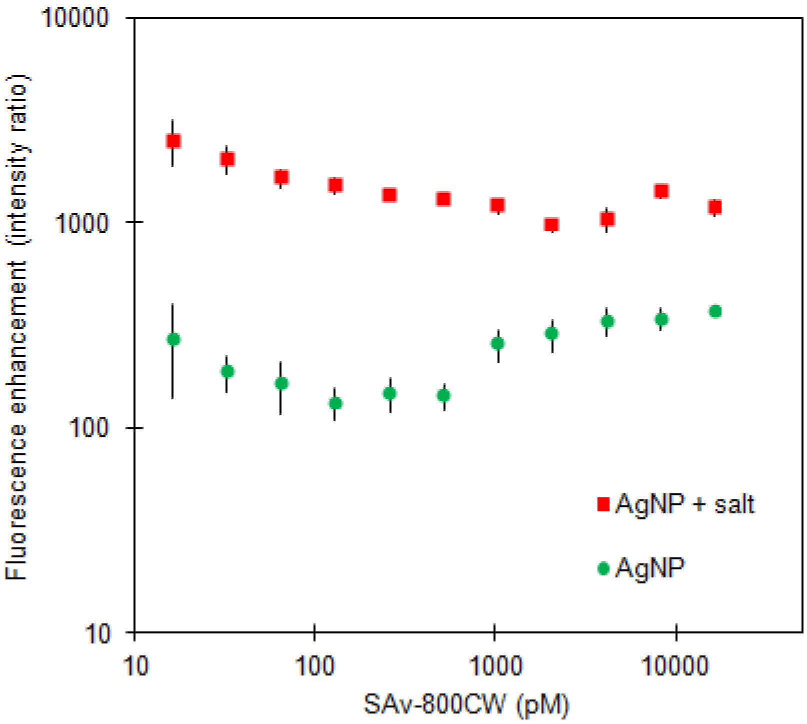

Figure 6.11. Surface enhanced fluorescence versus the molar concentration of SAv-800CW for AgNP, with and without salt. Error bars indicate +/- 1 standard deviation at each data point. The overall average enhancement with salt was 1484-fold with a maximum of 2530-fold, while the overall average without salt was 241-fold with a maximum of 376-fold.

SEF of various NIR fluorophores. The technology was also tested on other NIR fluorophores conjugated to SAv with similar spectral properties to IRDye 800CW. The table below summarizes the fluorophores along with their physical characteristics (per manufacturer websites).

Table 6.2. Physical characteristics of various NIR fluorophores (per manufacturers).

Fluorophore	$\lambda_{abs,max}$	$\lambda_{em,max}$	$\varepsilon_{\lambda abs,max}$
Alexa Fluor 790	782	805	260,000
DyLight 800	777	794	140,000
IRDye 800CW	778	794	240,000
CF790	784	806	210,000

Figure 6.12 shows the fluorescence enhancement for the various fluorophores. The enhancement is very similar for all of the fluorophores tested. Some variation is expected as the fluorophores have differing intrinsic quantum yield[156] and absorption/emission spectra. It is unclear at this time as to why the salt-induced aggregation provided less enhancement for the CF790.

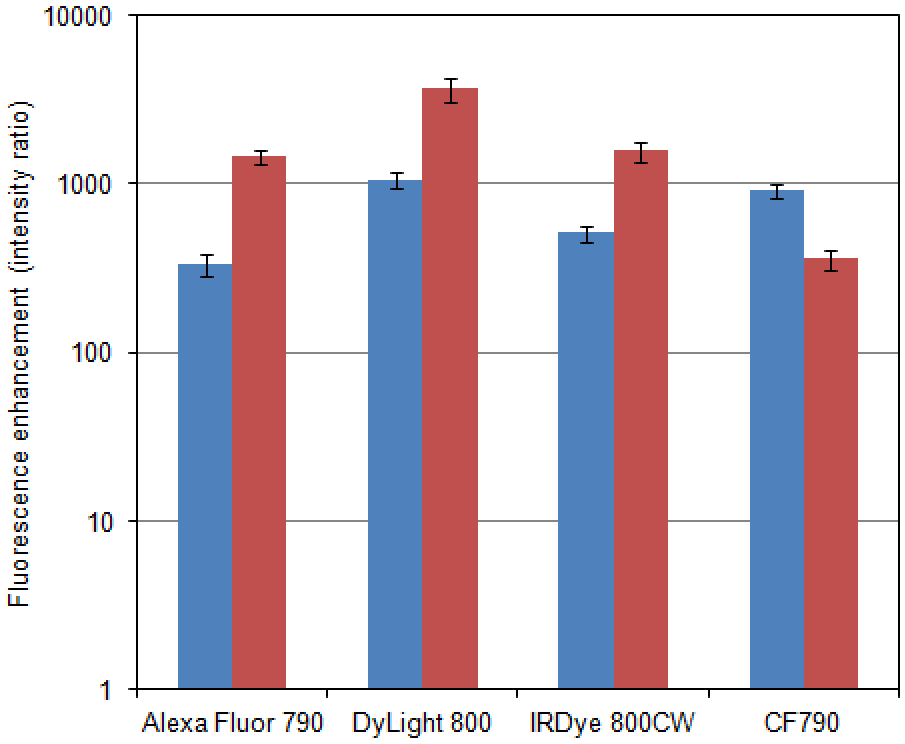

Figure 6.12. Fluorescence enhancement for various NIR fluorophores with AgNP only (blue) and AgNP with salt (red). Error bars indicate +/- 1 standard deviation for each data point.

Assay potential. Due to the magnitude of potential fluorescence enhancement, translation into real-world assays is the next step in our long-range goals. A few characteristics of useful assays include linearity, a large dynamic range, low LOD, and repeatability. These characteristics were analyzed on our NIR-SEF technique. Figure 6.13 shows the fluorescence intensity versus SAv-800CW concentration for reference samples, as well as NIR-SEF with and without salt. All three samples have good linearity prior to approaching their respective LOD (defined as 3 standard deviations above the respective mean background intensity). The dynamic range of SAv-800CW alone (using the described detection system) extends beyond the concentrations included in this study by three orders of magnitude. Our NIR-SEF technology, however, cannot be extended above the range shown in Figure 6.13 as the detector signal saturates at the lowest intensity setting on the instrument. NIR-SEF does extend the dynamic range on the low end, though. NIR-SEF with salt improved the LOD over 1000-fold, while AgNP without salt successfully enhances the signal but only improves the LOD by 4-fold. The addition of salt not only increases the intensity of the signal, it also shows lower background signal. This may be due to the fact that the AgNP without salt remain primarily as monomers (especially at low concentrations of SAv-800CW) and scatter more light than the AgNP aggregates formed upon the addition of salt. This is contrary to the absorbance curves shown in Figure 6.3 since they were acquired in the presence of relatively large amounts of SAv. The background wells did not include any SAv-800CW and it has been found that the optical density of AgNP alone is reduced upon the addition of salt at all wavelengths in the visible to NIR (data not shown). Using these results, a combination assay (e.g. fluorescent-linked immunosorbent assay, FLISA) in which NIR-SEF is employed after regular fluorescence detection to extend the dynamic range and LOD beyond current assay limitations, while maintaining linearity at higher concentrations, could potentially be developed. Furthermore, the technique has proved to be repeatable indicated by the error bars (+/- 1 standard deviation) in Figure 6.11 and Figure 6.13 (which cannot be seen in Figure 6.13 as the standard deviations are smaller than the data point symbols on the logarithmic scale). Nonetheless, incorporating this technique into ‘real-world’ assays is non-trivial. This technology relies on the aggregation of AgNP with SAv-800CW. Therefore, the SAv-800CW, which is generally immobilized during an immuno-affinity assay, must either be re-mobilized or somehow accessible to the AgNP. Future work will focus on determining ways to achieve this requirement. It should be noted that the LOD of some immunoassays (e.g., enzyme-linked immunosorbent assay, ELISA) may be limited by antibody specificity, rather than signal intensity. Yet, there remains a need for signal amplification, as it has been shown that antibodies can be used at diluted concentrations to reduce non-specific binding (when there is adequate signal) and thus improve the LOD[157]. Also, signal improvement may lead to achievement of current detection limits with less expensive optics, which may be particularly attractive for clinical applications as well as locations with limited resources.

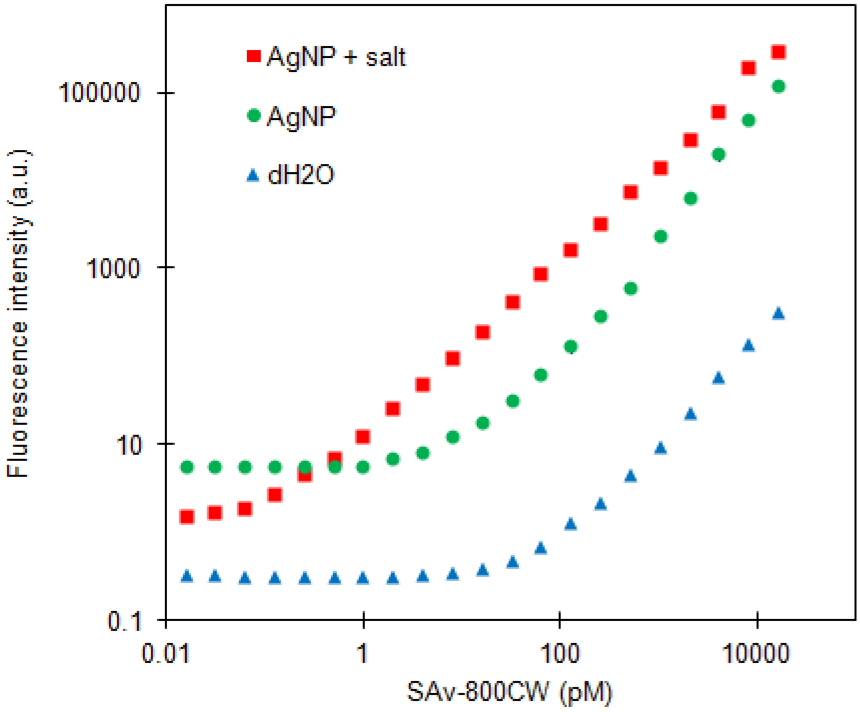

Figure 6.13. Fluorescence intensity versus molar concentration for SAv-800CW alone, with AgNP, and with AgNP and salt. Error bars at +/- 1 standard deviation at each data

point are included, though they are smaller than the data markers and therefore hidden. The experimental LODs were 16, 4, and 0.0156 pM for SAv-800CW alone, with AgNP, and with AgNP and salt respectively.

6.4. CONCLUSIONS

In summary, we have demonstrated a NIR-SEF technique that enhances the signal of SAv-800CW up to 2530-fold while improving the LOD over 1000-fold. The technique also has the advantage of being easy to implement while maintaining compatibility with commercially available immunoassay instrumentation and microtiter plates. Our NIR-SEF technique makes use of non-functionalized, citrate-stabilized AgNPs that aggregate at an optimal salt concentration. Future research will focus on applying this technology to a common immunoassay (FLISA) (Chapter 7), adapting the technology to other assay formats, including surface-based assays such as Western blots, and investigating the potential to multiplex with other fluorophores for multiple biomarker assays. This technology may ultimately lead to improved and novel assays for life science research as well as clinical diagnoses.

CHAPTER 7. A NEAR-INFRARED, SURFACE-ENHANCED FLUOROPHORE-LINKED IMMUNOSORBENT ASSAY

This chapter is based on previously published work by the author[158]*. Reprinted (adapted) with permission from Analytical Chemistry, 85, 2013, 7102-7108, A near-infrared, surface-enhanced, fluorophore-linked immunosorbent assay, Furtaw, M.D., Steffens, D.L., Urlacher, T.M., and Anderson, J.P. Copyright 2013 American Chemical Society.*

7.1. INTRODUCTION

The enzyme-linked immunosorbent assay (ELISA) is one of the most widely used among all assay techniques in clinical and research settings. While ELISA is sufficient for many clinical and research diagnoses, the method may be inadequate for some biomarker implementations and development. ELISA typically involves the detection of a colorimetric product which can limit its linear range and inherently limits the ability to simultaneously measure multiple antigens of interest. The fluorophore-linked immunosorbent assay (FLISA) is a closely related technique which may offer some advantages including an extended linear range and multiplexed detection. It would be beneficial to enhance the sensitivity of the FLISA assay in order to maintain its advantages while matching or surpassing the sensitivity of the ELISA assay. Importantly, the optimal technology should improve assay sensitivity and LOD while maintaining current assay workflow with a minimal learning curve.

In this chapter, we introduce a surface-enhanced, fluorophore-linked immunosorbent assay (SEFLISA) which maintains the traditional FLISA protocol and adds two simple steps to the end that significantly improve LOD and sensitivity. The mechanisms involved are explained using the accumulated knowledge from previous work along with insight from Chapters 3-6 in this dissertation. The SEFLISA technique works with direct and sandwich FLISA (see Figure 7.1). We evaluate the performance on a model-system using direct SEFLISA to detect rabbit immunoglobulin-G (IgG) as well as a clinically relevant, sandwich SEFLISA to detect alpha-fetoprotein (AFP).

As mentioned above, the FLISA technique is a closely-related modification of the more commonly used ELISA. Specifically, FLISA makes use of a fluorophore covalently linked to the detection antibody instead of an enzyme as used in ELISA. After probing with the detection antibody, a FLISA assay is ready for detection with a fluorescence plate reader, whereas ELISA still requires enzyme substrate incubation prior to detection with a colorimetric or chemiluminescence plate reader. A major drawback with enzyme-based assays can be the lack of an extensive linear range. This is particularly problematic at high antigen concentrations as the enzyme-based assays become non-linear due to substrate limited kinetics, followed by saturation of the detector signal. An additional drawback with colorimetric-based detection is high background signal due to any contamination that may absorb light in the visible spectrum, which can limit the linear range at the low-signal end. Fluorescence-based detection often demonstrates significantly broader linear range, partially by reducing background. The use of near-infrared (NIR) fluorophores can further reduce the background due to lower autofluorescence[30] and scatter in comparison to visible dyes. Background reduction is ultimately limited by antibody specificity which remains a problem common to all immunoassay techniques.

Previous studies employing NIR-SEF to improve assay sensitivity typically suffer from difficult fabrication processes and/or incompatibility with traditional assay workflows. Our technique for SEFLISA improves upon previous work by enabling significant improvements in sensitivity and LOD with only two additional steps beyond the traditional FLISA. Further, the technique allows the traditional FLISA to be fully completed with detection prior to any assay modifications. This maintains the current linear range of FLISA while extending the low end with SEFLISA. In fact, one could choose to employ the SEFLISA technique only after verifying that the traditional FLISA lacked the sensitivity or detection capability for the specific sample. This is particularly attractive for technology adoption since a current FLISA user could attempt the SEFLISA technique without the risk of data loss from precious sample.

7.2. MATERIALS AND METHODS

Materials. IRDye 800CW labeled streptavidin (SAv-800CW), Odyssey blocking buffer, protease K salt solution, and silver nanoparticles (AgNP) were obtained from LI-COR

Biosciences (Lincoln, NE). Rabbit IgG was purchased from Rockland Immunochemical (Gilbertsville, PA). Biotinylated donkey anti-rabbit antibody was purchased from Jackson ImmunoResearch (West Grove, PA). Human alpha-fetoprotein capture antibody, biotinylated detection antibody, and recombinant standard were all purchased as a development kit from R&D Systems (Minneapolis, MN). All reagents were stored and prepared according to manufacturer recommendations. All dilutions and buffers were made with ultrapure, Milli-Q water from an EMD Millipore system (Billerica, MA).

Absorbance measurements. Absorbance (UV-VIS) measurements were made on an Agilent 8453 UV-visible spectrophotometer (Agilent Technologies Inc., Santa Clara, CA). The AgNP solution was diluted 10-fold to be within the linear range of the instrument. The absorbance spectra of AgNP with SAv, with and without salt, were acquired by incubation of the diluted AgNP solution with 100 ng/ml SAv in dH_2O or 5 mM NaCl for one hour prior to the measurement. This is a relatively high concentration of SAv in order to demonstrate the aggregation.

Dynamic light scattering. Dynamic light scattering (DLS) measurements of the AgNP solution was conducted on a 90Plus Particle Size Analyzer (Brookhaven Instruments Corp., Holtsville, NY) in optical grade poly(methyl methacrylate) cuvettes. Polymer microspheres in water (Duke Scientific Corp., Palo Alto, CA), NIST traceable mean diameter 92±3.7 nm, were used as standards to ensure accuracy and stability of the instrument.

Electron microscopy. AgNPs were immobilized on 5 mm square, ultra-flat thermal silicon dioxide wafers (Ted Pella, Redding, CA) for imaging with a Hitachi

S4700 field-emission scanning electron microscope (Hitachi, Schaumburg, IL). The wafers were prepared and AgNPs immobilized according to a NIST-NCL joint assay protocol[151].

Fluorescence measurements. Emission spectra were acquired in optical grade poly(methyl methacrylate) cuvettes using a QuantaMaster spectrofluorometer (Photon Technology International, Birmingham, NJ). Plate-based fluorescence measurements, including assays, were made in 96-well, black, high-bind, optical bottom plates (Corning Life Sciences, Tewksbury, MA) using an Odyssey Sa infrared imaging system (LI-COR Biosciences, Lincoln, NE).

SEFLISA assays. Figure 7.1 shows the steps for direct FLISA, sandwich FLISA, and the two additional steps required for SEFLISA enhancement. Step-by-step protocols are provided in Appendix B. Briefly, FLISA assays were completed using standard protocols. A solution of protease K and salt is then added to cleave the antibody/antigen sandwich to free the SAv-800CW. AgNPs are then added to form aggregates with the remobilized SAv-800CW in the salt solution. Proteins are able to non-specifically assemble on citrate-stabilized nanoparticles through electrostatic interactions, depending on pH and salt content in solution[159]. The AgNPs are also able to form aggregates with other antibodies, whole and fragments, however these additional interactions are not problematic. The aggregation process of the AgNP is further enabled through a reduction of surface charge in salt solution (Figure 7.2(b)).

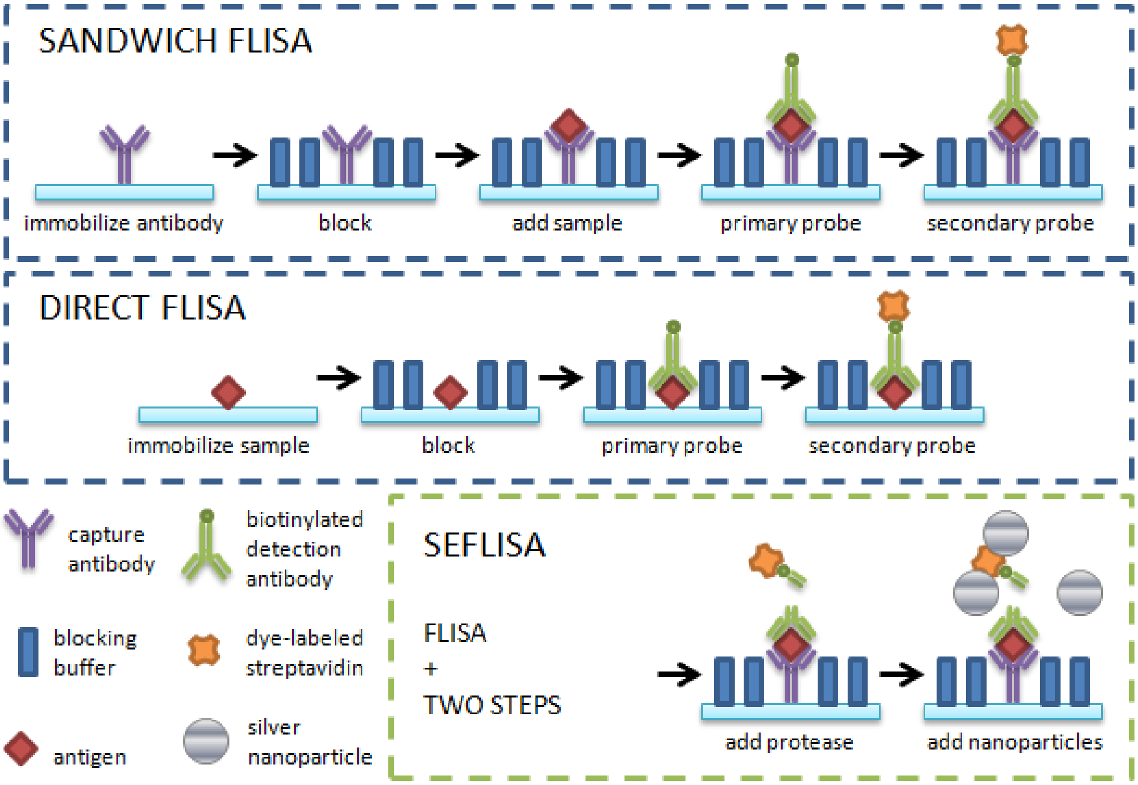

Figure 7.1. Diagram showing the workflows of sandwich FLISA, direct FLISA, and the two additional steps required to increase sensitivity using surface-enhanced fluorescence.

Protease efficiency. Biotinylated bovine serum albumin (b-BSA) was serially diluted 2-fold to create 10 samples between 20,000 and 39 ng/ml using 40 µM BSA in 0.1X PBS as the diluent. A volume of 100 µl of each sample was added, in quadruplicate, to the corresponding columns of a 96-well microtiter plate. The plate was covered and incubated for 1 hour at room temperature on a plate shaker. The plate was then inverted to dump out the sample. Each well was washed with 300 µl of PBS 3 times for 2 minutes each on a plate shaker. A volume of 300 µl of Odyssey blocking buffer was added to each well, covered, and incubated for 1 hour at room temperature on a plate shaker. The blocking buffer was then dumped by inverting the plate. A volume of 100 µl of SAv-800CW, diluted 1:10,000 in Odyssey blocking buffer, was added to each well, covered with seal and foil, and incubated for 1 hour at room temperature on a plate shaker. The plate was then inverted and washed, as before. Protease K salt solution (250X) was diluted 1:250 in dH_2O. A volume of 50 μl of protease K solution was added to each well in 2 rows of the plate, with dH_2O added to the other 2 rows. The plate was covered with seal and foil and incubated for 30 minutes at room temperature on a plate shaker. The plate was then inverted and washed, as before. Finally, 50 μl of dH_2O was added to each well before scanning the plate on an Odyssey Sa with a focus offset of 3.4 mm at an intensity of 9.

SDS-PAGE analysis of assay supernatant. The protocol for a direct SEFLISA using a 10-fold dilution series of rabbit IgG from a concentration of 1000 to 0.001 ng/ml was followed (see Appendix B), except for the final section using AgNP. Immediately after the protease treatment, 30 μl of solution was collected from each well and combined with 10 μl of loading buffer. The samples were incubated at 70°C for 10 minutes in order to denature the proteins. SDS-PAGE of each sample was performed using NuPAGE 4-12% Bis-Tris gels. Also, SAv-800CW and 800CW ladder with the same pre-treatment was loaded for comparison.

7.3. RESULTS AND DISCUSSION

Surface-enhanced fluorescence of IRDye 800CW. Citrate-stabilized AgNPs were fabricated by a proprietary method based on commonly used methods[98, 99]. Figure 7.2(a) shows the relative distribution of size, as determined by DLS, which gave an average diameter of 21 nm. DLS measurements were confirmed using scanning electron microscopy (SEM) as shown in the inset. The absorbance of the AgNP solution is shown in Figure 7.2(b), which confirms the interaction with light in the visible spectrum. The absorbance curve is somewhat broad due to the polydisperse population of AgNP diameters as a small number of larger AgNPs can significantly affect the ensemble light interaction. By eye, the highly concentrated AgNP solution (~ 20 nM) appears opaque green due to the absorbance of blue light, scattering of green light, and weak interaction with red light. This would not typically be considered an ideal substrate for NIR-SEF since the far-field interaction with light near the absorbance and emission spectra of IRDye 800CW (Figure 7.2(b)) is minimal[82, 84-87]. It turns out that a good substrate for NIR-SEF may not need to be in resonance with the fluorophore and there are a number of reasons we believe this to be true. First, while the interaction with light in the NIR region may be relatively weak compared to the visible region, the quality factor is maximized in the NIR (Figure 7.2(b)). The quality factor represents the number of plasmon oscillations, prior to decay, per excitation oscillation. A high quality factor indicates an enhanced local electromagnetic field with relatively low internal dissipative losses[79]. Therefore, quality factor may be an indicator of potential SEF. Second, while visible fluorophores may experience the greatest local electromagnetic field enhancement near AgNPs, the non-local excitation and emission waves are subject to severe attenuation due to the high optical density of the AgNP solution. In contrast, NIR fluorophores have very little far-field attenuation and therefore may be able to more efficiently convert near-field enhancement into measurable SEF. Third, aggregation has been known to broaden and red-shift the resonant frequency of AgNPs by enabling multi-pole plasmon modes[160] and thus increases the interaction with NIR light (Figure 7.2(b)). Aggregation of AgNP has also been shown to generate small, localized, enhanced electromagnetic fields, known as 'hot spots', thereby enabling significant SEF of appropriately located fluorophores[89, 161, 162]. Therefore, a combination of enhanced near-field due to aggregation with low far-field losses and the maximized quality factor makes NIR-SEF with AgNPs in solution a powerful technology.

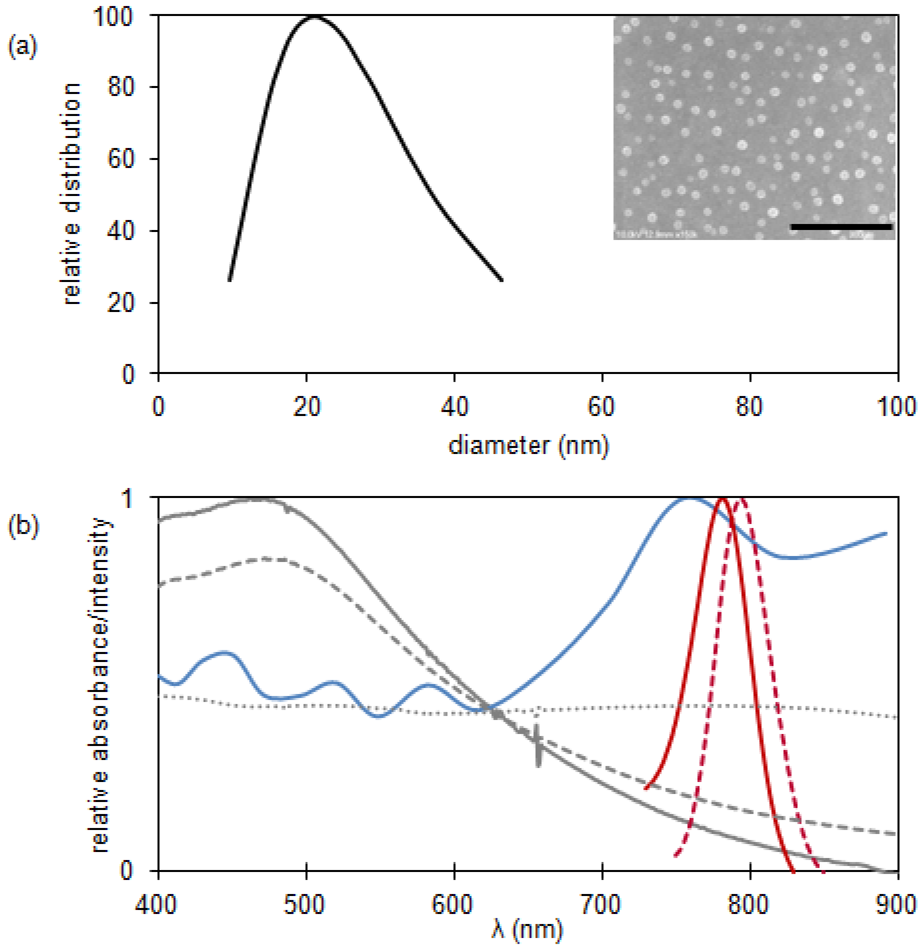

Figure 7.2. Size and spectral characteristics of AgNP. (a) Relative distribution of AgNP size as determined by dynamic light scattering (DLS). The mean diameter was 21 nm. The inset is an SEM image of individual AgNPs used to verify the DLS measurements, the scale bar (black) is 300 nm. (b) Normalized absorbance of AgNP alone (solid gray), AgNP with SAv (dashed gray), and AgNP with SAv and salt (dotted gray) all relative to the maximum absorbance of AgNP alone. Calculated quality factor of AgNPs based on empirical optical properties[35] (solid blue), along with the absorbance (solid red) and emission (dashed red) spectra of IRDye 800CW all scaled relative to their maximum value for qualitative comparison.

Fluorescence emission scans of SAv-800CW in 5 mM NaCl with and without AgNP (Figure 7.3) demonstrate the ability to achieve 300-fold signal enhancement in solution. This demonstrates a larger enhancement than immobilizing the dye on surfaces[88, 89]. We attribute this difference to the ability to locate the fluorophores within and between the aggregating AgNP in solution as opposed to locating on one side of the aggregates on a surface. Further investigation is required to determine the exact mechanism that provides the extra enhancement in solution and is beyond the scope of this study. The inset in Figure 7.3 shows a slight blue-shift in the enhanced emission spectrum compared to the dye alone, which has previously been shown to coincide with an increased radiative decay rate[58]. The ‘knee’ in the curve around 830 nm is thought to be an artifact caused by AgNP-induced scatter which was not completely removed by background subtraction (i.e. AgNP spectrum with unlabeled SAv in salt solution). SEF is known to be the product of enhanced quantum yield and enhanced excitation rate. With an intrinsic quantum yield ~ 0.07, IRDye 800CW has been suggested to gain around 10-fold enhancement due to an improved quantum yield alone[95]. Furthermore, since quantum yield cannot exceed unity the majority of enhancement observed in this study must come from an increased excitation rate.

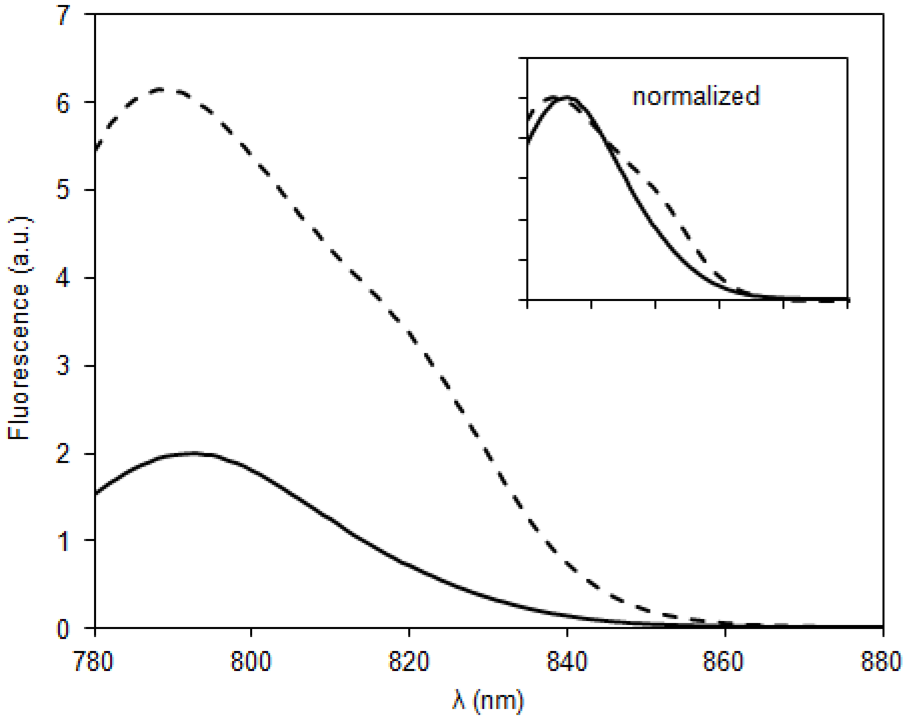

Figure 7.3. Fluorescence emission from 20 nM SAv-800CW (solid line) and SEF emission from 0.2 nM SAv-800CW with 20 nM AgNP (dotted line) after background subtraction, demonstrating ~300-fold enhancement. The inset shows the normalized emission spectra to demonstrate the blue-shift of the peak wavelength from normal fluorescence to SEF.

SEFLISA technology analysis. Translating the advantage of solution-based SEF into a useful assay is not trivial. Typical fluorescence-based assays involve the immobilization of a dye-labeled detection antibody onto a surface. To realize the full potential of SEF, in this case, the SAv-800CW must be remobilized or brought back into solution after immuno-probing. This can be achieved by using a protease to partially digest the immobilized proteins, thus releasing full and partial proteins back into solution. To verify this process a model-system, direct FLISA was conducted using biotinylated bovine serum albumin (b-BSA). Two-fold dilutions of b-BSA from 2000 ng/ml to 200 ng/ml were incubated in a 96-well plate in 0.1% BSA and 0.1X PBS buffer at room temperature for 1 hour. After washing and blocking, SAv-800CW was used to probe the b-BSA. A final wash was followed by 4 differing treatments to the dilution series: (1) no protease and no AgNP, (2) no protease with AgNP, (3) protease and no AgNP, and (4) protease with AgNP. The protease step consisted of adding 50 μl of salt solution with or without protease K and incubating for 30 minutes at room temperature. Protease K was chosen over other proteases due to its promiscuous protein cleaving and temperature stability. It has been experimentally determined that approximately 90% of the SAv-800CW is remobilized after this step without significant cleavage of the SAv itself. Figure 7.4 shows the cleavage efficiency of the protease K solution at the various concentrations of immobilized b-BSA. The asymptotic value is ~ 94%. As expected, the efficiency decreases at very low values of b-BSA where the concentration is insignificant in comparison to the blocking buffer proteins.

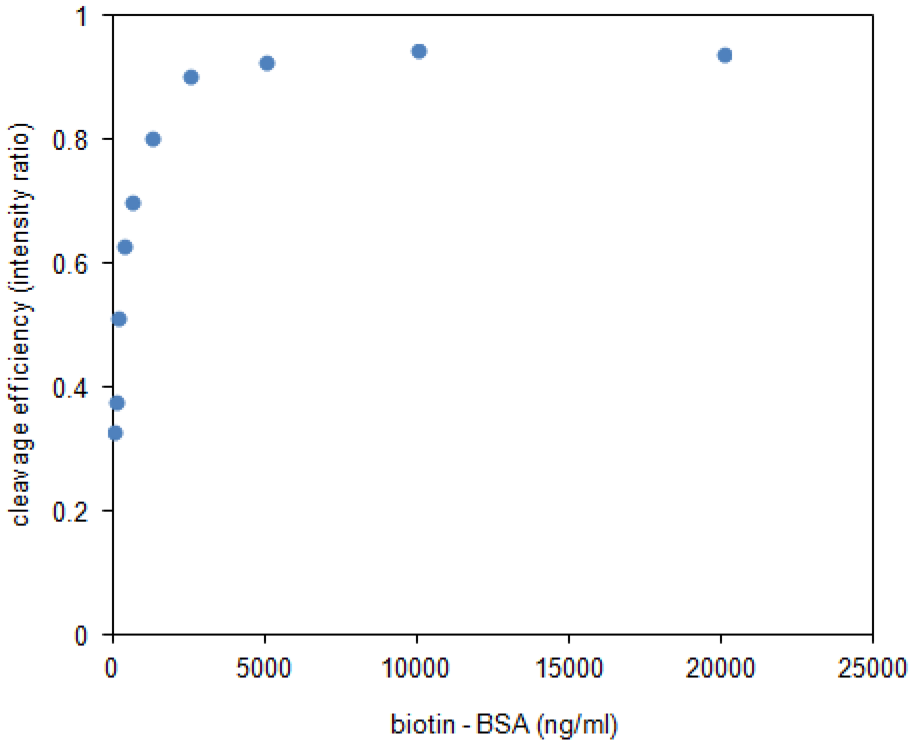

Figure 7.4. Cleavage efficiency of protease K solution at various concentrations of immobilized b-BSA. Cleavage efficiency is defined as the percent of SAv-800CW remobilized after protease K treatment, which was measured as the ratio of fluorescence from wells with protease K divided by the reference wells which contained only dH_2O.

The AgNP treatment consisted of adding 50 µl of AgNP or dH_2O and incubating for 15 minutes on a plate shaker at room temperature. All data points were acquired in quadruplicate with the standard deviations shown in Figure 7.5. The protease K treatment enabled an average enhancement of 166-fold (background subtracted) with a standard deviation of 24, while only 14-fold enhancement with a standard deviation of 1 occurred without the protease. This suggests that the protease K treatment not only remobilizes the SAv-800CW, but also that the remobilization is an important step in realizing the full potential of SEF in this system.

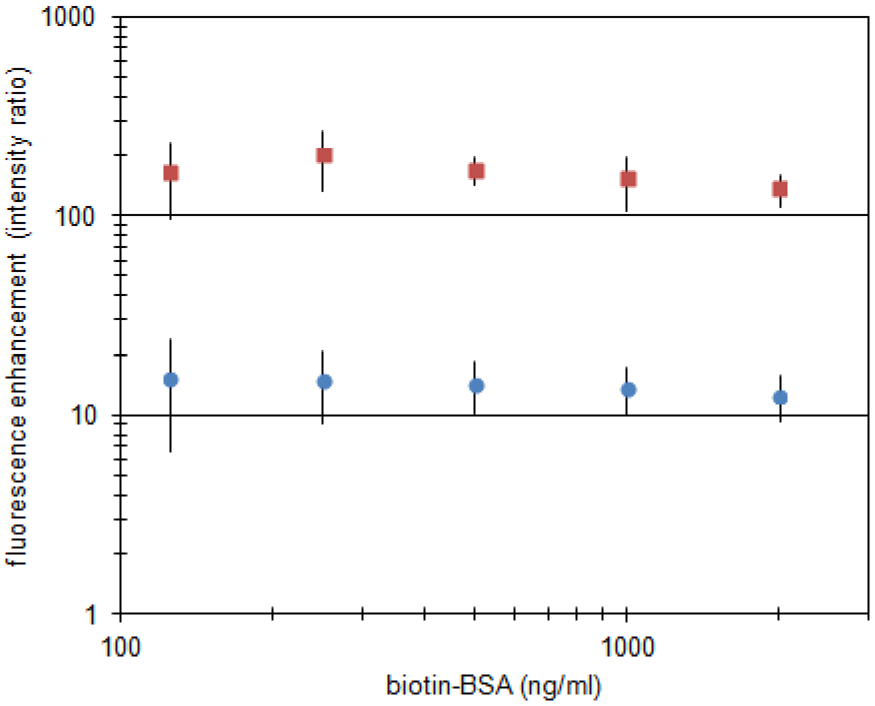

Figure 7.5. Fluorescence enhancement versus concentration of b-BSA with (red squares) and without (blue circles) protease K treatment. Error bars indicate +/- 1 standard deviation at each data point. The protease K treatment enabled an average enhancement of 166-fold across this range of antigen, while the treatment without protease only enabled an average enhancement of 14-fold.

SDS-PAGE was used to determine the form of the SAv-800CW after protease treatment. Specifically, to determine if the protease cleaves the SAv itself and whether or not the SAv becomes immobilized alone or as a complex with antibody attached. Comparing the sample lanes to the SAv-800CW alone (Figure 7.6), it appears that the majority of SAv-800CW is immobilized without remaining attached to antibody. Some fluorescence appears smeared in the size range between 50 and 250 kDa, which is probable due to SAv-800CW remaining attached to various forms of antibody, fragments and whole. The majority of the signal shows up in similar bands as the SAv-800CW reference sample which indicates monomers, dimers, trimers, and tetramers of the SAv-800CW.

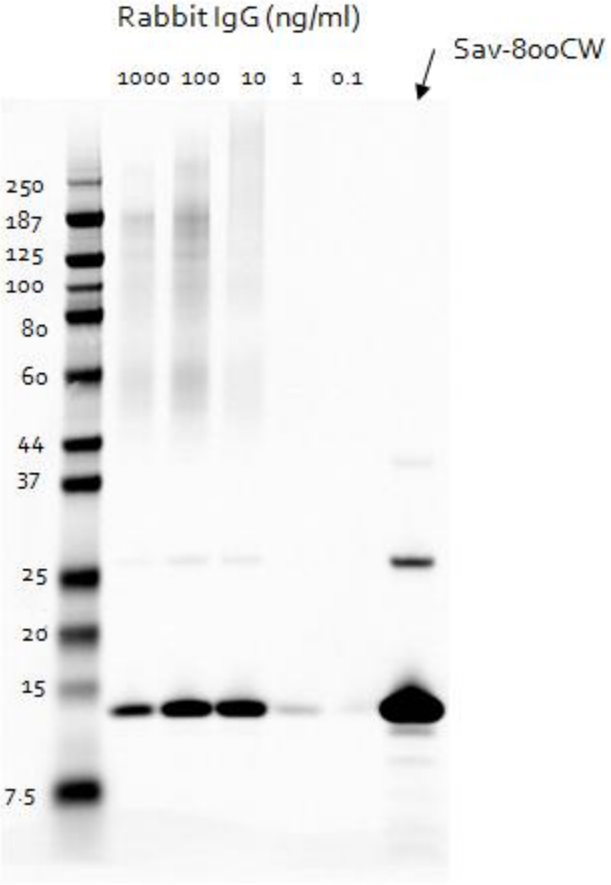

Figure 7.6. Fluorescence image of SDS-PAGE gel showing the distribution of SAv-800CW after protease treatment.

Rabbit IgG direct assay. The SEFLISA technique was then studied using a model-system consisting of rabbit IgG detection in a direct FLISA. There were 4 data points (microtiter plate wells) for each sample dilution which included 2 FLISA and 2 SEFLISA. The data are plotted in Figure 7.7 on linear and logarithmic scales. A linear fit for the FLISA gives a slope of 1.7 x 10^{-3} ml/pg and an offset of 7.6 x 10^{-1}, with an R^2 of 0.97. The SEFLISA has a slope of 1.0 x 10^{-1} ml/pg and an offset of 4.7, with an R^2 of 0.99. By the ratio of the slopes, the SEFLISA is 59-fold more sensitive than the standard FLISA. In this case, we refer to sensitivity as the difference in signal caused by difference in antigen concentration. This sensitivity enhancement enables the assay to detect slight changes in antigen concentration which may be well within the noise for a less sensitive assay technique. LOD lines (3 standard deviations above the mean background) are shown in log format to demonstrate the 8-fold improvement from the empirical 125 pg/ml for standard FLISA down to 15.6 pg/ml for SEFLISA. The limit of quantitation (LOQ), defined as 10 standard deviations above the mean background, is also improved from 143 pg/ml for standard FLISA to 47 pg/ml for SEFLISA. The difference in sensitivity enhancement versus LOD and LOQ enhancement can be attributed to the 6-fold increase in background signal. The background signal increase is probably due to scatter of the excitation light from the AgNP. Due to the small Stokes shift of the dye, the excitation light is not completely filtered prior to detection, which leaves scatter as a potential problem in assay performance. Also, the 6-fold increase is to a very low background due to using NIR fluorescence, therefore, the background remains relatively low. Nonetheless, the assay performance is clearly improved with the SEFLISA technique.

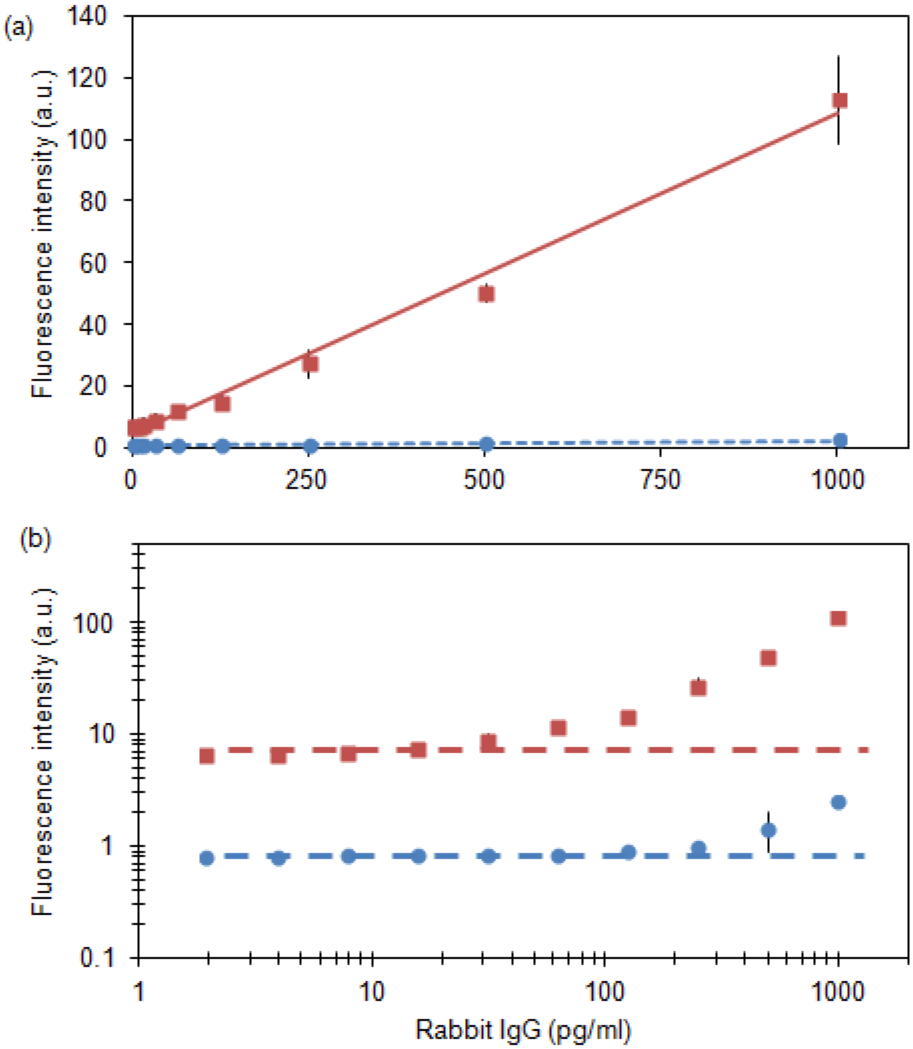

Figure 7.7. Fluorescence intensity versus concentration of rabbit IgG in linear (a) and log (b) format. Error bars indicate +/- 1 standard deviation at each data point. Linear fits were applied to both the standard FLISA (blue) and SEFLISA (red) data sets. The log plot shows the LOD of each data set as dotted lines.

AFP sandwich assay. The SEFLISA technique was then studied on a clinically relevant sandwich assay to detect AFP. In this assay, there were 8 data points for each sample dilution which included 4 standard FLISA and 4 SEFLISA. The data are plotted in Figure 7.8 on linear and logarithmic scales, along with a fluorescence image of the assay plate. A linear fit for the standard FLISA gives a slope of 2.6×10^{-3} ml/pg and an offset of 1.6, with an R^2 of 0.99. The SEFLISA has a slope of 1.1×10^{-1} ml/pg and an offset of 22, with an R^2 of 0.99. The ratio of the slopes is 42 making the SEFLISA 42-fold more sensitive than the standard FLISA. LOD lines are again shown in the log format to demonstrate the 16-fold improvement from 625 pg/ml for standard FLISA down to 39.1 pg/ml for SEFLISA. The 39.1 pg/ml LOD using the SEFLISA technique for AFP is comparable to the typical ELISA LOD of 46 pg/ml[163], while the LOQ is improved from 312 pg/ml for ELISA to 189 pg/ml for SEFLISA. The difference in enhancement between the sensitivity, LOD, and LOQ can once again be attributed to increase in background signal. At 14-fold, the background signal increase is slightly higher in this case which may be due to signal enhancement of non-specific binding. The offset of the standard FLISA for AFP is 2-fold higher than that of the rabbit IgG assay, which further suggests that non-specific binding is likely the cause of the increase in background signal. Notice that the LOD and LOQ of the SEFLISA are much closer in magnitude than those for the ELISA. This is due to the much lower optical background in the NIR fluorescence-based assay.

AFP was employed in this study for its clinical relevance in a variety of diseases. AFP is also an excellent example of a biomarker requiring an assay with a large dynamic range. AFP is produced primarily by the fetal liver and therefore is highest in pregnant women and infants, while being significantly lower in normal adults. The average adult serum level is 3 ng/ml, which is slightly higher in men than in women[164]. During pregnancy, the maternal AFP level elevates to 11 ng/ml at the 8th week of gestation[165] and continues to rise until it peaks at ~ 250 ng/ml around the 32nd week[166]. AFP can be measured in pregnant women, via blood or amniotic fluid, to test for various prenatal development abnormalities[167]. The highest levels of AFP are witnessed at birth where the average infant serum level is 42,000 ng/ml[168] (four orders of magnitude above the average adult level). AFP has also been shown to be a biomarker for hepatocellular carcinoma, a liver cancer[169], where a multi-color assay may be advantageous in order to measure differences in glycosylation[170]. With the large range of clinical levels and differences in glycosylation of AFP, in this case, the SEFLISA technique introduced in this paper, combined with the traditional FLISA, may be a better assay than the traditional ELISA.

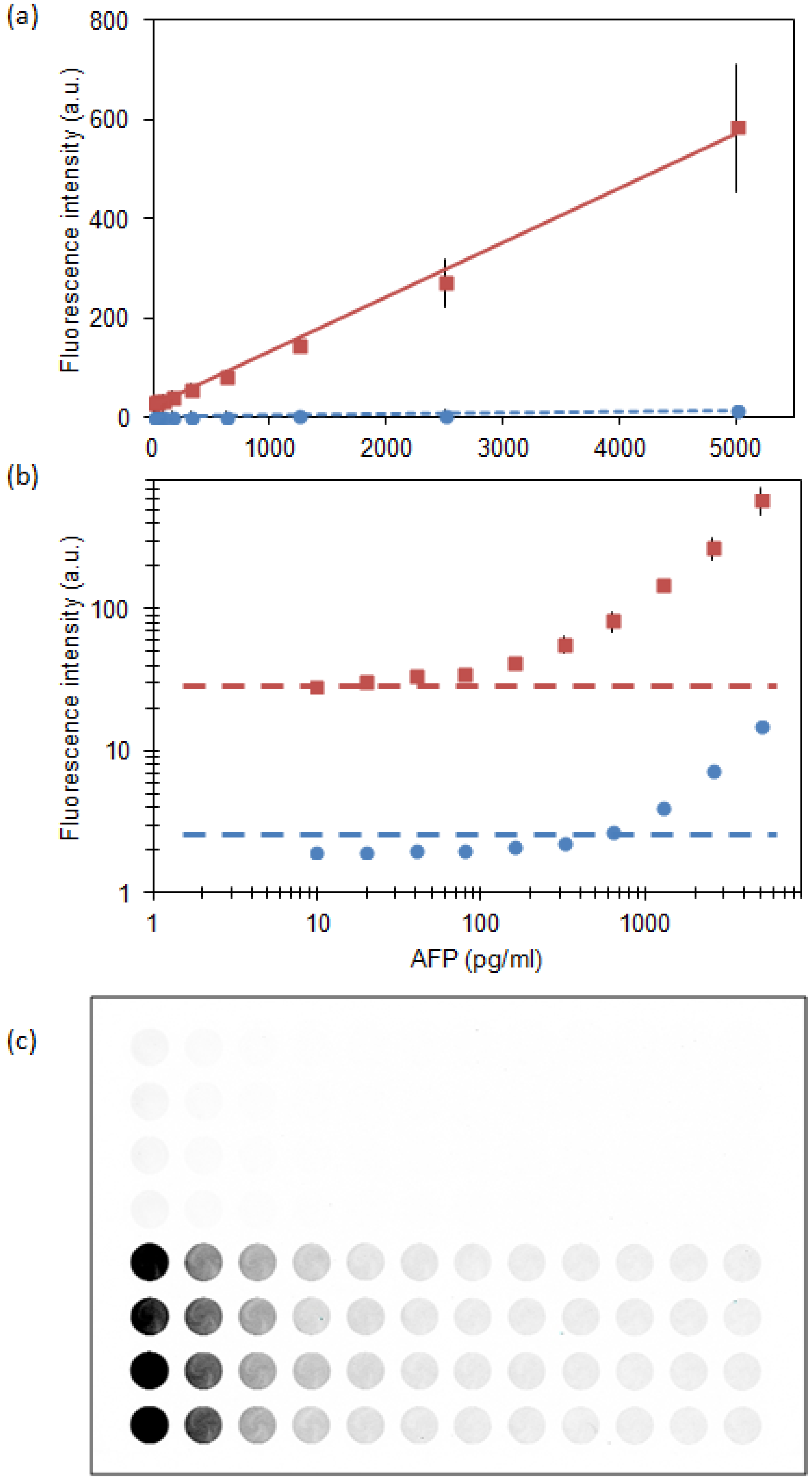
(a)
800
600
400
200
0
Fluorescence intensity (a.u.)
0
1000
2000
3000
4000
5000
(b)
100
10
1
Fluorescence intensity (a.u.)
1
10
100
1000
AFP (pg/ml)
(c)

Figure 7.8. Fluorescence intensity versus concentration of AFP in linear (a) and log (b) format. Error bars indicate +/- 1 standard deviation at each data point. Linear fits were applied to both the standard FLISA (blue) and SEFLISA (red) data sets. The log plot shows the LOD of each data set as dotted lines. Grayscale, fluorescence image of scanned plate (c) for AFP assay. AFP is diluted 2-fold in each column from 5 ng/ml in column 1 to 9.8 pg/ml in column 10. Columns 11 and 12 are background wells. The top 4 rows are the standard, sandwich FLISA while the bottom 4 rows are sandwich SEFLISA.

7.4. CONCLUSIONS

In conclusion, we have introduced a SEFLISA technique that maintains the advantages of FLISA while matching, or surpassing, the sensitivity of ELISA. Further, the technique maintains all of the traditional steps of FLISA while adding two simple steps at the end. A 59-fold enhancement to sensitivity and an 8-fold improvement in LOD were demonstrated on a direct assay using a model system of rabbit IgG. The technique was also tested on a clinically relevant assay to detect AFP, in which a 42-fold enhancement to sensitivity was demonstrated along with a 16-fold improvement in LOD. Both assays demonstrated more favorable enhancement to sensitivity in comparison to LOD and LOQ which is likely due to the increase in background from excitation scatter.

This SEFLISA technique has been demonstrated to be potentially superior to ELISA for detecting AFP. We anticipate this to be the case for other antigens of interest as well. Further research will focus on multiplexing the technique for multiple antigen detection, or measuring differences in post-translational modification. Also, we expect to be able to improve the assay performance since the enhancement is far from the empirical limit (Chapter 6). Further research will be required to determine the limitations and optimize adjustments to the current protocol to realize further sensitivity improvement.

CHAPTER 8. CONCLUSIONS

8.1. REVIEW OF GOALS AND RESULTS

The overall goal of this work was to determine the extent to which fluorescence in solution may be enhanced by altering specific variables involved in the process, such as wavelength, carrier protein, AgNP concentration, and salt concentration, with the intent of providing a simple solution that may be readily adopted by current fluorescence users in the life science research community. This goal has been achieved by designing and completing a series of experiments to test formulated hypotheses and reporting the results in the form of peer-reviewed publications, including this dissertation.

Theoretical analysis along with experimental data tested the hypotheses that (1) inner-filtering may red-shift the optimal fluorophore spectrum away from the resonant frequency of the plasmon-active nanostructure and (2) that in some cases, the quality factor may be a more important predictor of SEF as opposed to the nanostructure resonance indicated by the absorbance spectra (Chapter 3). The data agree with both hypotheses when a concentrated solution of AgNP is used causing significant inner-filtering near the resonant frequency and allowing aggregation to enable SEF in the NIR where the quality factor is maximized.

The hypothesis that the physical size and shape of carrier proteins play an important role in the ability to enhance the fluorescent signal from the fluorophores they carry when combined with AgNP in solution was tested in multiple ways (Chapter 4). The effect of protein size on distance between AgNP and thus electromagnetic field intensity was studied using BEM simulations. The effect of protein size on the number of bound AgNP was experimentally studied by measuring aggregation at various protein/AgNP ratios by changes in absorbance. The effect of protein shape on possible AgNP-fluorophore orientations was qualitatively discussed based on geometric limitations. Finally, the effects were studied in combination by measuring fluorescence enhancement with dye-labeled SAv, F(ab')$_2$, and IgG. Each protein demonstrated the ability to enhance fluorescence, maintain a linear relationship with signal versus concentration, and ultimately improve the LOD. SAv was determined to be the best choice for carrier protein due to its ability to generate the largest (on the order of 1000-fold) enhancement with the smallest variance.

The effect of aggregation on SEF in solution was studied through controlled mixing in a digital, microfluidic device (Chapter 5). Specifically, a liquid-liquid droplet micromixer in a disposable poly(methyl methacrylate) (PMMA) microchip was used to study the effects of salt concentration, colloid concentration, and mixing efficiency on SEF of a NIR fluorophore with aggregated AgNP using conventional fluorescence microscopy. It was found that an optimal salt concentration could be identified. The effect of colloid concentration and mixing efficiency remained unbounded as both demonstrated maximum SEF at the highest tested values. This study was the first demonstration in the literature, to the authors' knowledge, of SEF in a microfluidic format.

Next, NIR-SEF was investigated in the more common assay format of a microtiter plate with the intention of benefiting current fluorescence users. Through optimization of salt concentration, it was demonstrated that a NIR-SEF technique can enhance the signal of SAv-800CW up to 2530-fold while improving the LOD over 1000-fold (Chapter 6). Importantly, the technique uses simple-to-fabricate, citrate-stabilized AgNPs in solution in contrast to other studies that require expensive and complicated manufacturing processes to create delicate surfaces that achieve similar results.

Finally, a NIR-SEFLISA technique was introduced and interpreted, in terms of the results acquired throughout this dissertation, to use the NIR-SEF technology in a real-world application. A 42-fold improvement in sensitivity for the clinically-relevant biomarker AFP was demonstrated, along with a 16-fold improvement in LOD. This assay demonstrates the ability to apply the NIR-SEF technique in ways that may benefit other research and medical fields.

8.2. RECOMMENDATIONS FOR FUTURE RESEARCH

For every answer or experimental result many questions arise. This dissertation contributes to the overall understanding of SEF and particularly NIR-SEF using citrate-stabilized AgNP in solution. The following are recommendations for future research that may advance the understanding even further:

i. It has been determined in this work that the pH of the AgNP solution is extremely important in controlling the interaction between the individual AgNPs and proteins (Appendix C). In fact, no enhancement of fluorescence signal was detected using off-the-shelf AgNPs in the same procedures used in this dissertation. Preliminary results show that the off-the-shelf AgNP solutions have a pH ≈ 7, while the AgNP solution used in this work is pH ≈ 4. It is hypothesized that the pH directly affects the AgNP-protein interaction by (1) changing the overall charge on the protein, which can attract or repel it from the AgNP (depending on the pH of the solution and the pI of the protein), (2) changing the zeta potential of the AgNPs by protonating/de-protonating the citrate molecules on the surface, (3) reducing or increasing the steric hindrance caused by the citrate molecules by affecting the equilibrium concentration on the surfaces of the AgNP, and (4) a combination of all the above mentioned factors. An attempt was made to simply adjust the AgNP solution pH and then conduct absorbance and SEF measurements; however, adjustment of the AgNP solution pH may have caused additional effects not accounted for such as particle stability and changes in size distribution. A careful study involving the pH adjustment of AgNP solution should be reattempted with confirmation that particle size distribution remains unaffected. In addition, in the future zeta potential measurements will be valuable to determine any change in the surface charge associated with the AgNP. Another approach, avoiding the challenges associated with pH changes to the AgNP solution, would be to study protein binding on Ag (and Au) surfaces using the surface plasmon resonance (SPR) technique[171, 172]. SPR studies are conducted by measuring the reflection of laser illumination incident at various angles relative to a thin metal film. The reflection intensity at a given angle and the angle of maximum reflection change with the local index of refraction near the surface, which is related to the concentration of bound biomolecules. One could then change the citrate concentration, pH, salt concentration etc. and measure the change in protein interaction with the metal surface. If successful, this experiment could be repeated for various proteins/biomolecules, as well as various capping agents on the metal surface (e.g. PVP, tannic acid, etc.). Further insight can be obtained from related research on NP-protein interactions[173-176] and NP functionalization techniques[177, 178].

ii. Clearly aggregation of AgNP is one successful strategy for fabricating plasmon-active nanostructures to enable NIR-SEF (Chapters 5 and 6). The related technology of SERS (described in Chapter 2) has also been shown to benefit from similar nanostructure formations. No known combination study has been conducted where SEF and SERS are measured simultaneously on the same nanostructures. This combined study would enable the empirical separation of the electric field enhancement from the quantum yield enhancement, as SERS relies strictly on field enhancement. More specifically, SERS is proportional to $|E/E_0|^4$ while SEF is proportional to $|E/E_0|^2$ and q/q_0. The separation of these two components in the overall enhancement is needed to confirm theoretical predictions with empirical data. Studies involving single-molecule measurements would also be useful for statistical analysis of the processes in discrete spots instead of ensemble measurements. It may be the case that a few ‘hot-spots’ are responsible for the majority of the ensemble signal enhancement, as has been shown for SERS[54]. This research could be accomplished with an optical detection set-up, such as a microscope, where fluorescence and Raman spectra can be obtained from the same location on a sample immobilized on a surface. The plasmon-active nanostructures could be aggregated AgNP, as in this dissertation; however, a better choice would be nanoparticles in arrays on a surface with deliberate periodicity for easier location mapping and comparison to simulated electromagnetic fields[179-183]. This study would require collaboration with other researchers who have created such surfaces, or development of the technique locally.

iii. Recently, it has been suggested that the intentional design of nanoantennas in the form of dimers of mNPs may be significantly more efficient than random aggregation for enhancing Raman signals[184]. A similar hypothesis could be formed for fluorescence. It would be very useful to first solve for an analytical solution, if possible, or a semi-empirical solution of the SEF process between a symmetric dimer of Ag- or AuNPs. Currently, Mie theory along with numerical techniques must be used to accomplish the task even though SEF can be calculated near a monomer with simple equations[154]. One could then determine the optimal design for a specific fluorophore followed by experimental verification. Recent progress towards this goal has been demonstrated by modeling the hot-spot between two mNPs as a superposition of hot-spots located on the surface of each mNP[47]. It was determined that simple, spherical mNPs may generate larger local electromagnetic field enhancement than more complicated geometries; however, a solution to mathematically represent the simplified case was not presented. Further, incorporation of the dipole emitter will require changes to the model. Ultimately, the suggested research may enable the design of a super-bright fluorescent probe for immunoassays with 10,000-fold enhancement or better, similar to attempts involving SERS[185-187].

iv. It is now widely accepted that the SEF process is comprised of an enhancement to the electric field along with an improved quantum yield of the emitter. It has also been shown that an improved quantum yield (radiative decay rate) can be accompanied with a shorter Stokes-shift (Chapter 6). It was hypothesized that the amount of Stokes-shift reduction may be positively correlated with the improvement in quantum yield. The reasoning is that a blue-shift in the emission spectra may be indicative of improved efficiency in the process (i.e. less loss to the surrounding environment). A quick experiment did not demonstrate this effect. Further research is warranted as this aspect of the SEF process is poorly understood. This study could be accomplished by using a simple, plasmon-active substrate, such as SIF or AgNP on a surface, to measure the change in decay rate of multiple fluorophores with similar spectral properties but differing intrinsic quantum yield. This acquisition of this data would require a fluorescence detection system with time-resolved capability. The experiment could be repeated with fluorophores on different substrates, or varying distance from the substrate, to determine if the trend remains the same. The research may have implications in optical design when using SEF, as the optimal emission filter(s) could differ from those without the blue-shifted emission. The blue-shift may also counteract the enhancement in signal by reducing the collection efficiency of the emitted light due to a smaller Stokes-shift.

v. The NIR-SEFLISA assay presented (Chapter 7) may be improved with further development. The 59-fold improvement in sensitivity is well below the empirical limit of over 2000-fold improvement (Chapter 6). This gap should be closed with further exploration. One research activity could involve the design of a linker to the SAv-800CW molecule that can be specifically cleaved so that non-specific antibodies and fragments are not in direct competition for the surface area on the AgNP in solution. First, one should determine whether the extra proteins and fragments in solution are troublesome. This investigation could be accomplished by measuring the fluorescence enhancement of SAv-800CW in solution with AgNP in the presence of various concentrations of proteins and fragments differing in size and composition. The study could include all proteins present in the NIR-SEFLISA assay; however, the blocking buffer itself contains a large number of proteins so this would be impractical. The study should probably include proteins of various size and pI as both would likely have an impact on the results. Additionally, the difference in potential sensitivity (Chapter 6) and current sensitivity (Chapter 7) could also be due to the microplate surface being coated with protein. The proteins may reduce the concentration of AgNP in solution and/or adversely affect the background signal due to AgNP binding on the surface. This potential effect could be verified by measuring the background signal of AgNP with and without proteins on the surface of the microtiter plate. If either of the aforementioned problems exist, the use of a specifically, cleavable linker would likely improve assay performance. If the proteins on the surface are determined to be problematic, the cleaved SAv-800CW could be transferred to a fresh microtiter plate via centrifugation. Commercially available cleavable linkers include disulfide bonds that can be cleaved with reducing agents, such as dithiothreitol (DTT), β-mercaptoethanol (BME), or tris(2-carboxyethyl)phosphine (TCEP), as well as UV-cleavable linkers. While these linkers would be convenient, they may generate adverse reactions to the AgNP due to the reducing agents, or the UV exposure may destroy the fluorophores. Another option would be to design a DNA/RNA linker that can be cleaved with a nuclease. The chosen nuclease should be efficient in order to require a small concentration to accomplish the cleavage. Ideally, specific release of the bound SAv-800CW would create an environment, much like in Chapter 6, where over 1000-fold improvement in LOD was demonstrated.

In summary, this dissertation contributes to the overall understanding of the SEF process, particularly NIR-SEF using AgNP in solution. It has been demonstrated that substantial enhancement to fluorescence signal and improved LOD of IRDye 800CW can be achieved using a labeled carrier protein with citrate-stabilized AgNP in solution. This work may enable the adoption of NIR-SEF by researchers outside of the plasmonic community to improve sensitivity and LOD of bioassays used in medical research and diagnostics. Recommendations for future research are made to further advance the understanding of the physical mechanisms involved in SEF.

REFERENCES

(1) Lakowicz, J. R., *Principles of fluorescence spectroscopy*. 3rd ed.; Springer: New York, 2006.

(2) Burnette, W. N. “Western Blotting”: Electrophoretic transfer of proteins from sodium dodecyl sulfate-polyacrylamide gels to unmodified nitrocellulose and radiographic detection with antibody and radioiodinated protein A. *Analytical Biochemistry* **1981,** 112, 195-203.

(3) Dalessio, J.; Ashley, R. Highly sensitive enhanced chemiluminescence immunodetection method for herpes simplex virus type 2 Western immunoblot. *Journal of Clinical Microbiology* **1992,** 30, 1005-1007.

(4) Gingrich, J. C.; Davis, D. R.; Nguyen, Q. Multiplex detection and quantitation of proteins on western blots using fluorescent probes. *Biotechniques* **2000,** 29, 636-642.

(5) Fradelizi, J.; Friederich, E.; Beckerle, M. C.; Golsteyn, R. M. Quantitative measurement of proteins by western blotting with Cy5-coupled secondary antibodies. *Biotechniques* **1999,** 26, 484-486, 488, 490.

(6) Jia, C.-P.; Zhong, X.-Q.; Hua, B.; Liu, M.-Y.; Jing, F.-X.; Lou, X.-H.; Yao, S.-H.; Xiang, J.-Q.; Jin, Q.-H.; Zhao, J.-L. Nano-ELISA for highly sensitive protein detection. *Biosensors and Bioelectronics* **2009,** 24, 2836-2841.

(7) Swartzman, E. E.; Miraglia, S. J.; Mellentin-Michelotti, J.; Evangelista, L.; Yuan, P.-M. A homogeneous and multiplexed immunoassay for high-throughput screening using fluorometric microvolume assay technology. *Analytical Biochemistry* **1999,** 271, 143-151.

(8) Giepmans, B. N. G.; Adams, S. R.; Ellisman, M. H.; Tsien, R. Y. The fluorescent toolbox for assessing protein location and function. *Science* **2006,** 312, 217-224.

(9) Tsurui, H.; Nishimura, H.; Hattori, S.; Hirose, S.; Okumura, K.; Shirai, T. Seven-color fluorescence imaging of tissue samples based on Fourier

spectroscopy and singular value decomposition. *Journal of Histochemistry and Cytochemistry* **2000,** 48, 653-662.

(10) Ntziachristos, V. Fluorescence molecular imaging. *Annual Review of Biomedical Engineering* **2006,** 8, 1-33.

(11) van Dam, G. M.; Themelis, G.; Crane, L. M. A.; Harlaar, N. J.; Pleijhuis, R. G.; Kelder, W.; Sarantopoulos, A.; de Jong, J. S.; Arts, H. J. G.; van der Zee, A. G. J.; Bart, J.; Low, P. S.; Ntziachristos, V. Intraoperative tumor-specific fluorescence imaging in ovarian cancer by folate receptor-α targeting: first in-human results. *Nature Medicine* **2011,** 17, 1315-1319.

(12) Wulfkuhle, J. D.; Liotta, L. A.; Petricoin, I., Emanuel F. Proteomic applications for the early detection of cancer. *Nature Reviews Cancer* **2003,** 3, 267-275.

(13) Haab, B. B. Antibody arrays in cancer research. *Molecular & Cellular Proteomics* **2005,** 4, 377-383.

(14) Sanchez-Carbayo, M. Antibody arrays: technical considerations and clinical applications in cancer. *Clinical Chemistry* **2006,** 52, 1651-1659.

(15) Hanash, S. Disease proteomics. *Nature* **2003,** 422, 226-232.

(16) Sahab, Z. J.; Semaan, S. M.; Sang, Q.-X. A. Methodology and applications of disease biomarker identification in human serum. *Biomarker Insights* **2007,** 2, 21-43.

(17) Comunale, M. A.; Rodemich-Betesh, L.; Hafner, J.; Wang, M.; Norton, P.; Di Bisceglie, A. M.; Block, T.; Mehta, A. Linkage specific fucosylation of alpha-1-antitrypsin in liver cirrhosis and cancer patients: implications for a biomarker of hepatocellular carcinoma. *PLoS One* [Online] **2012**, 5, e12419, 10.1371/journal.pone.0012419

(18) Negm, R. S.; Verma, M.; Srivastava, S. The promise of biomarkers in cancer screening and detection. *Trends in Molecular Medicine* **2002,** 8, 288-293.

(19) Etzioni, R.; Urban, N.; Ramsey, S.; McIntosh, M.; Schwartz, S.; Reid, B.; Radich, J.; Anderson, G.; Hartwell, L. Early detection: The case for early detection. *Nature Reviews Cancer* **2003,** 3, 243-252.

(20) Savage, N. Early detection: Spotting the first signs. *Nature* **2011,** 471, S14-S15.

(21) Faca, V.; Krasnoselsky, A.; Hanash, S. Innovative proteomic approaches for cancer biomarker discovery. *Biotechniques* **2007,** 43, 279-283.

(22) Liang, S.-L.; Chan, D. W. Enzymes and related proteins as cancer biomarkers: A proteomic approach. *Clinica Chimica Acta* **2007,** 381, 93-97.

(23) Landegren, U. D.; Vanelid, J.; Hammond, M.; Nong, R. Y.; Wu, D.; Ulleras, E.; Kamali-Moghaddam, M. Opportunities for sensitive plasma proteome analysis. *Analytical Chemistry* **2012,** 84, 1824-1830.

(24) Gilijohann, D. A.; Mirkin, C. A. Drivers of biodiagnostic development. *Nature* **2009,** 462, 461-464.

(25) Georganopoulou, D. G.; Chang, L.; Nam, J.-M.; Thaxton, C. S.; Mufson, E. J.; Klein, W. L.; Mirkin, C. A. Nanoparticle-based detection in cerebral spinal fluid of a soluble pathogenic biomarker for Alzheimer's disease. *Proceedings of the National Academy of Sciences* **2005,** 102, 2273-2276.

(26) Middendorf, L. R.; Amen, J.; Bruce, R. C.; Draney, D.; DeGraff, D.; Gewecke, J.; Grone, D. L.; Humphrey, P.; Little, G.; Lugade, A.; Narayanan, N.; Oommen, A.; Osterman, H.; Peterson, R.; Rada, J.; Raghavachari, R.; Roemer, S. C., Near-infrared fluorescence instrumentation for DNA analysis. In *Near-Infrared Dyes for High Technology Applications*, Daehne, S.; Resch-Genger, U.; Wolfbeis, O. S., Eds. Kluwer Academic Publishers: Dordrecht, The Netherlands, 1998, Vol. 52, pp 21-53.

(27) Piruska, A.; Nikcevic, I.; Lee, S. H.; Ahn, C. H.; Heineman, W. R.; Limbach, P. A.; Seliskar, C. J. The autofluorescence of plastic materials and chips measured under laser irradiation. *Lab on a Chip* **2005,** 5, 1348-1354.

(28) Hong, G.; Tabakman, S. M.; Welsher, K.; Chen, Z.; Robinson, J. T.; Wang, H.; Zhang, B.; Dai, H. Near-infrared-fluorescence-enhanced molecular imaging of

live cells on gold substrates. *Angewandte Chemie International Edition* **2011,** 50, 4644-4648.

(29) Jablonski, A. Efficiency of anti-Stokes fluorescence in dyes. *Nature* **1933,** 131, 839-840.

(30) Piruska, A.; Nikcevic, I.; Lee, S. H.; Ahn, C.; Heineman, W. R.; Limbach, P. A.; Seliskar, C. J. The autofluorescence of plastic materials and chips measured under laser irradiation. *Lab on a Chip* **2005,** 5, 1348-1354.

(31) Frangioni, J. V. *In vivo* near-infrared fluorescence imaging. *Current Opinion in Chemical Biology* **2003,** 7, 626-634.

(32) Schebarchov, D.; Auguie, B.; Le Ru, E. C. Simple accurate approximations for the optical properties of metallic nanospheres and nanoshells. *Physical Chemistry Chemical Physics* **2013,** 15, 4233-4242.

(33) Rakic, A. D.; Djurisic, A. B.; Elazar, J. M.; Majewski, M. L. Optical properties of metallic films for vertical-cavity optoelectronic devices. *Applied Optics* **1998,** 37, 5271-5283.

(34) Vial, A.; Grimault, A.-S.; Macias, D.; Barchiesi, D.; de la Chapelle, M. L. Improved analytical fit of gold dispersion: application to the modeling of extinction spectra with a finite-difference time-domain method. *Physical Review B* **2005,** 71, 085416.

(35) Johnson, P. B.; Christy, R. W. Optical constants of the noble metals. *Physical Review B* **1972,** 6, 4370-4379.

(36) Kinkhabwala, A.; Yu, Z.; Fan, S.; Avlasevich, Y.; Mullen, K.; Moerner, W. E. Large single-molecule fluorescence enhancements produced by a bowtie nanoantenna. *Nature Photonics* **2009,** 3, 654-657.

(37) Boriskina, S. V.; Dal Negro, L. Multiple-wavelength plasmonic nanoantennas. *Optics Letters* **2010,** 35, 538-540.

(38) Giannini, V.; Fernandez-Dominguez, A. I.; Heck, S. C.; Maier, S. A. Plasmonic nanoantennas: fundamentals and their use in controlling the radiative properties of nanoemitters. *Chemical Reviews* **2011,** 111, 3888-3912.

(39) Liu, N.; Tang, M. L.; Hentschel, M.; Giessen, H.; Alivisatos, A. P. Nanoantenna-enhanced gas sensing in a single tailored nanofocus. *Nature Materials* **2011,** 10, 631-636.

(40) Busson, M. P.; Rolly, B.; Stout, B.; Bonod, N.; Bidault, S. Accelerated single photon emission from dye molecule-driven nanoantennas assembled on DNA. *Nature Communications* **2012,** 3, 1-6.

(41) Punj, D.; Mivelle, M.; Moparthi, S. B.; Van Zanten, T. S.; Rigneault, H.; van Hulst, N. F.; Garcia-Parajo, M. F.; Wenger, J. A plasmonic 'antenna-in-box' platform for enhanced single-molecule analysis at micromolar concentrations. *Nature Nanotechnology* **2013,** 8, 512-516.

(42) Qin, L.; Zou, S.; Xue, C.; Atkinson, A. L.; Schatz, G. C.; Mirkin, C. A. Designing, fabricating, and imaging Raman hot spots. *Proceedings of the National Academy of Sciences* **2006,** 103, 13300-12303.

(43) Bek, A.; Jansen, R.; Ringler, M.; Mayilo, S.; Klar, T. A.; Feldmann, J. Fluorescence enhancement in hot spots of AFM-designed gold nanoparticle sandwiches. *Nano Letters* **2008,** 8, 485-490.

(44) Litz, J. P.; Camden, J. P.; Masiello, D. J. Spatial, Spectral, and Coherence Mapping of Single-Molecule SERS Active Hot Spots via the Discrete-Dipole Approximation. *The Journal of Physical Chemistry Letters* **2011,** 2, 1695-1700.

(45) Willets, K. A.; Stranahan, S. M.; Weber, M. L. Shedding light on surface-enhanced Raman scattering hot spots through single-molecule super-resolution imaging. *The Journal of Physical Chemistry Letters* **2012,** 3, 1286-1294.

(46) Borys, N. J.; Shafran, E.; Lupton, J. M. Surface plasmon delocalization in silver nanoparticle aggregates revealed by subdiffraction supercontinuum hot spots. *Scientific Reports* **2013,** 3, 2090.

(47) Perassi, E. M.; Coronado, E. A. The Structure, Energy, Confinement, and Enhancement of Hot Spots between Two Nanoparticles. *The Journal of Physical Chemistry C* **2013,** 117, 7744-7750.

(48) Novotny, L.; van Hulst, N. Antennas for light. *Nature Photonics* **2011,** 5, 83-90.

(49) Strutt), L. R. J. W. On the light from the sky, its polarization and colour. *Philosophical Magazine* **1871,** 41, 107-120, 274-279.

(50) Strutt), L. R. J. W. On the transmission of light through an atmosphere containing small particles in suspension and on the origin of the blue of the sky. *Philosophical Magazine* **1899,** 47, 375-384.

(51) Mie, G. Beitrage zur Optik truber Medien, speziell kolloidaler Metallosungen. *Annalen der Physik* **1908,** 330, 377-445.

(52) Purcell, E. M. Spontaneous emission probabilities at radio frequencies. *Physical Review* **1946,** 69, 681.

(53) Kleppner, D. Inhibited spontaneous emission. *Physical Review Letters* **1981,** 47, 233-236.

(54) Nie, S. Probing Single Molecules and Single Nanoparticles by Surface-Enhanced Raman Scattering. *Science* **1997,** 275, 1102-1106.

(55) Kneipp, K.; Wang, Y.; Kneipp, H.; Perelman, L. T.; Itzkan, I.; Dasari, R. R.; Feld, M. S. Single molecule detection using surface-enhanced Raman scattering (SERS). *Physical Review Letters* **1997,** 78, 1667-1670.

(56) Barnes, W. L. Fluorescence near interfaces: The role of photonic mode density. *Journal of Modern Optics* **1998,** 45, 661-699.

(57) Lakowicz; J. Radiative Decay Engineering: Biophysical and Biomedical Applications. *Analytical Biochemistry* **2001,** 298, 1-24.

(58) Lakowicz; J. Radiative Decay Engineering 2. Effects of Silver Island Films on Fluorescence Intensity, Lifetimes, and Resonance Energy Transfer. *Analytical Biochemistry* **2002,** 301, 261-277.

(59) Lakowicz; J. Radiative decay engineering 3. Surface plasmon-coupled directional emission. *Analytical Biochemistry* **2004,** 324, 153-169.

(60) Gryczynski; I. Radiative decay engineering 4. Experimental studies of surface plasmon-coupled directional emission. *Analytical Biochemistry* **2004,** 324, 170-182.

(61) Lakowicz, J. R. Radiative decay engineering 5: metal-enhanced fluorescence and plasmon emission. *Analytical Biochemistry* **2005,** 337, 171-194.

(62) Fort, E.; Grésillon, S. Surface enhanced fluorescence. *Journal of Physics D: Applied Physics* **2008,** 41, 013001.

(63) Zhang, J.; Lakowicz, J. R. Metal-enhanced fluorescence of an organic fluorophore using gold particles. *Optics Express* **2007,** 15, 2598-2606.

(64) Zhang, J.; Fu, Y.; Chowdhury, M. H.; Lakowicz, J. R. Metal-enhanced single-molecule fluorescence on silver particle monomer and dimer: coupling effect between metal particles. *Nano Letters* **2007,** 7, 2101-2107.

(65) Zhang, J.; Lakowicz, J. R. A model for DNA detection by metal-enhanced fluorescence from immobilized silver nanoparticles on solid substrate. *Journal of Physical Chemistry B* **2006,** 110, 2387-2392.

(66) Wei, X.; Li, H.; Li, Z.; Vuki, M.; Fan, Y.; Zhong, W.; Xu, D. Metal-enhanced fluorescent probes based on silver nanoparticles and its application in IgE detection. *Analytical and Bioanalytical Chemistry* **2012,** 402, 1057-1063.

(67) Tang, F.; Ma, N.; Tong, L.; He, F.; Li, L. Control of metal-enhanced fluorescence with pH- and thermoresponsive hybrid microgels. *Langmuir* **2012,** 28, 883-888.

(68) Nooney, R.; Clifford, A.; LeGuevel, X.; Stranik, O.; McDonagh, C.; MacCraith, B. D. Enhancing the analytical performance of immunoassays that employ metal-enhanced fluorescence. *Analytical and Bioanalytical Chemistry* **2010,** 396, 1127-1134.

(69) Aslan, K.; Gryczynski, I.; Malicka, J.; Matveeva, E.; Lakowicz, J.; Geddes, C. Metal-enhanced fluorescence: an emerging tool in biotechnology. *Current Opinion in Biotechnology* **2005,** 16, 55-62.

(70) Choudhury, S. D.; Badugu, R.; Ray, K.; Lakowicz, J. R. Silver-gold nanocomposite substrates for metal-enhanced fluorescence: ensemble and single-molecule spectroscopic studies. *Journal of Physical Chemistry C* **2012,** 116, 5042-5048.

(71) Geddes, C. D.; Gryczynski, I.; Malicka, J.; Gryczynski, Z.; Lakowicz, J. R. Metal-Enhanced Fluorescence: Potential Applications in HTS. *Combinatorial Chemistry and High Throughput Screening* **2003,** 6, 109-117.

(72) Geddes, C. D.; Parfenov, A.; Roll, D.; Gryczynski, I.; Malicka, J.; Lakowicz, J. R. Silver fractal-like structures for metal-enhanced fluorescence: enhanced fluorescence intensities and increased probe photostabilities. *Journal of Fluorescence* **2003,** 13, 267-276.

(73) Deng, W.; Goldys, E. M. Plasmonic approach to enhanced fluorescence for applications in biotechnology and the life sciences. *Langmuir* **2012,** 28, 10152-10163.

(74) Ming, T.; Chen, H.; Jiang, R.; Li, Q.; Wang, J. Plasmon-controlled fluorescence: beyond the intensity enhancement. *Journal of Physical Chemistry Letters* **2012,** 3, 191-202.

(75) Aroca, R. F. Plasmon enhanced spectroscopy. *Physical Chemistry Chemical Physics* **2013,** 15, 5355-5363.

(76) Geddes, C. D.; Lakowicz, J. R., *Radiative Decay Engineering*. Springer Science + Business Media, Inc.: New York, 2005; Vol. 8, p 457.

(77) Geddes, C. D., *Metal-Enhanced Fluorescence*. John Wiley & Sons, Inc.: Hoboken, New Jersey, 2010.

(78) Bharadwaj, P.; Deutsch, B.; Novotny, L. Optical antennas. *Advances in Optics and Photonics* **2009,** 1, 438-483.

(79) Stockman, M. I. Nanoplasmonics: past, present, and glimpse into future. *Optics Express* **2011,** 19, 22029-22106.

(80) Bharadwaj, P.; Anger, P.; Novotny, L. Nanoplasmonic enhancement of single-molecule fluorescence. *Nanotechnology* **2007,** 18, 044017.

(81) Lakowicz, J. R.; Malicka, J.; Gryczynski, I.; Gryczynski, Z.; Geddes, C. D. Radiative decay engineering: the role of photonic mode density in biotechnology. *Journal of Physics D: Applied Physics* **2003,** 36, R240-R249.

(82) Zhao, L.; Ming, T.; Chen, H.; Liang, Y.; Wang, J. Plasmon-induced modulation of the emission spectra of the fluorescent molecules near gold nanorods. *Nanoscale* **2011,** 3, 3849-3859.

(83) Maier, S. A., *Plasmonics : fundamentals and applications*. Springer: New York, 2007.

(84) Bharadwaj, P.; Beams, R.; Novotny, L. Nanoscale spectroscopy with optical antennas. *Chemical Science* **2011,** 2, 136-140.

(85) Chen, Y.; Munechika, K.; Ginger, D. S. Dependence of fluorescence intensity on the spectral overlap between fluorophores and plasmon resonant single silver nanoparticles. *Nano Letters* **2007,** 7, 690-696.

(86) Ringler, M.; Schwemer, A.; Wunderlich, M.; Nichtl, A.; Kurzinger, K.; Klar, T.; Feldmann, J. Shaping emission spectra of fluorescent molecules with single plasmonic nanoresonators. *Physical Review Letters* **2008,** 100, 203002.

(87) Tam, F.; Goodrich, G. P.; Johnson, B. R.; Halas, N. J. Plasmonic enhancement of molecular fluorescence. *Nano Letters* **2007,** 7, 496-501.

(88) Anderson, J. P.; Griffiths, M.; Boveia, V. R. Near-Infrared Fluorescence Enhancement Using Silver Island Films. *Plasmonics* **2006,** 1, 103-110.

(89) Anderson, J. P.; Griffiths, M.; Williams, J. G.; Grone, D. L.; Steffens, D. L.; Middendorf, L. M., Near-IR Metal Enhanced Fluorescence and Controlled Colloidal Aggregation. In *Metal-Enhanced Fluorescence*, Geddes, C. D., Ed. John Wiley & Sons, Inc.: Hoboken, NJ, 2010, pp 119-137.

(90) Geddes, C. D.; Cao, H.; Gryczynski, I.; Gryczynski, Z.; Fang, J.; Lakowicz, J. R. Metal-enhanced fluorescence (MEF) due to silver colloids on a planar surface: potential applications of indocyanine green to in vivo imaging. *Journal of Physical Chemistry A* **2003,** 107, 3443-3449.

(91) Malicka, J.; Gryczynski, I.; Geddes, C.; Lakowicz, J. R. Metal-enhanced emission from indocyanine green: a new approach to *in vivo* imaging. *Journal of Biomedical Optics* **2003,** 8, 472-478.

(92) Tabakman, S. M.; Lau, L.; Robinson, J. T.; Price, J.; Sherlock, S. P.; Wang, H.; Zhang, B.; Chen, Z.; Tangsombatvisit, S.; Jarrell, J. A.; Utz, P. J.; Dai, H. Plasmonic substrates for multiplexed protein microarrays with femtomolar sensitivity and broad dynamic range. *Nature Communications* [Online] **2011**, 2, 466, 10.1038/ncomms1477

(93) Zhang, B.; Price, J.; Hong, G.; Tabakman, S. M.; Wang, H.; Jarrell, J. A.; Feng, J.; Utz, P. J.; Dai, H. Multiplexed cytokine detection on plasmonic gold substrates with enhanced near-infrared fluorescence. *Nano Research* **2013,** 6, 113-120.

(94) Bardhan, R.; Grady, N. K.; Halas, N. J. Nanoscale control of near-infrared fluorescence enhancement using Au nanoshells. *Small* **2008,** 4, 1716-1722.

(95) Bardhan, R.; Grady, N. K.; Cole, J. R.; Joshi, A.; Halas, N. J. Fluorescence enhancement by Au nanostructures: nanoshells and nanorods. *ACS Nano* **2009,** 3, 744-752.

(96) Xu, S.; Hartvickson, S.; Zhao, J. X. Engineering of SiO_2-Au-SiO_2 sandwich nanoaggregates using a building block: single, double, and triple cores for enhancement of near infrared fluorescence. *Langmuir* **2008,** 24, 7492-7499.

(97) Anderson, J. P.; Griffiths, M.; Williams, J. G.; Grone, D. L.; Lamb, D. T.; Boveia, V. R. In *Analysis of metal enhanced fluorescence on near-IR fluorophores*, Plasmonics: Metallic Nanostructures and Their Optical Properties V, San Diego, CA, 2007; Stockman, M. I., Ed. Proceedings of SPIE: San Diego, CA, 2007; p 664108.

(98) Turkevich, J.; Stevenson, P. C.; Hillier, J. A study of the nucleation and growth processes in the synthesis of colloidal gold. *Discussions of the Faraday Society* **1951,** 11, 55-77.

(99) Lee, P.; Meisel, D. Adsorption and surface-enhanced Raman of dyes on silver and gold sols. *Journal of Physical Chemistry* **1982,** 86, 3391-3395.

(100) Anderson, J. P.; Urlacher, T. M. Colloidal metal aggregates and methods of use. 2009.

(101) Zhang, W.; Ding, F.; Li, W.-D.; Wang, Y.; Hu, J.; Chou, S. Y. Giant and uniform fluorescence enhancement over large areas using plasmonic nanodots in 3D resonant cavity nanoantenna by nanoimprinting. *Nanotechnology* **2012,** 23, 225301.

(102) Zhou, L.; Ding, F.; Chen, H.; Ding, W.; Zhang, W.; Chou, S. Y. Enhancement of immunoassay's fluorescence and detection sensitivity using three-dimensional plasmonic nano-antenna-dots array. *Analytical Chemistry* **2012,** 84, 4489-4495.

(103) Liu, S.-Y.; Huang, L.; Li, J.-F.; Wang, C.; Li, Q.; Xu, H.-X.; Guo, H.-L.; Meng, Z.-M.; Shi, Z.; Li, Z.-Y. Simultaneous Excitation and Emission Enhancement of Fluorescence Assisted by Double Plasmon Modes of Gold Nanorods. *The Journal of Physical Chemistry C* **2013,** 117, 10636-10642.

(104) van Dijk, T.; Sivapalan, S. T.; DeVetter, B. M.; Yang, T. K.; Schulmerich, M. V.; Murphy, C. J.; Bhargava, R.; Carney, P. S. Competition Between Extinction and Enhancement in Surface-Enhanced Raman Spectroscopy. *The Journal of Physical Chemistry Letters* **2013,** 4, 1193-1196.

(105) Sivapalan, S. T.; DeVetter, B. M.; Yang, T. K.; van Dijk, T.; Schulmerich, M. V.; Carney, P. S.; Bhargava, R.; Murphy, C. J. Off-Resonance Surface-Enhanced Raman Spectroscopy from Gold Nanorod Suspensions as a Function of Aspect Ratio: Not What We Thought. *ACS Nano* **2013,** 7, 2099-2105.

(106) Ameer, F. S.; Ansar, S. M.; Hu, W.; Zou, S.; Zhang, D. Inner Filter Effect on Surface Enhanced Raman Spectroscopic Measurement. *Analytical Chemistry* **2012,** 84, 8437-8441.

(107) Han, H.; Valle, V.; Maye, M. M. Probing Resonance Energy Transfer and Inner Filter Effects in Quantum Dot–Large Metal Nanoparticle Clusters using a DNA-Mediated Quench and Release Mechanism. *The Journal of Physical Chemistry C* **2012,** 116, 22996-23003.

(108) Le Ru, E. C.; Galloway, C.; Etchegoin, P. G. On the connection between optical absorption/extinction and SERS enhancements. *Physical Chemistry Chemical Physics* **2006,** 8, 3083-3087.

(109) Kleinman, S. L.; Sharma, B.; Blaber, M. G.; Henry, A.-I.; Valley, N.; Freeman, R. G.; Natan, M. J.; Schatz, G. C.; Van Duyne, R. P. Structure Enhancement Factor Relationships in Single Gold Nanoantennas by Surface-Enhanced Raman Excitation Spectroscopy. *Journal of the American Chemical Society* **2012,** 135, 301-308.

(110) Moskovits, M. Persistent misconceptions regarding SERS. *Physical Chemistry Chemical Physics* **2013,** 15, 5301-5311.

(111) Chivers, C. E.; Koner, A. L.; Lowe, E. D.; Howarth, M. How the biotin-streptavidin interaction was made even stronger: investigation via crystallography and a chimaeric tetramer. *Biochemical Journal* **2011,** 435, 55-63.

(112) Le Trong, I.; Wang, Z.; Hyre, D. E.; Lybrand, T. P.; Stayton, P. S.; Stenkamp, R. E. Streptavidin and its biotin complex at atomic resolution. *Acta Crystallographica Section D: Biological Crystallography* **2011,** 67, 813-821.

(113) Harris, L. J.; Larson, S. B.; Hasel, K. W.; McPherson, A. Refined Structure of an Intact IgG2a Monoclonal Antibody†,‡. *Biochemistry* **1997,** 36, 1581-1597.

(114) IRDye(R) 680LT Protein Labeling Kit - Microscale. [Online] **2011**,

(115) Hohenester, U.; Trugler, A. MNPBEM - A Matlab toolbox for the simulation of plasmonic nanoparticles. *Computer Physics Communications* **2012,** 183, 370-381.

(116) Smaili, S.; Massoud, Y., Field enhancement by spherical dimers in the quasistatic regime. In *2011 IEEE Nanotechnology Materials and Devices Conference*, IEEE: Jeju, Korea, 2011; pp 583-587.

(117) Furtaw, M. D.; Lin, D.; Wu, L.; Anderson, J. P. Near-infrared metal-enhanced fluorescence using a liquid-liquid droplet micromixer in a disposable poly(methyl methacrylate) microchip. *Plasmonics* **2009,** 4, 273-280.

(118) Barry, R.; Ivanov, D. Microfluidics in biotechnology. *Journal of Nanobiotechnology* **2004,** 2.

(119) Beebe, D. J.; Mensing, G. A.; Walker, G. M. Physics and Applications of Microfluidics in Biology. *Annual Review of Biomedical Engineering* **2002,** 4, 261-286.

(120) Whitesides, G. M. The origins and the future of microfluidics. *Nature* **2006,** 442, 368-373.

(121) Olive, D. M. Quantitative methods for the analysis of protein phosphorylation in drug development. *Expert Rev Proteomics* **2004,** 1, 327-41.

(122) Shah, K.; Weissleder, R. Molecular optical imaging: applications leading to the development of present day therapeutics. *NeuroRX* **2005,** 2, 215-225.

(123) Chen, Y.-H.; Chen, S.-H. Analysis of DNA fragments by microchip electrophoresis fabricated on poly(methyl methacrylate) substrates using a wire-imprinting method. *Electrophoresis* **2000,** 21, 165-170.

(124) Lee, G.-B.; Chen, S.-H.; Huang, G.-R.; Sung, W.-C.; Lin, Y.-H. Microfabricated plastic chips by hot embossing methods and their applications for DNA separation and detection. *Sensors and Actuators B* **2001,** 75, 142-148.

(125) Wabuyele, M. B.; Ford, S. M.; Stryjewski, W.; Barrow, J.; Soper, S. A. Single molecule detection of double-stranded DNA in poly(methylmethacrylate) and polycarbonate microfluidic devices. *Electrophoresis* **2001,** 22, 3939-3948.

(126) Wang, Y.; Vaidya, B.; Farquar, H. D.; Stryjewski, W.; Hammer, R. P.; McCarley, R. L.; Soper, S. A. Microarrays assembled in microfluidic chips fabricated from poly(methyl methacylate) for the detection of low-abundant DNA mutations. *Analytical Chemistry* **2003,** 75, 1130-1140.

(127) Drexhage, K. H.; Kuhn, H.; Schäfer, F. P. Variation of the Fluorescence Decay Time of a Molecule in Front of a Mirror. *Berichte der Bunsengesellschaft für physikalische Chemie* **1968,** 72, 329-329.

(128) Aslan, K.; Lakowicz, J. R.; Geddes, C. D. Plasmon light scattering in biology and medicine: new sensing approaches, visions and perspectives. *Current Opinion in Chemical Biology* **2005,** 9, 538-544.

(129) Geddes, C. D.; Parfenov, A.; Gryczynski, I.; Malicka, J.; Roll, D.; Lakowicz, J. R. Fractal silver structures for metal-enhanced fluorescence: applications for ultra-bright surface assays and lab-on-a-chip-based technologies. *Journal of Fluorescence* **2003,** 13, 119-122.

(130) Lakowicz, J.; Gryczynski, I.; Malicka, J.; Gryczynski, Z.; Geddes, C. Enhanced and Localized Multiphoton Excited Fluorescence Near Metallic Silver Islands: Metallic Islands Can Increase Probe Photostability. *Journal of Fluorescence* **2002,** 12, 299-302.

(131) Aslan, K.; Leonenko, Z.; Lakowicz, J.; Geddes, C. Annealed Silver-Island Films for Applications in Metal-Enhanced Fluorescence: Interpretation in Terms of Radiating Plasmons. *Journal of Fluorescence* **2005,** 15, 643-654.

(132) Kummerlen, J.; Leitner, A.; Brunner, H.; Aussenegg, F. R.; Wokaun, A. Enhanced dye fluorescence over silver island films: analysis of the distance dependence. *Molecular Physics* **1993,** 80, 1031-1046.

(133) Ray, K.; Chowdhury, M. H.; Lakowicz, J. R. Aluminum Nanostructured Films as Substrates for Enhanced Fluorescence in the Ultraviolet-Blue Spectral Region. *Analytical Chemistry* **2007,** 79, 6480-6487.

(134) Chowdhury, M. H.; Ray, K.; Gray, S. K.; Pond, J.; Lakowicz, J. R. Aluminum nanoparticles as substrates for metal-enhanced fluorescence in the ultraviolet for the label-free detection of biomolecules. *Analytical Chemistry* **2009,** 81, 397-1403.

(135) Aslan, K.; Lakowicz, J. R.; Szmacinski, H.; Geddes, C. D. Metal-enhanced fluorescence solution-based sensing platform. *Journal of Fluorescence* **2004,** 14, 677-679.

(136) Aslan, K.; Wu, M.; Lakowicz, J. R.; Geddes, C. D. Metal Enhanced Fluorescence Solution-based Sensing Platform 2: Fluorescent Core-Shell Ag@SiO2 Nanoballs. *Journal of Fluorescence* **2007,** 17, 127-131.

(137) Lukomska, J.; Gryczynski, I.; Malicka, J.; Makowiec, S.; Lakowicz, J. R.; Gryczynski, Z. One- and two-photon induced fluorescence of Pacific Blue-labeled human serum albumin deposited on different core size silver colloids. *Biopolymers* **2006,** 81, 249-255.

(138) Sun, C.; Wu, X.; Ding, H.; Zhao, L.; Wang, F.; Yang, J.; Liu, X. The Fluorescence Enhancement of the Protein Adsorbed on the Surface of Ag Nanoparticle. *Journal of Fluorescence* **2009,** 19, 111-117.

(139) Zhang, J. Oligonucleotide-displaced organic monolayer-protected silver nanoparticles and enhanced luminescence of their salted aggregates. *Analytical Biochemistry* **2004,** 330, 81-86.

(140) Chen, L.; Choo, J. Recent advances in surface-enhanced Raman scattering detection technology for microfluidic chips. *Electrophoresis* **2008,** 29, 1815-1828.

(141) Keir, R.; Igata, E.; Arundell, M.; Smith, W. E.; Graham, D.; McHugh, C.; Cooper, J. M. SERRS. In situ substrate formation and improved detection using microfluidics. *Analytical Chemistry* **2002,** 74, 1503-1508.

(142) Lee, S.; Choi, J.; Chen, L.; Park, B.; Kyong, J. B.; Seong, G. H.; Choo, J.; Lee, Y.; Shin, K.-H.; Lee, E. K.; Joo, S.-W.; Lee, K.-H. Fast and sensitive trace analysis of malachite green using a surface-enhanced Raman microfluidic sensor. *Analytica Chimica Acta* **2007,** 590, 139-144.

(143) Park, T.; Lee, S.; Seong, G. H.; Choo, J.; Lee, E. K.; Kim, Y. S.; Ji, W. H.; Hwang, S. Y.; Gweon, D.-G.; Lee, S. Highly sensitive signal detection of duplex dye-labelled DNA oligonucleotides in a PDMS microfluidic chip: confocal surface-enhanced Raman spectroscopic study. *Lab on a Chip* **2005,** 5, 437.

(144) Strehle, K. R.; Cialla, D.; Rosch, P.; Henkel, T.; Kohler, M.; Popp, J. A reproducible surface-enhanced Raman spectroscopy approach. Online SERS measurements in a segmented microfluidic system. *Analytical Chemistry* **2007,** 79, 1542-1547.

(145) Tice, J. D.; Song, H.; Lyon, A. D.; Ismagilov, R. F. Formation of droplets and mixing in multiphase microfluidics at low values of the Reynolds and the capillary numbers. *Langmuir* **2003,** 19, 9127-9133.

(146) Bringer, M. R.; Gerdts, C. J.; Song, H.; Tice, J. D.; Ismagilov, R. F. Microfluidic systems for chemical kinetics that rely on chaotic mixing in droplets. *Philosophical Transactions A: Math, Physics, and Engineering Sciences* **2004,** 362, 1087-1104.

(147) Nguyen, N.-T., *Micromixers : fundamentals, design and fabrication*. William Andrew: Norwich, NY, 2008.

(148) Stone, Z. B.; Stone, H. A. Imaging and quantifying mixing in a model droplet micromixer. *Physics of Fluids* **2005,** 17, 063103.

(149) Zhang, P. X.; Fang, Y.; Wang, W. N.; Ni, D. H.; Fu, S. Y. Influence of addition of potassium chloride to silver colloids. *Journal of Raman Spectroscopy* **1990,** 21, 127-131.

(150) Furtaw, M. D.; Anderson, J. P.; Middendorf, L. R.; Bashford, G. R. Near-infrared, surface-enhanced fluorescence using silver nanoparticle aggregates in solution. *Plasmonics* **2013**.

(151) Vladar, A. E.; Ming, B. *Measuring the size of colloidal gold nano-particles using high-resolution scanning electron microscopy*; PCC-15; Natl. Inst. Stand. Technol.: NIST (U.S.), 2011.

(152) Bonevich, J. E.; Haller, W. K. Measuring the size of nanoparticles using transmission electron microscopy (TEM); NIST - NCL Joint Assay Protocol, Gaithersburg, MD, 2010.

(153) Schwartzberg, A. M.; Grant, C. D.; Wolcott, A.; Talley, C. E.; Huser, T. R.; Bogomolni, R.; Zhang, J. Z. Unique gold nanoparticle aggregates as a highly active surface-enhanced Raman scattering substrate. *Journal of Physical Chemistry B* **2004,** 108, 19191-19197.

(154) Bharadwaj, P.; Novotny, L. Spectral dependence of single molecule fluorescence enhancement. *Optics Express* **2007,** 15, 14266-14274.

(155) Quinten, M. Local fields close to the surface of nanoparticles and aggregates of nanoparticles. *Applied Physics B: Lasers and Optics* **2001,** 73, 245-255.

(156) Tynan, C. J.; Clarke, D. T.; Coles, B. C.; Rolfe, D. J.; Martin-Fernandez, M. L.; Webb, S. E. Multicolour single molecule imaging in cells with near infra-red dyes. *PLoS One* **2012,** 7, e36265.

(157) Rissin, D. M.; Kan, C. W.; Campbell, T. G.; Howes, S. C.; Fournier, D. R.; Song, L.; Piech, T.; Patel, P. P.; Chang, L.; Rivnak, A. J.; Ferrell, E. P.; Randall, J. D.; Provuncher, G. K.; Walt, D. R.; Duffy, D. C. Single-molecule enzyme-linked immunosorbent assay detects serum proteins at subfemtomolar concentrations. *Nature Biotechnology* **2010,** 28, 595-599.

(158) Furtaw, M. D.; Steffens, D. L.; Urlacher, T. M.; Anderson, J. P. A near-infrared, surface-enhanced, fluorophore-linked immunosorbent assay. *Analytical Chemistry* **2013,** 85, 7102-7108.

(159) Katz, E.; Willner, I. Integrated nanoparticle-biomolecule hybrid systems: synthesis, properties, and applications. *Angewandte Chemie International Edition* **2004,** 43, 6042-6108.

(160) Drachev, V. P.; Perminov, S. V.; Rautian, S. G.; Safonov, V. P., Nonlinear Optical Effects and Selective Photomodification of Colloidal Silver Aggregates. In *Optical Properties of Nanostructured Random Media*, Shalaev, V. M., Ed. Springer Berlin Heidelberg: 2002, Vol. 82, pp 115-148.

(161) Gill, R.; Le Ru, E. C. Fluorescence enhancement at hot-spots: the case of Ag nanoparticle aggregates. *Physical Chemistry Chemical Physics* **2011,** 13, 16366-16372.

(162) Gill, R.; Tian, L.; Somerville, W. R.; Le Ru, E. C.; van Amerongen, H.; Subramaniam, V. Silver nanoparticle aggregates as highly efficient plasmonic antennas for fluorescence enhancement. *Journal of Physical Chemistry C* **2012,** 116, 16687-16693.

(163) R&D Systems. Human alpha-Fetoprotein Quantikine ELISA kit. http://rndsystems.com/Products/DAFP00

(164) Ball, D.; Rose, E.; Alpert, E. Alpha-fetoprotein levels in normal adults. *American Journal of the Medical Sciences* **1992,** 303, 157-159.

(165) Olajide, F.; Kitau, M.; Chard, T. Maternal serum AFP levels in the first trimester of pregnancy. *European Journal of Obstetrics & Gynecology and Reproductive Biology* **1989,** 30, 123-128.

(166) Richardson, B. E.; Hulka, B. S.; Peck, J. L. D.; Hughes, C. L.; van den Berg, B. J.; Christianson, R. E.; Calvin, J. A. Levels of maternal serum alpha-

fetoprotein (AFP) in pregnant women and subsequent breast cancer risk. *American Journal of Epidemiology* **1998,** 148, 719-727.

(167) Waller, D. K.; Lustig, L. S.; Smith, A. H.; Hook, E. B. Alpha-Fetoprotein: A Biomarker for Pregnancy Outcome. *Epidemiology* **1993,** 4, 471-476.

(168) Blohm, M. E. G.; Versterling-Horner, D.; Calaminus, G.; Gobel, U. Alpha$_1$-fetoprotein (AFP) reference values in infants up to 2 years of age. *Pediatric Hematology and Oncology* **1998,** 15, 135-142.

(169) Tangkijvanich, P.; Anukulkarnkusol, N.; Suwangool, P.; Lertmaharit, S.; Hanvivatvong, O.; Kullavanijaya, P.; Poovorawan, Y. Clinical characteristics and prognosis of hepatocellular carcinoma. *Journal of Clinical Gastroenterology* **2000,** 31, 302-308.

(170) Sato, Y.; Nakata, K.; Kato, Y.; Shima, M.; Ishii, N.; Koji, T.; Taketa, K.; Endo, Y.; Nagataki, S. Early recognition of hepatocellular carcinoma based on altered profiles of alpha-fetoprotein. *New England Journal of Medicine* **1993,** 328, 1802-1806.

(171) Liedberg, B.; Nylander, C.; Lunstrom, I. Surface plasmon resonance for gas detection and biosensing. *Sensors and Actuators* **1983,** 4, 299-304.

(172) Green, R. J.; Frazier, R. A.; Shakesheff, K. M.; Davies, M. C.; Roberts, C. J.; Tendler, S. J. B. Surface plasmon resonance analysis of dynamic biological interactions with biomaterials. *Biomaterials* **2000,** 21, 1823-1835.

(173) Zhang, D.; Neumann, O.; Wang, H.; Yuwono, V. M.; Barhoumi, A.; Perham, M.; Hartgerink, J. D.; Wittung-Stafshede, P.; Halas, N. J. Gold nanoparticles can induce the formation of protein-based aggregates at physiological pH. *Nano Letters* **2009,** 9, 666-671.

(174) Dominguez-Medina, S.; McDonough, S.; Swanglap, P.; Landes, C. F.; Link, S. In situ measurement of bovine serum albumin interaction with gold nanospheres. *Langmuir* **2012,** 28, 9131-9139.

(175) Goy-Lopez, S.; Juarez, J.; Alatorre-Meda, M.; Casals, E.; Puntes, V. F.; Taboada, P.; Mosquera, V. Physicochemical characteristics of protein-NP bioconjugates: the role of particle curvature and solution conditions on human

serum albumin conformation and fibrillogenesis inhibition. *Langmuir* **2012,** 28, 9113-9126.

(176) Khan, A. A.; Fox, E. K.; Górzny, M. Ł.; Nikulina, E.; Brougham, D. F.; Wege, C.; Bittner, A. M. pH Control of the Electrostatic Binding of Gold and Iron Oxide Nanoparticles to Tobacco Mosaic Virus. *Langmuir* **2013,** 29, 2094-2098.

(177) Zhang, X.; Servos, M. R.; Liu, J. Instantaneous and quantitative functionalization of gold nanoparticles with thiolated DNA using a pH-assisted and surfactant-free route. *Journal of the American Chemical Society* **2012,** 134, 7266-7269.

(178) Zhang, X.; Servos, M. R.; Liu, J. Fast pH-assisted functionalization of silver nanoparticles with monothiolated DNA. *Chemical Communications* **2012,** 48, 10114-10116.

(179) Gopinath, A.; Boriskina, S. V.; Feng, N.-N.; Reinhard, B. M.; Dal Negro, L. Photonic-plasmonic scattering resonances in deterministic aperiodic structures. *Nano Letters* **2008,** 8, 2423-2431.

(180) Yan, B.; Thubagere, A.; Premasiri, W. R.; Ziegler, L. D.; Del Negro, L.; Reinhard, B. M. Engineered SERS substrates with multiscale signal enhancement: nanoparticle cluster arrays. *ACS Nano* **2009,** 3, 1190-1202.

(181) Gopinath, A.; Boriskina, S. V.; Premasiri, W. R.; Ziegler, L. D.; Reinhard, B. M.; Dal Negro, L. Plasmonic nanogalaxies: multiscale aperiodic arrays for surface-enhanced Raman sensing. *Nano Letters* **2009,** 9, 3922-3929.

(182) Yan, B.; Boriskina, S. V.; Reinhard, B. M. Design and implementation of noble metal nanoparticle cluster arrays for plasmon enhanced biosensing. *The Journal of Physical Chemistry C* **2011,** 115, 24437-24453.

(183) Yan, B.; Boriskina, S. V.; Reinhard, B. M. Optimizing gold nanoparticle cluster configurations ($n<=7$) for array applications. *The Journal of Physical Chemistry C* **2011,** 115, 4578-1583.

(184) Fabris, L. *Bottom-up* optimization of SERS *hot-spots*. *Chemical Communications* **2012,** 48, 9346-9348.

(185) Fabris, L.; Dante, M.; Nguyen, T.-Q.; Tok, J. B.-H.; Bazan, G. C. SERS aptatags: new responsive metallic nanostructures for heterogeneous protein detection by surface enhanced Raman spectroscopy. *Advanced Functional Materials* **2008,** 18, 2518-2525.

(186) Guarrottxena, N.; Liu, B.; Fabris, L.; Bazan, G. C. *Anti*tags: Nanostructured tools for developing SERS-based ELISA analogs. *Advanced Materials* **2010,** 22, 4954-4958.

(187) Guarrotxena, N.; Bazan, G. C. Antibody-functionalized SERS tags with improved sensitivity. *Chemical Communications* **2011,** 47, 8784-8786.

APPENDIX A. MATLAB CODE

```
%This program simulates the electromagnetic field around a dimer
%of nanoparticles using the MNPBEM toolbox.

%written by Michael Furtaw, 1-5-2012


clear all
clc


%INPUT PARAMETERS
diam = 20;      %nanoparticle diameter, nm
distbtw = 5;    %distance between NPs, nm
enei = 785;     %light wavelength in vacuum, nm
xynum = 161;    %number of points in x and y axes


%CREATE NANOPARTICLE AND PLOT NORMAL VECTORS
p1 = trisphere(256,diam);
p1 = shift(p1,[-.5*diam-.5*distbtw,0,0]);
p2 = trisphere(256,diam);
p2 = shift(p2,[.5*diam+.5*distbtw,0,0]);


%CREATE DIELECTRIC ENVIRONMENT
epstab =
{epsconst(1.33^2),epstable('silver.dat'),epstable('silver.dat')};
p = comparticle(epstab,{p1,p2},[2,1;3,1],1,2);
figure(1)
plot(p,'EdgeColor','b','nvec',1)


%CREATE POINT CLOUD FOR ELECTRIC FIELD VISUALIZATION
[x,y] = meshgrid(linspace(-2*diam,2*diam,xynum));
z = 0*x;
pt = compoint(p,[x(:),y(:),z(:)],'mindist',1);


%SET UP COMPSTRUCT WITH PLANE WAVE EXCITATION
exc = planewavestat([1,0,0]);   %quasistatic plane wave with x-
polarization
c = exc(p,enei);                %excitation potential at wavelength
figure(2)
plot(p,c.phip)                  %plot excitation field on particle


%CALL BEM SOLVER WITH QUASISTATIC APPROXIMATION
sig = bemstat(p) \ c;
figure(3)
plot(p,sig.sig)


%CALCULATE GREEN FUNCTION BETWEEN POINTS AND PARTICLE
```

```
g = compgreen(pt,p);


%CALCULATE ELECTRIC FIELD AT POINTS
field = g.field(sig)+exc.field(pt,enei);
figure(4)
coneplot(pt.pos,real(field.e(:,:,1)),'scale',1);
view(0,90);
plot(p,'EdgeColor','k');


%CALCULATE ELECTRIC FIELD MODULUS FOR CONTOUR PLOT
modgrid = 0*x;
for i = 1:length(field.e)       %loop to put modulus in meshgrid format
    indx = round((pt.pos(i,1)+2*diam)*(xynum-1)/(4*diam)+1);
    indy = round((2*diam-pt.pos(i,2))*(xynum-1)/(4*diam)+1);
    vectpt = real(field.e(i,:));
    modgrid(indy,indx) =
(vectpt(:,1))^2+(vectpt(:,2))^2+(vectpt(:,3))^2;
end
figure(5)
surf(x,y,log(modgrid));
view(0,90);
colorbar;
shading interp;
plot(p,'EdgeColor','k');
```

APPENDIX B. SEFLISA ASSAY PROTOCOLS

DIRECT SEFLISA (RABBIT IGG)

A. Antigen Immobilization

  a. Complete a two-fold serial dilution of rabbit IgG to obtain samples between 1000 pg/ml and 2 pg/ml. The buffer is carbonate-bicarbonate with a pH between 9.2 and 9.8.
  b. Add 100 µl of each sample to the appropriate wells in the 96-well microtiter plate.
  c. Cover plate and incubate overnight at 4°C.

B. Blocking

  a. Invert plate and shake out antigen.
  b. Wash each well in plate with 300 µl of PBST 2 times and PBS 1 time for 1 minute each on a plate shaker.
  c. Add 300 µl of Odyssey blocking buffer to each well.
  d. Cover plate and incubate for 1 hour at room temperature on a plate shaker.

C. Detection Antibody

  a. Invert plate and shake out blocking buffer. No need to wash at this point.
  b. Dilute biotinylated anti-rabbit conjugate in blocking buffer to a concentration of 1 µg/ml.
  c. Add 100 µl of diluted detection antibody to each well.
  d. Cover plate and incubate for 1 hour at room temperature on a plate shaker.

D. Streptavidin – Fluorophore Conjugate

  a. Invert plate and shake out detection antibody.
  b. Wash each well in plate with 300 µl of PBST 2 times and PBS 1 time for 1 minute each on a plate shaker.
  c. Dilute SAv-800CW (1 mg/ml) in blocking buffer to a concentration of 0.1 µg/ml.
  d. Add 100 µl of diluted SAv-800CW to each well.

- e. Cover plate with seal and foil, incubate for 1 hour at room temperature on a plate shaker.

E. Protease K Solution

- a. Invert plate and shake out streptavidin – fluorophore conjugate.
- b. Wash each well in plate with 300 µl of PBST 1 time, PBS 1 time, and dH_2O 1 time for 1 minute each on a plate shaker.
- c. Dilute protease K salt solution (250X) by 1:250 in dH_2O.
- d. Add 50 µl of diluted protease K salt solution to each well. Note: 50 µl of dH_2O was added to reference (FLISA) wells instead.
- e. Cover plate with seal and foil, incubate for 30 minutes at room temperature on a plate shaker.

F. AgNP Solution

- a. Add 50 µl of AgNP solution to each well. Note: 50 µl of dH_2O was added to reference (FLISA) wells instead.
- b. Cover plate with seal and foil, incubate for 15 minutes at room temperature on a plate shaker.
- c. Detect on Odyssey Sa with a focus offset of 3.4 mm at an intensity of 11.

SANDWICH SEFLISA (AFP)

A. Capture Antibody

- a. Dilute mouse anti-human AFP in PBS to a concentration of 2 µg/ml.
- b. Add 100 µl of diluted capture antibody to each well in the 96-well microtiter plate.
- c. Cover plate and incubate overnight in drawer (dark) at room temperature.

B. Blocking

- a. Invert plate and shake out excess capture antibody.
- b. Wash each well in plate with 300 µl of PBST 2 times and PBS 1 time for 1 minute each on a plate shaker.
- c. Add 300 µl of Odyssey blocking buffer to each well.

   d. Cover plate and incubate for 1 hour at 37°C on a plate shaker.

C. Antigen

   a. Invert plate and shake out blocking buffer.
   b. There is no need to wash at this point.
   c. Complete a two-fold serial dilution of human AFP to obtain samples between 5000 pg/ml and 9.8 pg/ml. The diluent is 1% BSA in PBS.
   d. Add 100 µl of each sample to the appropriate wells in the 96-well microtiter plate.
   e. Cover plate and incubate for 1 hour at 37°C on a plate shaker.

D. Detection Antibody

   a. Invert plate and shake out sample.
   b. Wash each well in plate with 300 µl of PBST 2 times and PBS 1 time for 1 minute each on a plate shaker.
   c. Dilute biotinylated chicken anti-human AFP in blocking buffer to a concentration of 0.2 µg/ml.
   d. Add 100 µl of diluted detection antibody to each well.
   e. Cover plate and incubate for 1 hour at 37°C on a plate shaker.

E. Streptavidin – Fluorophore Conjugate

   a. Invert plate and shake out detection antibody.
   b. Wash each well in plate with 300 µl of PBST 2 times and PBS 1 time for 1 minute each on a plate shaker.
   c. Dilute SAv-800CW (1 mg/ml) in blocking buffer to a concentration of 0.1 µg/ml.
   d. Add 100 µl of diluted SAv-800CW to each well.
   e. Cover plate with seal and foil, incubate for 1 hour at 37°C on a plate shaker.

F. Protease K Solution

   a. Invert plate and shake out streptavidin – fluorophore conjugate.
   b. Wash each well in plate with 300 µl of PBST 1 time, PBS 1 time, and dH_2O 1 time for 1 minute each on a plate shaker.
   c. Dilute protease K salt solution (250X) by 1:250 in dH2O.
   d. Add 50 µl of diluted protease K salt solution to each well. Note: 50 µl of dH_2O was added to reference (FLISA) wells instead.

e. Cover plate with seal and foil, incubate for 30 minutes at 37°C on a plate shaker.

G. AgNP Solution

a. Add 50 µl of AgNP solution to each well. Note: 50 µl of dH_2O was added to reference (FLISA) wells instead.
b. Cover plate with seal and foil, incubate for 15 minutes at 37°C on a plate shaker.
c. Detect on Odyssey Sa with a focus offset of 3.4 mm at an intensity of 11.

APPENDIX C. EFFECT OF PH ON SEF

As mentioned in Chapter 8, it was found that the pH of the AgNP solution has substantial affect on the SEF process. Commercially available citrate-stabilized AgNP (Ted Pella, Redding, California) were purchased in order to study the effect of size distribution on SEF (as our in-house recipe creates a polydisperse distribution). Upon applying the same SEF process as with LI-COR AgNP, there was no measurable fluorescence enhancement. Knowing the buffer solutions likely differ (without knowing exactly the contents in the purchased AgNP) it was hypothesized that the pH may be the cause of the discrepancy. The AgNP used in this thesis (LI-COR, Lincoln, Nebraska) have a pH ~ 4.0 while the commercially-available AgNP have a pH ~ 7.4. To quickly test the pH hypothesis, the two AgNP solutions were added to a solution of SAv-800CW as received and also with the supernatants swapped after spinning-down the AgNP. Figure C.1 shows qualitatively that JA AgNP (LI-COR, Jon Anderson) demonstrate significant SEF while TP AgNP (Ted Pella) show no enhancement (Figure C.1, middle row) relative to SAv-800CW alone (Figure C.1, top row). Upon swapping the supernatants (Figure C.1, bottom row), the JA AgNP show no enhancement while the TP AgNP show significant enhancement in one well and not the other (we assume a mistake was made in the centrifugation or pipetting).

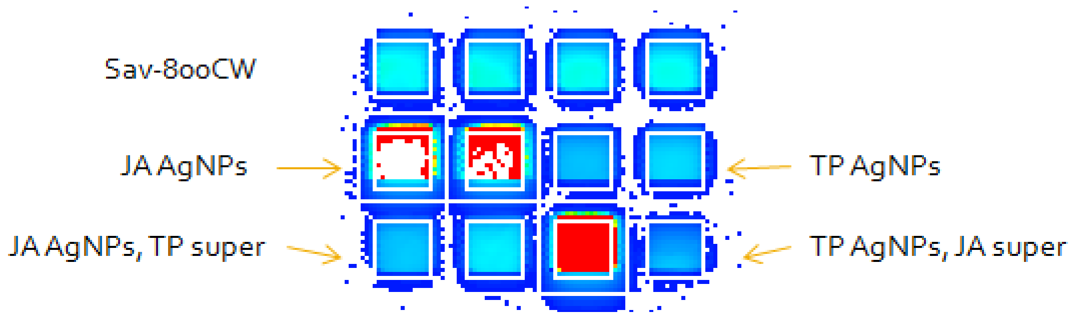

Figure C.1. Fluorescence image of SAv-800CW alone (top row), JA AgNP and TP AgNP as received (middle row), and JA AgNP and TP AgNP with supernatants swapped (bottom row). The fluorescence intensity is shown on an RGB scale where red is more intense and blue is less intense (white is saturated pixels).

With further evidence that pH may have a significant effect on SEF, the hypothesis was further developed to include the isoelectric point (pI) of the carrier protein. It was then hypothesized that the pH of the AgNP solution must be below the pI of the carrier protein in order to allow a positively-charged carrier protein to interact with the negative, citrate-stabilized AgNP. This was tested by creating a series of AgNP solutions using a common, simple recipe[99] that involves only silver nitrate and citrate where the pH could be tuned using citric acid in place of citrate at various ratios. Different total concentrations of citrate/citric acid were also used to study this effect. Figure C.2 shows fluorescence enhancement versus pH for SAv-800CW mixed with the AgNP solutions at 2 mM and 6mM total citrate/citric acid concentration. Clearly, SEF is affected by pH with the general trend being that lower pH enables more enhancement. Interestingly, the curves seem to have sections where the slope is constant and then abruptly changes. The pKa values of citrate (~ 3.1, 4.8, and 6.4) were added to show that these abrupt changes may be correlated with the protonation of individual carboxyl groups of which there are three. It was also hypothesized that the total concentration of citrate/citric acid may affect SEF by changing the equilibrium surface coverage of the AgNP at each pH value. This would suggest that the SEF would be higher at lower citrate/citric acid concentration which is opposite of the data shown below. It is unclear at this time as to why the higher concentration of citrate/citric acid demonstrates greater SEF, but may be due to changes in the size and/or shape of the AgNP which was not tested. Overall, this data appears quite convincing about some of the hypotheses; however, it was difficult to repeat. Further research is suggested as the pH effect is obviously dramatic (significant SEF to no SEF) but poorly understood.

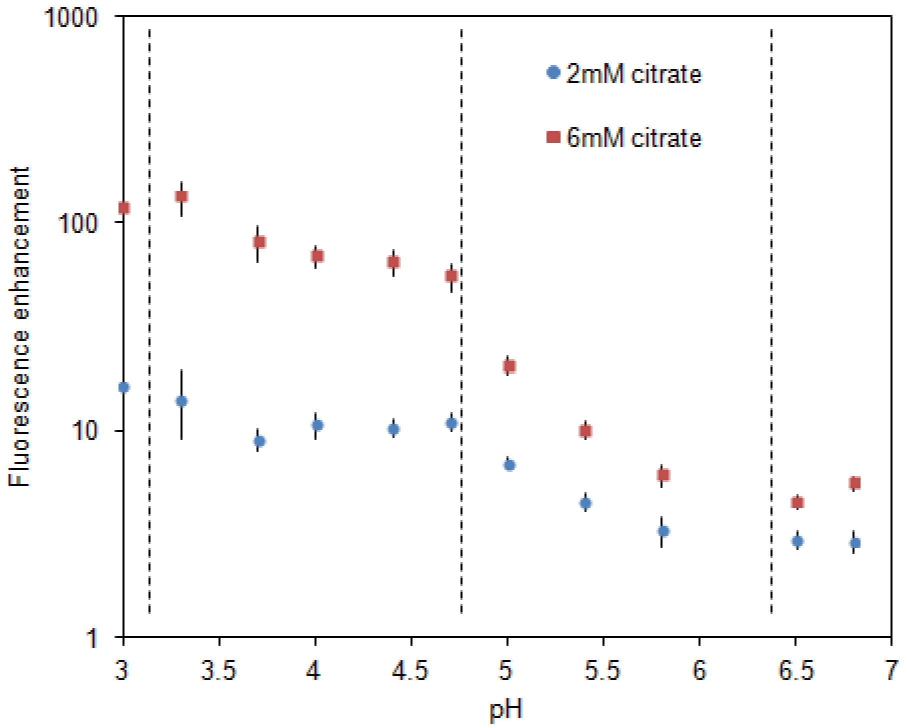

Figure C.2. Fluorescence enhancement versus AgNP solution pH for 2mM and 6 mM total citrate/citric acid concentration. The three pKa values of citrate are shown as vertical dashed lines.